Universitat Politécnica de Catalunya

Doctoral Thesis

Towards the Generation of Isolated Attosecond Pulses in the Water Window

Author:
Seth Lucien Cousin

Supervisor:
Prof. Dr. Jens Biegert

A thesis submitted in fulfilment of the requirements for the degree of Doctor of Philosophy

in the

Attoscience and Ultrafast Optics
ICFO, Institute of Photonic Sciences

May 2016

Abstract

Attosecond science investigates the realm of processes that happen in fleetingly short passages of time. One attosecond to one second, is what one second is to the age of the universe! Advances in lasers and specifically ultra-short pulsed lasers have opened the door to this extreme frontier of physics.

In this thesis I will describe what is required from a laser system in order to access these time scales. The stringent requirements needed motivated us to extensively study, model, redesign and then finally rebuild our laser system making it capable of delivering the necessary laser pulses. Characterisation of these types of laser pulses is essential in making them usable in the pursuit of a fundamental understanding of ultrashort physical processes. Two new characterisation techniques have been developed to add to the suite of tools available to the scientific community to achieve the complicated goal of characterising femtosecond laser pulses.

To jump from the femtosecond regime to the attosecond regime, high harmonic generation is currently the defacto method of getting there. I will give a detailed description of our high harmonic beamline, which ultimately is used to perform the first water-window radiation range spectroscopy from a high harmonic source. Intrinsic to the radiation generated for spectroscopy is the sub-femtosecond temporal structure of the radiation.

Temporal characterisation of attosecond pulses is traditionally done using the attosecond streaking technique however until now, this technique has not been used in the water-window. X-ray pulses possessing our ultra-broad bandwidth and central photon energy

are unprecedented, making this the first time that a streaking experiment is done in this regime.

Acknowledgements

I would foremost like to acknowledge Prof. Dr Jens Biegert for offering me the opportunity to first undertake my masters degree in his group and then to continue on to the doctoral degree. The laboratory provided by him is state of the art and has provided me with every possible tool, first to learn about this exciting discipline of physics and then to help to take it further.

I would also like to acknowledge Dr Phil Bates and Dr Oliver Chalus, who were the post doctoral researchers in the group when I arrived. Dr Bates really showed me what laboratory science is about and when enough tweaking was enough.

For all the technical practicalities of actually building a laser system I would like to thank Dr Michael Hemmer, who joined the group at the perfect time!

Finally I would like to acknowledge Dr Dane Austin, who guided me through my first experiments, instilled proper note taking skills and took my programming skills from zero to the level that I needed.

Publications

Few-cycle pulse characterization with an acousto-optic pulse shaper S.L Cousin, N Forget, A Grün, P.K Bates, D.R Austin, J Biegert, Optics Letters **36** (15), 2803-2805, (2011)

Three-dimensional spatiotemporal pulse characterization with an acousto-optic pulse shaper and a Hartmann-Shack wavefront sensor S.L Cousin, J.M Bueno, N Forget, D.R Austin, J Biegert, Optics Letters **37** (15), 3291-3293, (2012)

Trajectory interferences in a semi-infinite gas cell S.M Teichmann, D.R Austin, P Bates, S.L Cousin, A Grün, M Clerici, A Lotti, D Faccio, P Di Trapani, A Couairon, J Biegert, Laser Physics Letters **9** (3), 207, (2012)

Generation of high-fidelity few-cycle pulses at 2.1 µm via cross-polarized wave generation A Ricci, F Silva, A Jullien, S.L. Cousin, D.R Austin, J Biegert, Rodrigo Lopez-Martens, Optics Express **21** (8), 9711-9721, (2013)

All-PM coherent 2.05 µm Thulium/Holmium fiber frequency comb source at 100 MHz with up to 0.5 W average power and pulse duration down to 135 fs H Hoogland, A Thai, D Sánchez, S.L Cousin, M Hemmer, M Engelbrecht, J Biegert, Ronald Holzwarth, Optics Express **21** (25), 31390-31394,(2013)

High-flux table-top soft x-ray source driven by sub-2-cycle, CEP stable, 1.85-μm 1-kHz pulses for carbon K edge spectroscopy S.L Cousin, F Silva, S Teichmann, M Hemmer, B Buades, J Biegert, Optics Letters **39** (18), 5383-5386,(2014)

Spatio-temporal isolation of attosecond soft X-ray pulses in the water window F Silva, S Teichmann, S.L Cousin, M Hemmer, J Biegert, Nature Communications **6**, 661, (2015)

The importance of intensity to phase coupling for water window high harmonic generation with few-cycle pulses S Teichmann, F Silva, S.L Cousin, J Biegert, Physical Review A **91**, 063817, (2015)

Three-wave mixing mediated femtosecond pulse compression in BBO A Grün, D.R Austin, S.L Cousin, J Biegert, Optics Letters **40** (20), 4679-4682, (2015)

7-micron, ultrafast, sub-mJ-level mid-IR OPCPA pumped at 2 micron D Sanchez, M Hemmer, M Baudisch, S.L.Cousin, K Zawilski, P Schunemann, O Chalus, C Simon-Boisson, J Biegert, Optica **3** (2), (2016)

0.5 keV soft X-ray attosecond continua S Teichmann, F Silva, S.L Cousin, J Biegert, Nature Communications **7**, 11493, (2016)

Contents

List of Figures

List of Tables

Abbreviations

AOPDF	Acousto-Optic Programmable Dispersive Filter
ASE	Amplified Spontaneous Emission
ATI	Above Threshold Ionisation
AUO	Attoscience and Ultrafast Optics
BBO	Beta Barium Borate
CAD	Computer Aided Design
CEP	Carrier Envelope Phase
CFD	Computational Fluid Dynamics
CPA	Chirped Pulse Amplification
DPSS	Diode Pumped Solid State
FEA	Finite Element Analysis
FOD	Fourth Order Dispersion
FROG	Frequency Resolved Optical Gating
FROGCRAB	Frequency Resolved Optical Gating for Complete Reconstruction of Attosecond Bursts
FTL	Fourier Transform Limit
FTSI	Fourier Transform Spectral Interferometry
FWHM	Full Width Half Maximum
GDD	Group Delay Dispersion
GVD	Group Velocity Dispersion

HAMSTER	Hartmann–shack Assisted, Multi-dimensional, Shaper-based Technique for Electric-field Reconstruction
HCF	Hollow-Core Fiber
HHG	High Harmonic Generation
ICFO	The Institute of Photonic Sciences
IT	Information Technology
LSGPA	Least-Squares Generalized Projections Algorithm
Nd:YAG	Neodymium-Doped Yttrium Aluminium Garnet
Nd:YLF	Neodymium-Doped Yttrium Lithium Fluoride
NEXAFS	Near Edge Xray Absorption Fine Structure
OD	Optical Density
OPA	Optical Parametric Amplifier
PCGPA	Principal Component Generalized Projections Algorithm
PFT	Pulse Front Tilt
SHG	Second Harmonic Generation
SPIDER	Spectral Phase Interferometry for Direct Electric-field Reconstruction
SPM	Self Phase Modulation
STC	Spatio-Temporal Coupling
Ti:Sa	Titanium-doped Sapphire
TOD	Third Order Dispersion
ToF	Electron Time of Flight
UHV	Ultra-High Vacuum
WFS	Wavefront Sensor
XUV	Extreme Ultra Violet

Dedicated to my wife Martinette, for her support and sacrifices before, during and after my PhD

Chapter 1

Introduction

1.1 Introduction

In 2005 I was browsing a book store and I came across a book called "Quantum: A Guide For The Perplexed" [1]. After reading the book, I realised my high school physics and maths were insufficient to delve deeper into this strange world and that a university degree was needed. As I was already five years into a burgeoning career in information technology (IT), by then employed by a prestigious law firm, daytime university was not an option. I enrolled at the Open University, which is a distance learning university, and consequently the UK's largest university. The next four years worth of evenings and weekends were spent diligently obtaining a Bachelors degree in Physical Science, with an honours project based on ion trap quantum computing. By the last year of studies, I was hooked on physics and identified that despite the success I was enjoying in IT, a much greater challenge was far more enticing - graduate studies. I applied to universities all over the world that had experimental groups researching ion or atom trapping quantum information, which lead me

to ICFO (The Institute of Photonic Sciences) in Barcelona. In January of 2009, I visited the institute for an interview with Prof. Dr. Jurgen Eschner who's group was investigating atom/ion trapping but on the same day was also invited for an interview with Prof Dr Jens Biegert, group leader of the Attoscience and Ultrafast Optics (AUO) group, researching extreme non-linear optics. I did not have a clue about any of these three terms prior to that day, however after a visit to the AUO laboratory and a read through some of the founding papers of the field of research I was intrigued, to say the least. Fortunately, Prof. Biegert offered me the opportunity to attain first my Masters degree in the group and then to continue on to the PhD.

Over the course of my PhD, one of the cornerstones of this discipline of physics has played the dominating role in shaping my contributions, and that is pulse characterisation. I have developed the ability to characterise pulses from wavelengths as high as 1850 nanometers down to as low as 3.5 nanometers containing pulses as long as 90 nanoseconds and ultimately down to isolated attosecond pulses possessing the spectrum to support 20 attosecond pulse durations. Two new characterisation techniques have been invented to accomplish some of these measurements and the de-facto technique for the characterisation of isolated attosecond pulses has for the first time been applied to the soft x-ray regime.

Key to these achievements and this discipline of physics is the ultrashort pulsed laser system. Despite the relatively mature technology of titanium sapphire laser systems, the requirements needed to investigate the attosecond regime are still barely accomplished by commercially available laser systems. A significant proportion of my doctoral degree has been dedicated to laser development of the laser system to achieve these stringent requirements.

Chapter 2

Titanium Sapphire Seeded, 1.85 μm Few Cycle, CEP Stable, Laser Pulses

2.1 Introduction

In the first part of this chapter, I will describe the extensive work undertaken over the course of the first few years of my PhD, in which a problematic commercial laser system was completely redesigned and rebuilt to the high level of quality required to pump a wavelength conversion stage. The second part of the chapter explains briefly this wavelength conversion stage and subsequent pulse compression- and stabilisation- systems.

2.2 Titanium:Sapphire Laser Systems

The full spectroscopic and laser characterisation of titanium-doped sapphire (Ti:Sa) in 1986 [2] paved the way for the now mature field of femtosecond laser physics. This is due predominantly to the broad fluorescence spectrum of Ti:Sa ranging from below 600 nm to over 1050 nm. Such a broad bandwidth i.e. having a full width half maximum (FWHM) of ≈200 nm can in principle already support a pulse duration of less than 4 fs. In addition to this, the absorption cross-section is centred around 500 nm which is a favourable wavelength for the frequency-doubled high power diode pumped solid state (DPSS) pump lasers which have been extensively developed and are now capable of providing up to 100 mJ of 527/532 nm at 1 kHz [3]. The cryogenic properties of sapphire which will be discussed in more detail, offer significant benefits for high average power laser systems.

When I joined the group, we had just acquired the highest average power, kilohertz-repetition-rate Ti:Sa laser amplifier in the world. The system had a specification of 50 W at 5 kHz (10 mJ) and a pulse duration of around 25 fs. A laser system of such specifications could realistically only be thought of as "research" grade i.e. Fitting in-between a prototype and a commercially ready system.

The Ti:Sa system is based on the concept of chirped pulse amplification (CPA) [4], common to all similar systems of this power level. The CPA scheme prevents laser damage of optical components caused by the amplification of high intensity laser pulses. Low energy, femtosecond pulses generated in a mode-locked oscillator are first stretched in time (in our case from a few tens of femtoseconds to hundreds of picoseconds) which significantly reduces their peak

intensity. The now low peak intensity pulses can be amplified significantly to much higher energies but with peak intensities well below the damage threshold of the optical components. After amplification, the pulses can then be re-compressed to provide the high energy and high peak intensities desired.

Most simply described, our laser system comprised of a Ti:Sa oscillator, a Dazzler (discussed in section 3.3) and a stretcher followed by two subsequent amplification stages and a compressor. Within the first few months of operation it became clear that the laser system was suffering from some debilitating problems, manifesting primarily in the inability to reach operating specifications without damaging optics. Additionally, spatial diagnostics revealed significant distortions which would later prove insurmountable in attempts to use the laser system to drive a wavelength conversion stage, whose efficacy depends on a high level of spatio-temporal beam quality. The two main problems with the system were: 1) The poor output beam quality and 2) the inability to sustain the high average powers without damaging optical components. Another issue that complicated use of the system was that daily start-up would require minor re-alignment in the first stage and more significant re-alignment in the second stage. Compounding this with more common warm up and thermalisation times, the whole start-up and warm-up process could take on average around an hour and a half.

Through extensive diagnostics, modelling and eventual full redesign we were able to overcome these debilitating problems and re-engineer our laser system to a very high level of both spatial and temporal quality, needed to pursue our line of research.

2.2.1 Optical Design Issues of the Original System

The first amplification stage of our laser system used the multi-pass architecture configured to run with thirteen passes through the Ti:Sa crystal. Due to the high fluences used to pump Ti:Sa crystals, amplified spontaneous emission (ASE) can exist as a significant and unwanted background. ASE is however generated in a full 4π sterad angle in the crystal and thus does not have the same divergence as the pulses being amplified. To limit the amount of ASE in the multi-pass system an aperture mask can be placed in the beam path, with apertures large enough for the pulses to pass through, but small enough to limit the propagation of the more divergent ASE. The size of the apertures and the placement of the mask is critical because even subtle clipping of the amplified pulses will result in diffraction, leading to a hole in the intensity profile of the beam after propagation of the pulses. We experienced this exact problem caused by the aperture mask in our system, seen in Fig. 2.1 and initially chose to overcome this by using a spatial pinhole filter. This filter relies upon a pinhole aperture in the Fourier plane of a lens to filter out the high frequency components carried in the beam and results in a much higher quality beam. The aperture size dictates the level of filtering, however too small an aperture will result in beam clipping and a loss of energy in the beam. Our pinhole filters are made from diamond which albeit hard, had a life-time limited to a few months before laser damage became apparent.

High power DPSS laser pumping of Ti:Sa crystals can be achieved with frequency doubled neodymium-doped yttrium aluminium garnet (Nd:YAG) at 532 nm or neodymium-doped yttrium lithium fluoride (Nd:YLF) at 527 nm. There are many manufacturers of these

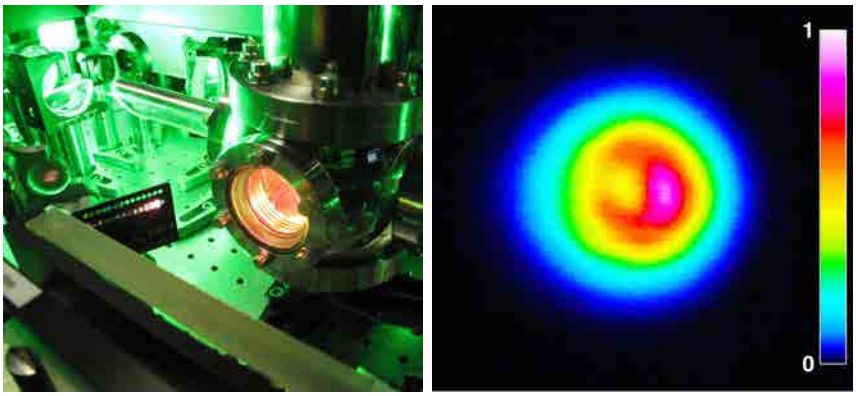

FIGURE 2.1: Left) The 14-hole aperture mask, showing the strong build up of ASE in the last 4 passes. Right) Beam profile showing the hole in the beam caused by the aperture mask

pump lasers, all of which have similar characteristics including multi-mode operation and an M^2 value quoted from around 15 up to and over 25. The quality of beams produced at these high powers is usually not that great out of focus therefore the most common practice is to image the laser rod into the Ti:Sa crystal where you are most likely to have the best quality beam to pump with.

When designing a high power femtosecond laser system there are some critical parameters to take into account. The gain characteristics for example depend on the size of both the seed and the pump beams which in optimal conditions are matched in size. Gain is then inversely proportional to the beam size however intensity is also inversely proportional to beam size, so a balance needs to be found between having sufficient gain without intensities that can damage optical components including the Ti:Sa crystal. Associated with the intensity is the B-integral which is a measure of the non-linear phase

shift and is defined as:

$$B = \frac{2\pi}{\lambda} \int n_2 I(z) dz \tag{2.1}$$

where n_2 is the non-linear refractive index, I is the optical intensity and λ is the wavelength. B-integral is cumulative as it propagates through each optical element and the B-integral sum should be kept below unity to avoid the accumulation of non-linear phase. This phase is extremely difficult to compensate for owing to being non-linear and highly modulated.

The second amplification stage of our laser system consisted of two Ti:Sa crystals through which the pulses propagated in a "race-track" type architecture. The pulses were amplified three times in each crystal before being ejected and sent to the compressor. In the interest of compactness (the footprint of this stage was 1.5 m × 0.5 m), the manufacturer thus needed to use short focal length optics to focus the 527 nm pump beams in the the Ti:Sa crystals which resulted in very small focal spots (substantially smaller than the required seed sizes to ensure sustainable intensities and reduction of B-integral). To overcome the beam size mismatches the pump laser foci were placed 3 cm to 6 cm out of the crystals which resulted in grossly inhomogeneous spatial pump profiles being used to amplify the seed beam. This in turn resulted in very poor spatial profile of our amplified Ti:Sa beam. An optimal output quality could be chosen by arbitrary misalignment of the three pump beam profiles to try ensure the most Gaussian like spatial profile.

The laser system originally shipped with a compressor comprised of gold-coated ruled copper gratings. Near field images of the beam

profile showed vertical lines across the entire beam which were related to the gratings' manufacture method (mechanically ruled).

Figure 2.2 shows a beam profile taken with our beam profiler. The intensity distribution is very far from Gaussian, despite the misalignment procedure described above. The vertical lines present in the beam are a manifestation of the poorly ruled compressor gratings.

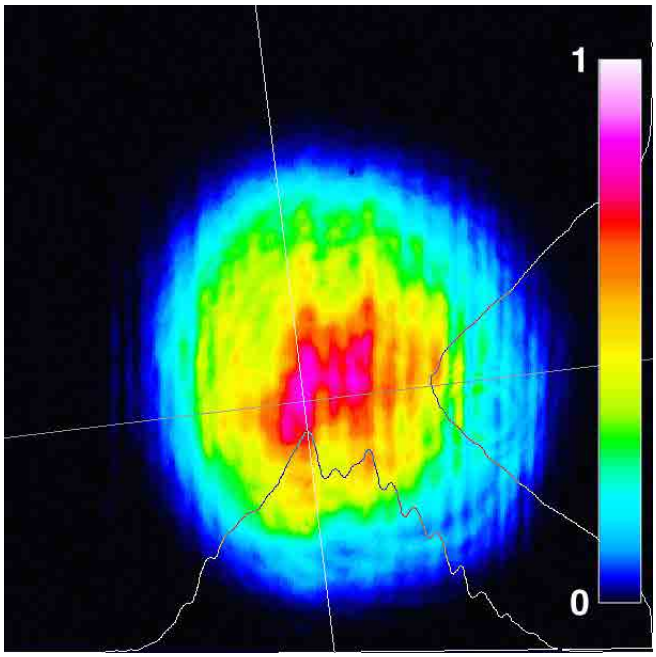

FIGURE 2.2: A beam profile of the original system output

2.2.2 Spatial Characterisation

Too often, a beam quality is defined purely by its M^2 value or by looking at a small focal spot whose size is often approaching a few times the pixel size of the beam profiling camera. In the case that intensity on focus is the only requirement and there is sufficient energy

to not rely on a diffraction limited focus to achieve the high intensities, then these figures of merit may be sufficient. On the other hand if the laser is to be used to pump a multi-stage non-linear frequency converter, such as an optical parametric amplifier (OPA), the beam quality needs to be measurably excellent to ensure an acceptable level of efficiency in the frequency conversion process. The demands of our research most certainly places us into this second category so we need a more critical measure of the beam quality.

A technique employed to get a more realistic idea of beam quality is to take a "beam caustic". This entails focusing a more or less collimated beam with a lens, where the choice of focal length and the beam size ensure that over a distance of a few Rayleigh ranges, a beam profiling camera can be used to view the profile from pre-focus to focus to post-focus. Optimal selection of the focal length will ensure that the beam profiler's full size is used at the out-of-focus extremes. A ruler bolted to the optical table provides a guide for the camera to capture an image at regular intervals through the caustic.

The output of the beam caustic gives you the beam profile in focus, as well as the profiles in planes before and after the focus which give a far more realistic idea of the quality of the beam as a function of propagation. When the laser beam's intended use is to pump a multi-stage OPA whose stages are pumped with collimated telescope-downsized versions of the beam, a clean beam caustic tells us that there are no poor quality planes which could end up in the same amplification plane of the OPA.

By the time the laser system was working quasi-immaculately, a beam caustic setup could be put together at a similar pace to that of a formula one pit crew!

Figure 2.3 shows the beam caustic of our fully amplified Ti:Sa system measured after the compressor. Here the beam is downsized after the compressor to a size of 12.5 mm $1/e^2$ diameter and then focused with a 50 mm diameter, $f = 1000$ mm lens. The camera is translated 180 mm with an image taken each 10 mm. The top left profile can be described as the "best" quality in this caustic, however the profiles after the focus reveal just how important it is to characterise the beam with such a technique. This characterisation also revealed that our method of output profile optimisation through misalignment of the pump beams may have resulted in a "good" profile in the one plane, however unacceptably poor in other planes.

2.2.3 Thermal Lensing

In this regime of high power optical pumping of a laser medium, thermal lensing becomes a critical factor. The refractive index of a material is temperature dependant, characterised by its so-called thermo-optic coefficient dn/dT, where n is the refractive index and T is the temperature. The near Gaussian intensity profile of the pump laser beam induces a non-uniform heating profile across the beam, which in turn induces a non-uniform refractive index that manifests as a thermal lens. Neglecting the stress induced change in refractive index as well as the distortion of the curvature of the input and output faces of the laser medium, The focal length f of the thermal lens is then given by [5]:

$$f = \frac{2KA}{dN/dTP_{pump}} \tag{2.2}$$

where K is the thermal conductivity, A is the beam area and P_{pump} is the optical pump power. The goal is to reduce the effect of thermal

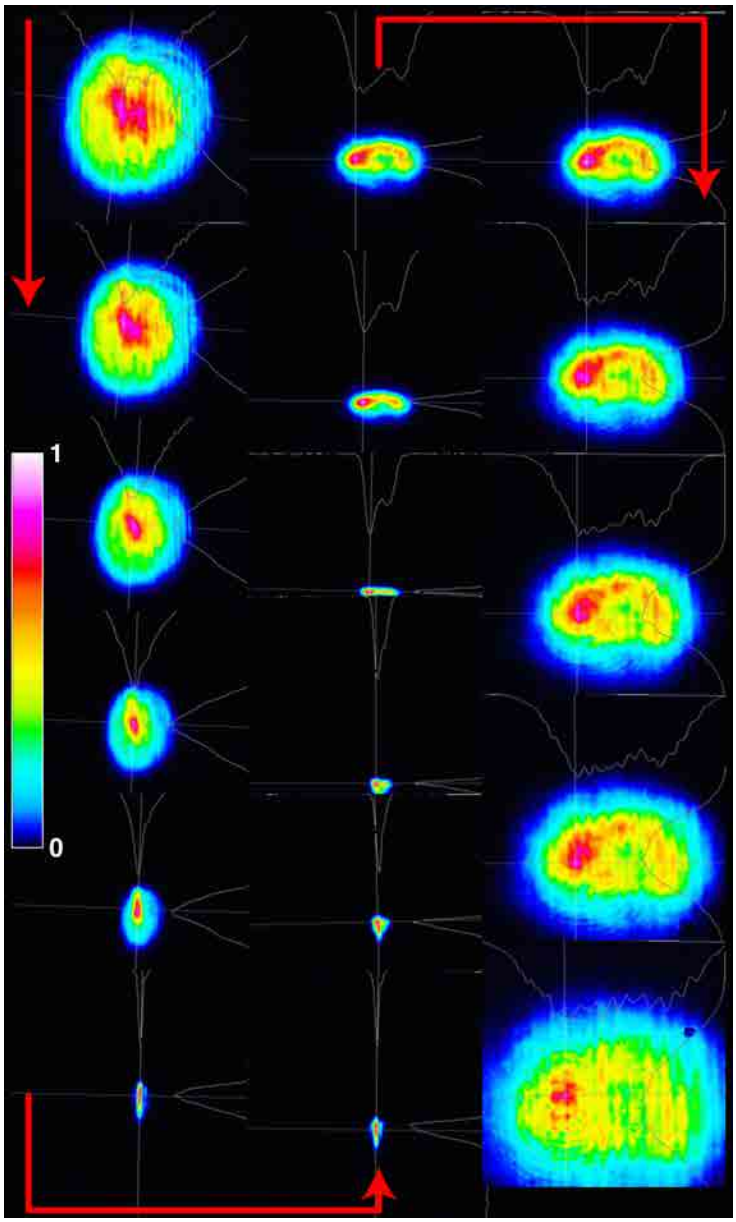

FIGURE 2.3: A beam caustic of the original system output. Images are recorded at 1 cm intervals ranging from 5 cm before the focus to 13 cm beyond the focus. 0.25 cm Increments separate the focal image from its neighbours

lensing as much as possible, which means having f as large as possible. The thermal conductivity of sapphire is maximum around 29 K (see appendix A.1) therefore cryogenic cooling of the sapphire results in reduced temperatures and temperature gradients and hence a longer focal length thermal lens.

Thermal lensing manifests spatially as a distortion to the beam. Compounding the problem is the different thermal conductivity of the two crystal axes of Ti:Sa resulting in an elliptical thermal lens as can be seen in Fig. 2.4. The amplified output beam viewed using a beam profiler is shown at four different powers achieved by increasing the pump laser power. (3 kHz operation showing output energies of 10.3 mJ to 13.1 mJ). The elliptical distortion starts to become clear around 36 W.

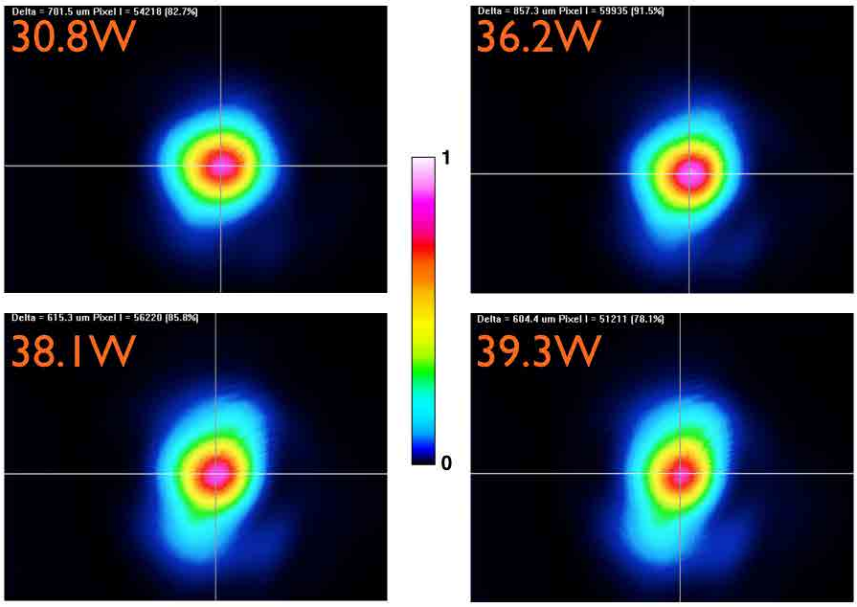

FIGURE 2.4: Thermal lensing shown for different pump laser powers

Our Ti:Sa system relies upon cryogenic cooling [6] of the Ti:Sa crystals to minimise thermal lensing. Two Gifford-McMahon Cycle cryogenic coolers (Cryomech CHCS120) circulate 35 K helium in gas phase in a closed-cyle loop offering around 120 W of cooling power at 80 K. All vibrating components are kept out of the laboratory in an adjacent service corridor, minimising vibrational noise to the laser system. A copper cold-finger is connected via vacuum flex-lines to the cryo-cooler in the service corridor. The long flex-lines sacrifice some cooling per unit length, however the advantage of minimal vibration near the laser system far exceeds the disadvantage of a slightly reduced cooling capacity

The Ti:Sa crystals are held in copper crystal mounts buffered with a 250 μm layer of indium. The indium ensures a more homogeneous contact between the various hard and superficially incompatible surfaces. These mounts are then connected to the copper cold fingers (also buffered with a 250 μm layer of indium). Some improvements were however needed to optimise the design of the original crystal mounts. At cryogenic temperatures, the cold-finger-mounted crystal mounts are necessarily located in vacuum chambers pumped down to 5×10^{-6} mbar prior to cryogenic cooling

2.3 Ti:Sa System Redesign

2.3.1 Crystal Mount Thermal Simulations

Finite element analysis (FEA) simulations were performed first on basic configurations of two different copper crystal mount architectures to ascertain the optimal cooling conditions, with regards to two parameters: 1) Proximity of the crystal to the cooling surface

and 2) the volume of copper surrounding the crystal. Two geometries were tested, each with the heat source placed near as well as far from the cooling surface. The first geometry replicates the manufacturer's existing design and the second simulates having significantly more volume of copper around the heat source. These initial basic simulations were performed assuming a quasi-point heat source. The results of the FEA simulation can be seen in Fig. 2.5.

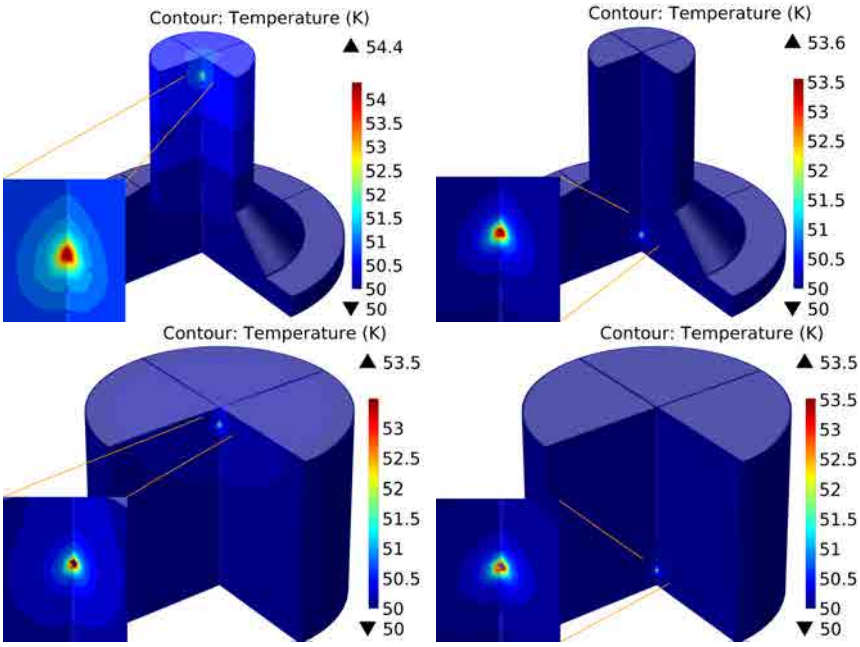

FIGURE 2.5: Top left) Original mount - Heat source far from cold finger. Top right) Original mount - Heat source near to cold finger. Bottom left) Cylinder mount - Heat source far from finger. Bottom right) Cylinder mount - Heat source near to cold finger. Insets show zoomed in view of the heat source.

In all simulations, the cryo cooler is mounted on the base of the mount henceforth known as the cold finger side. The top two simulations in Fig. 2.5 represent the actual mount characterized by having a relatively small amount of copper surrounding the point heat

source. The top left result, having the heat source far from the cold finger shows the highest temperatures with the largest temperature gradients, corresponding to the poorest performing configuration. The bottom two simulations in Fig. 2.5 represent a mount with significantly more copper surrounding the point heat source. The bottom right result, having the heating source close to the cold finger shows the smallest temperature gradients and thus corresponds to the optimal configuration.

2.3.2 Crystal Mount Design

Based on the results of these simulations I designed a new crystal mount using computer aided design (CAD) that kept the crystal as close as possible to the cold surface and surrounded it with as much copper as possible. The crystal mount is comprised of two parts facilitating the clamping of the crystal between them. I opted to separate the parts into two "D" shapes, ensuring that both sides were in direct thermal contact with the cold finger. Also taken into consideration in the design was to leave access to the crystal for inspection and cleaning purposes. The final CAD design can be seen in the top left of Fig. 2.6. Shown in the top right of Fig. 2.6 is the mount which was subsequently manufactured in our mechanical workshop. In addition to the mount design, a custom vacuum chamber was needed, to facilitate the low profile mount still being centred in the chamber. I again used CAD to design the chamber which was then manufactured elsewhere.

A more in-depth FEA simulation (details in appendix A.1) was performed on the new design illustrating that it could provide a significant improvement on the original (see Fig. 2.6). The concentration of heat in the crystal also highlights the high thermal conductivity of

cryogenic sapphire compared to the surrounding indium and copper.

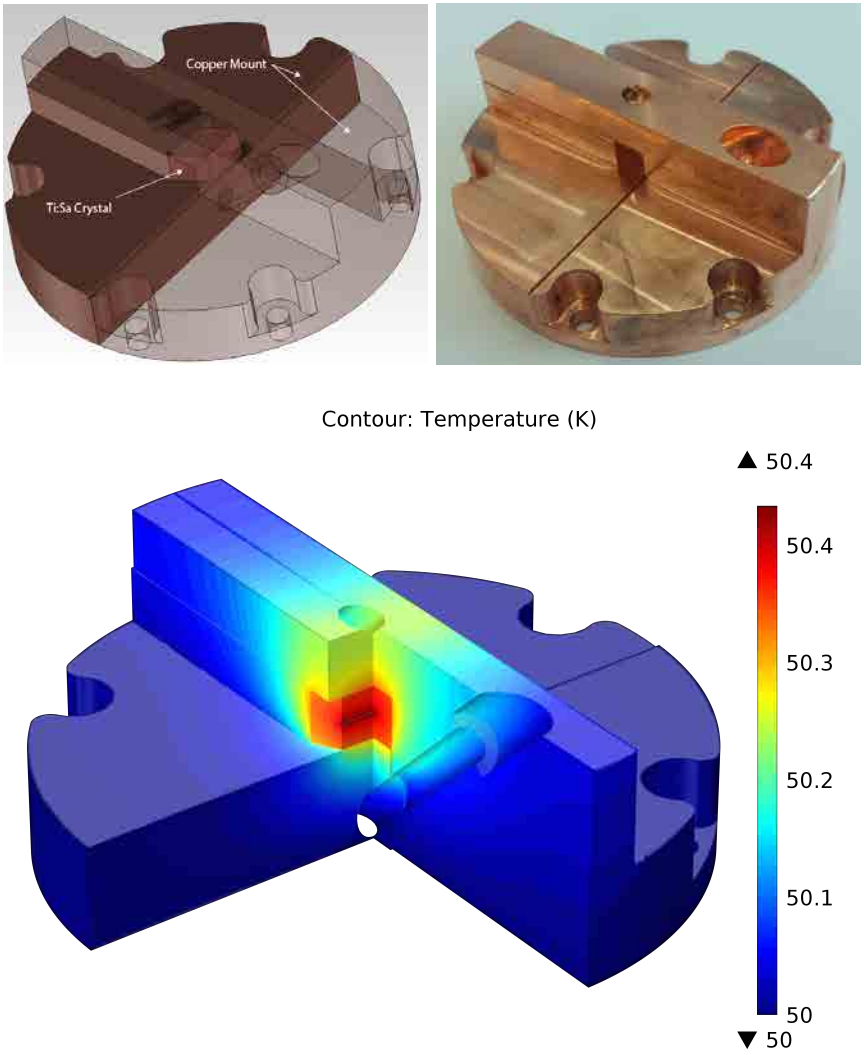

FIGURE 2.6: Top left) CAD design of the new crystal mount. Top right) Copper mount fabricated in our machine shop. Bottom) Finite element analysis simulations of the new crystal mount.

2.3.3 Cryogenic Regenerative Amplifier

With an ultimate goal of having the best beam quality possible, we decided to redesign the first amplification stage using a regenerative (regen) amplifier architecture. A hemispheric cavity design was chosen and initially simulated in Rezonator [7]. This cavity layout is beneficial for higher average power systems as the most sensitive optical element of the cavity, the Pockel's cell can be placed at one end of the cavity where the beam is largest. The Ti:Sa crystal can then be placed at the other end of the cavity, where gain can be optimised with the smaller beam. An added benefit of this layout is that the end mirror placed close to the crystal can act as an optical fuse which damages before the Ti:Sa crystal, which when brewster cut (as in our case) experiences a larger effective beam area than that of the end mirror. The thermal lens generated by high power optical pumping needs to be taken into account when designing the regen cavity. The focal length of the thermal lens is calculated for 25 W of optical pumping (our required pump power) and shown on the top left plot of Fig. 2.8. This thermal lens can then be introduced to the cavity modelling in Rezonator by placing a "thin lens" at the same plane as the Ti:Sa crystal, with a focal length calculated using equation (2.2) for a range of values around the typical temperature measured on the copper mounts. The expected beam radii in the cavity are shown on the right plot in Fig. 2.8. The blue curve represents no thermal lensing and thus the hemispherical cavity design as expected. The yellow curve however gives more realistically expected beam sizes based on a thermal lens present in the Ti:Sa crystal. Indeed this was verified experimentally twice. The first time, when the regen cavity was assembled and the limits were being found, optical damage did occur at a point close to where the beam is the smallest in the yellow curve. The second time this

occured was when the cryo-cooler cooling this crystal began to fail, resulting in poorer cooling, a higher temperature and effective dragging of the smallest beam size onto an optic. The bottom left plot of Fig. 2.8 shows the expected focal length of the thermal lens for a range of pumping powers. This cavity will not resonate stably with a thermal lens focal length below 1.5 m corresponding to a pump power of ≈ 35 W. Also noteworthy is that a change of only a few degrees can really influence the cavity architecture, for example at 44.5 K (green curve), the beam is now smallest in the Pockel's cell and largest in the crystal, which could destroy the Pockel's cell crystal and/or have very low gain due to the poor size matching of the pump and the seed. This highlights the requirement to have highly stable cryogenic systems control such as the cryo-coolers we use.

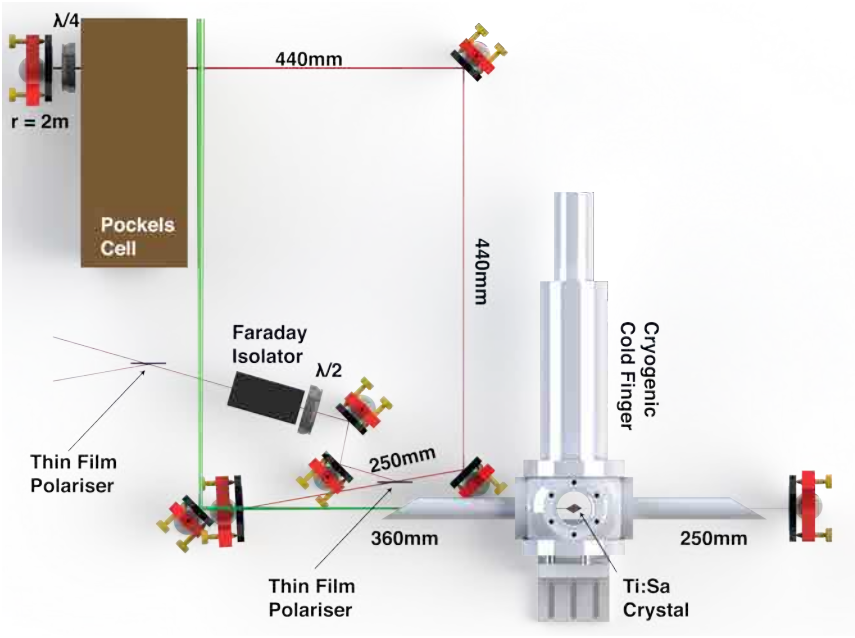

FIGURE 2.7: Regenerative amplifier layout. All mirrors are flat HR800 dielectrics, unless labelled otherwise.

The cavity roundtrip length is 3.48 m corresponding to a roundtrip

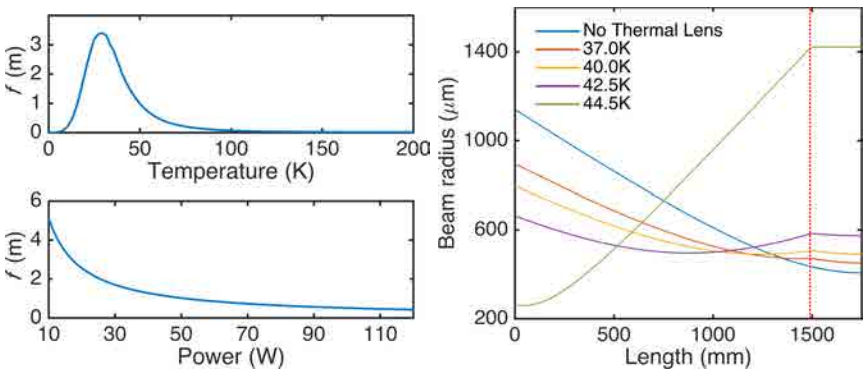

FIGURE 2.8: Top left) Thermal lens focal length expected from 25W of optical pumping as a function of crystal temperature. Bottom left) Thermal lens focal length expected for pump power from 10 W to 120 W (for a fixed temperature of 40 K). Right) Regen cavity beam sizes for different crystal temperatures. The dotted red line indicates the position of the Ti:Sa crystal

time of 11.6 ns. The pockel's cell (Bergmann) can cleanly switch in less than 8 ns which allows us to optimally open and close our regen cavity. The optimal regen build-up is in 12 round trips, achieved by optically pumping with 25W. The output profile is outstanding with an energy of 2.3 mJ. Based on the Rezonator modelling, a pump beam size of 500 μm is chosen to optimise the pump and seed size overlap.

A drawback of the high-gain regenerative amplifier is the more dramatic spectral gain narrowing that can occur. We use our Dazzler to counter-act gain narrowing through careful amplitude shaping of the seed pulse spectrum. A 85% depth hole was introduced to the spectrum with a width of 70 nm centred at 780 nm. The amplified spectrum could initially only support a pulse duration of >50 fs and after the spectral shaping could support a 38 fs pulse duration.

2.3.4 Cryogenic Multipass Booster Amplifier

Redesign of the second stage of amplification had the ultimate goal now of maintaining the regen's excellent beam quality. Optical table space was not a concern, so compactness could be neglected. A multi-pass architecture, illustrated in Fig. 2.9 consisting of only two passes was needed to achieve the goal energy of 10 mJ. Ideally the multi-pass architecture would re-image the beam at the crystal plane from the preceding pass, on to the following pass, which would be achieved through $4f$ imaging, however due to a combination of long focal length optics ($r = 5000mm$) and seed reshaping due to the thermal lensing, the $4f$ imaging system can be relaxed by shortening the collimated propagation (to 3.2 m). Rezonator[7] was again used to model the pass by pass beam sizes as part of the design phase.

Gain calculations suggested a suitable spot size of 500 μm, which is easily achievable with the high M^2 seed and the correct choice of focusing optics. To obtain this size of beam in focus from the pump lasers however, a more complicated negative telescope system was designed to first expand the beam and then gently focus it over a long distance. The key improvement on the original system was to use the pump laser in this fashion, having its focal plane in the Ti:Sa crystal. In this configuration despite the low M^2 values typically achieved with pump lasers, the optimal pump beam profile is usually found at the focus. Pumping the Ti:Sa crystal with 35 W, we achieve the 10 mJ and maintain good beam quality.

The total B-integral for the system calculated for worst case scenario is 2.42, which although is more than 1, is below the guideline of 3 to 5 at which non-linear effects such as self-focusing will start to manifest. Details of the calculation can be found in appendix A.2.

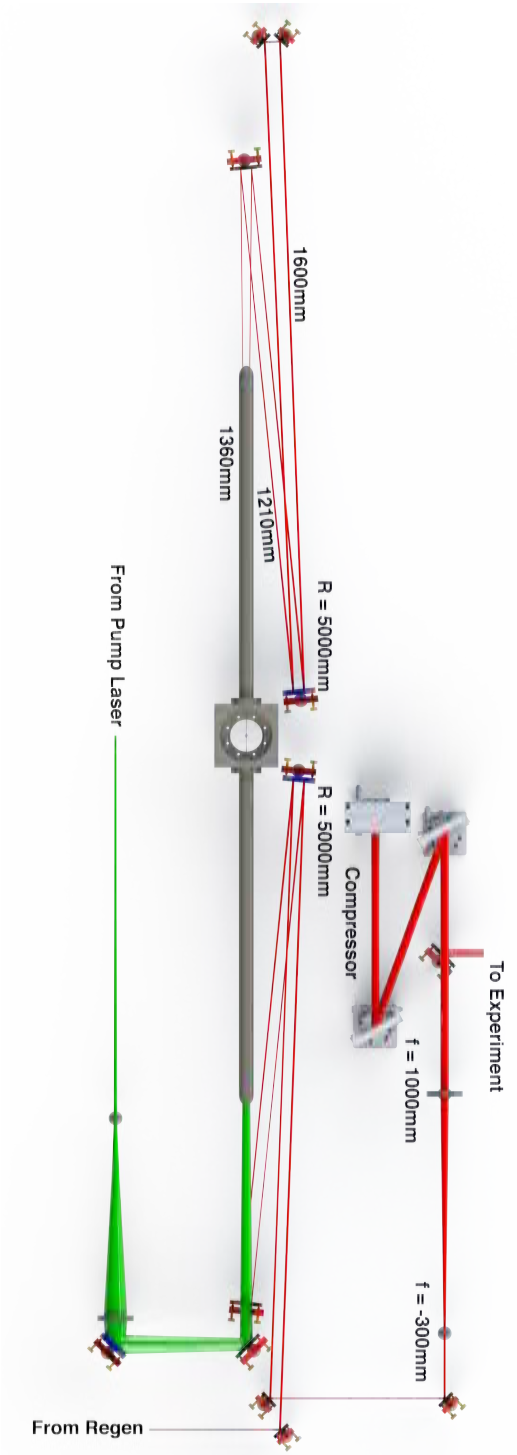

FIGURE 2.9: Booster amplifier layout. The long tubes extending from the vacuum chamber ensure a larger spot size on the brewster windows, negating peak intensity damage to the windows and mitigating B-integral.

2.3.5 Compressor Grating Upgrade

The only solution to the vertical lines in the beam, was to replace the compressor gratings. To ensure that suitable replacements were purchased, I first calculated the dispersion characteristics of the existing stretcher/compressor configuration using ray tracing as well as through basic analytic formulae [8]. Optica was used to perform the ray-tracing, shown in Fig. 2.10 along with a table showing the dispersion characteristics of the stretcher and compressor. In the CPA scheme, the compressor has to reverse the dispersion introduced by the stretcher and any other dispersive elements in the beam path. The ratio of group velocity dispersion (GVD) to third-order dispersion (TOD), in the stretcher and compressor is proportional to the grating separation. In the compressor, the separation is controlled via a motorised actuator to enable live modification of the output pulse compression. In addition to this, the Dazzler (discussed in chapter 3) can be used for fine tuning of the dispersion characteristics, including relevant higher order dispersion terms, such as fourth-order dispersion (FOD) to ensure successful pulse re-compression.

Based on the calculations we opted for some holographically etched gratings which are not mechanically ruled. Photolithographic techniques are used to etch interference-fringe generated grooves on a substrate and subsequently gold coat them. A Zerodur substrate was selected due to its high thermal conductivity to mitigate the effects of high average powers, such as localised warping of the gratings.

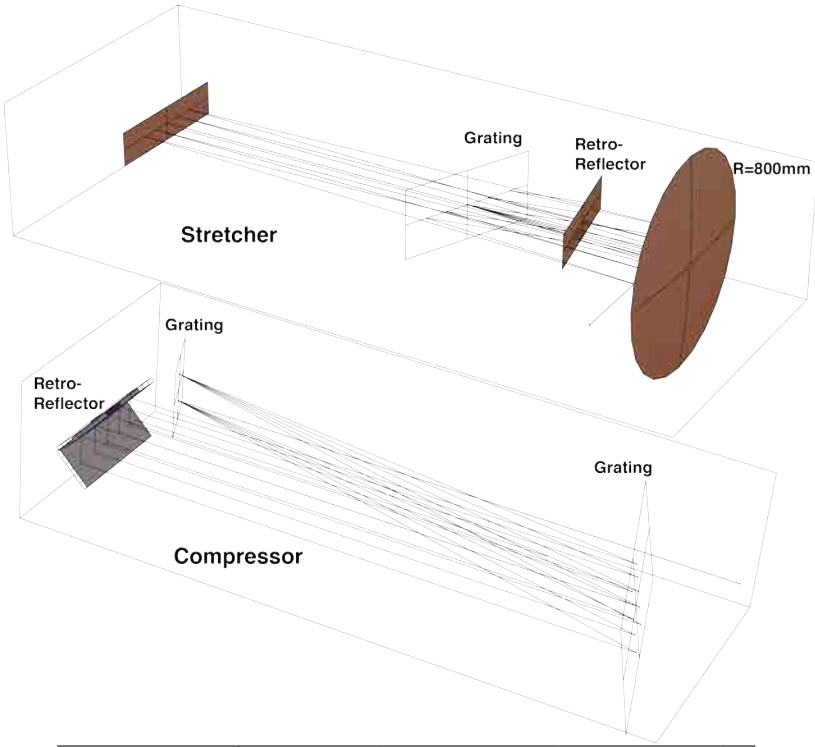

Component	GVD (fs^2)	TOD (fs^3)	4OD (fs^4)
Stretcher	7.4×10^5	-1.4×10^6	3.8×10^6
Compressor	-7.1×10^5	1.6×10^6	-5.7×10^6

FIGURE 2.10: Optica ray tracing of top) Stretcher and bottom) Compressor. Tabulated dispersion characteristics are also included

2.4 Ti:Sa System Characterisation

2.4.1 Temporal Characterisation

A home-built second harmonic generation (SHG) frequency resolved optical gating (FROG) device (described in appendix A.4) was used to characterise the compressed pulse duration. The FROG retrieval algorithm yields a compressed pulse duration of 40.5 fs shown in Fig.

2.11 close to the Fourier transform limit of 38 fs

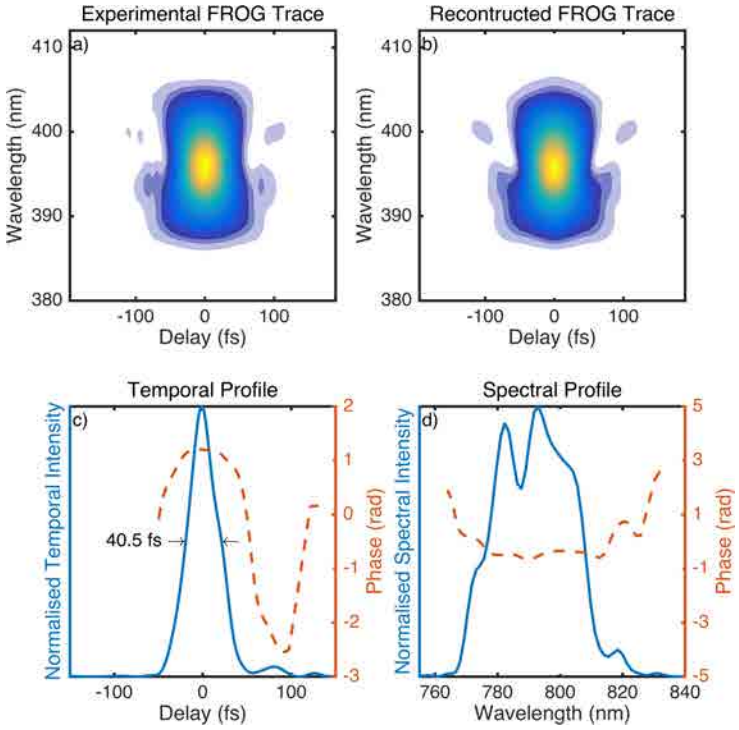

FIGURE 2.11: FROG measurement of the fully amplified Ti:Sa pulse: a) Measured bFROG trace b) Reconstructed bFROG trace c) Retrieved temporal intensity (blue curve) and temporal phase (red curve), d) Reconstructed spectrum and spectral phase (red curve)

As discussed in section 2.2.1 to prevent unwanted non-linear phase accumulation B-integral needs to be kept to a minimum, so to calculate the acquired B-integral in the system a pulse duration of the stretched pulse is needed. With a pulse duration expected in the hundreds of picoseconds, pulse characterisation is not so trivial. The pulse is still too short to be measured using the fastest photo diodes and as a consequence of the stretched duration, its peak intensity

can be below the threshold needed to induce a non-linear process usually required for pulse characterisation. Very modest amplification of the signal can be used to boost the pulse energy to enable peak intensities capable of inducing the desired non-linear effect. Extreme care is needed to ensure that the seed is not amplified too much resulting in optical damage. A simple intensity autocorrelator [9] was built for this purpose, using a thick beta barium borate (BBO) crystal to maximise second harmonic signal. Autocorrelation of the moderately amplified signal results in a pulse duration of 170 ps assuming a Gaussian temporal intensity distribution.

2.4.2 Spatial Characterisation

In stark contrast to Fig. 2.2, Fig. 2.12 shows the current beam profile, which can only be described as immaculate for a multi-millijoule, 1 kHz ultrafast laser beam.

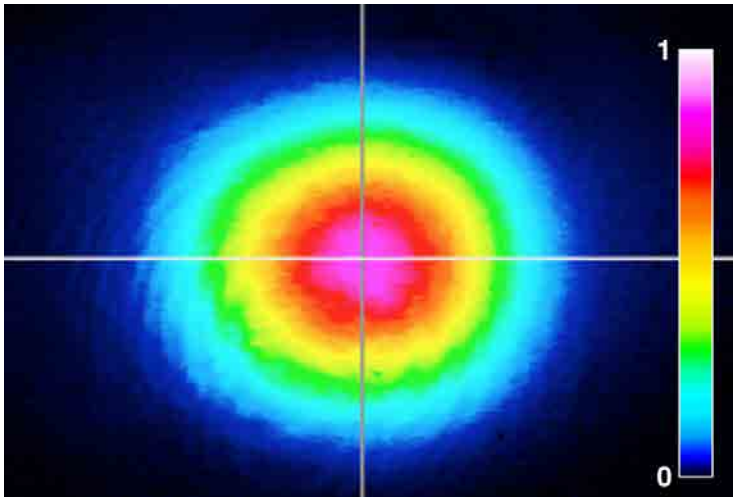

FIGURE 2.12: A beam profile of the current system output

2.4.3 System Stability

Instability in the amplified pulses from amplifiers can predominantly come from two sources. Initially if not driven in saturation the stability is inherited from the stability of the pump lasers. once driven in saturation the stability of the amplifier can exceed that of the pump lasers. The measured instability of our pump lasers (Photonics Industries DM50-527) is below 1% measured over 45 minutes. Spot sizes are chosen in the booster stage to provide the required power output while keeping the gain modest(≈ 5) and the high spatial profile quality. The desired power output is achieved in only two passes, which does not facilitate full saturation however owing to the high stability pump lasers yields a photodiode characterised shot to shot stability of $\approx 0.75\%$ measured over 45 minutes.[1]

The stability of the system is attributable not only to the pump lasers, but as importantly to the infrastructure supporting the full laser system. The laboratory has been designed to keep all sources of vibration and audible noise outside. I have also designed and built a full enclosure system that encloses the laser system as well as the rest of the optical table that houses the rest of the laser-dependant components that are discussed in this thesis. One of the components most sensitive to air currents and contamination, the compressor is also housed in an additional enclosure within the main enclosure. A complex air-conditioning system then ensures that a controlled flow of temperature and humidity controlled clean air is supplied to the laser hutch.

Beyond the measurable stability, lies the reliability and usability of the system. The system is now as "turn-key" as a high average

[1] 45 minutes was the measurement time to minimise disruption to laser use, however continued stability at these levels is normal during day to day operation.

power Ti:Sa system can be. Start-up procedure has been reduced to around ten minutes with an additional twenty minutes needed for thermalisation. On average the oscillator needs "tweeking" every six weeks, the regen every six months and the booster stage only needs realignment if the the regen output has been changed. As you will read in this thesis - water window high harmonics are generated starting from this laser source and it has become routine to have these harmonics on the detector within one hour from a completely off start-up. To date, the longest continual run of the system lasted around 80 hours after which the entire system was still rufnning perfectly - but the experiment was over!

2.5 1.85 μm Few Cycle, CEP Stable, Laser Pulses

2.5.1 TOPAS

The HE-TOPAS OPA is a commercially available product, so I will only give a brief description of the most important aspects of it that make it a critical part of our water-window soft X-ray radiation source.

The OPA is a travelling wave, white-light seeded optical parametric amplifier consisting of three amplification stages. The OPA is pumped with the full 7 mJ compressed output of the Ti:Sa system. A small fraction of this is used for white light generation and the rest is split three-fold to pump each of the three OPA stages, all of which use BBO non-linear crystals. The crystals are angle tuned to frequency down-shift the incoming 800 nm pump to a 1400 nm signal and an 1850 nm idler. The idler pulses have an energy of 1 mJ and a pulse duration around 45 fs.

As the white-light seed originates from the pump pulses, the idler is self carrier envelope phase (CEP) stable [10]. The expected CEP stability arises from the phase relationship of the three pulses involved in the parametric process

$$\phi_{idler} = -\pi/2 + \phi_{pump} - \phi_{signal} \tag{2.3}$$

The signal and the pump have the same phase and cancel each other out, leaving the phase of the idler offset by $\pi/2$ but insensitive to pulse-to-pulse phase fluctuations

The only significant modification to the OPA is in the third and final stage of amplification which is originally configured in a collinear alignment. In this configuration, dichroic optics are required to separate the signal and idler, with the idler being transmitted through the optic. The dispersion imparted by this final optic is unacceptable for our application, so we reconfigure the final stage to run in a non-collinear geometry with a very small angle between the pump and signal/idler of 0.2 degrees, limiting the spatio-temporal distortion of the pulses, while allowing spatial separation of around 1 cm of the idler after 2.5 m of propagation

2.5.2 Hollow-core Fibre Pulse Compression

The technique is described in more detail in section 3.2.2 and has been very successfully implemented with Ti:Sa systems at ≈ 800 nm. It has also been applied to longer wavelength laser pulses [11, 12] resulting in few-cycle laser pulses. We employ this technique to compress our 1.85 μm pulses. A static pressure of 1.1 bar of argon is applied to a sealed external glass tube housing the 250 μm hollow-core fiber (HCF). The spectral broadening is shown in Fig. 2.14 where the TOPAS idler output spectrum shown in red has a Fourier

transform limit (FTL) of 44.8 fs and the blue spectrum after spectral broadening in the HCF has a FTL of 10.2 fs. A coupling efficiency of around 50 % is achieved through the HCF resulting in pulse energies around 500 μJ.

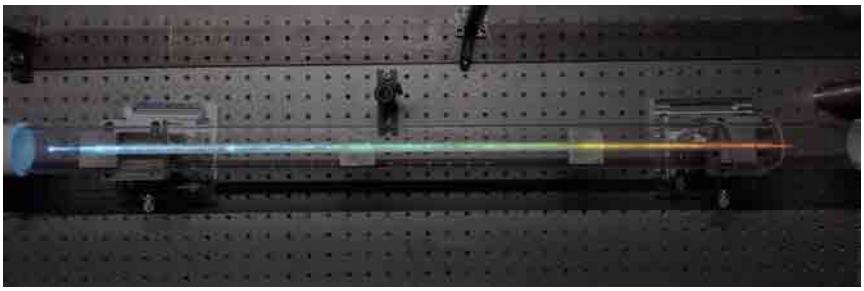

FIGURE 2.13: Photo of the Hollow-core Fibre

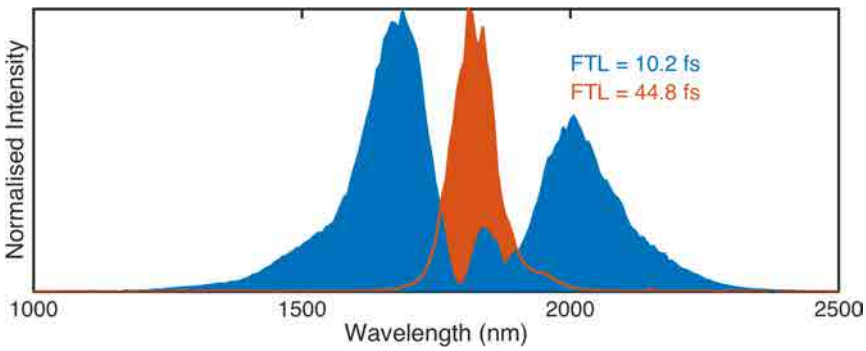

FIGURE 2.14: Spectra showing the spectral broadening of the hollow-core fibre

As described in [11, 12] compression of the pulses is achieved via propagation in bulk. HCF pulse compression described in chapter 3 around 800 nm, requires chirped mirrors for compression that impart negative group delay dispersion (GDD). The zero dispersion of many common glasses, such as fused silica, calcium flouride and BK7, lies close to 1300 nm. These materials impart positive GDD at 800 nm and negative GDD at 1850 nm. Compression can thus be

achieved via propagation through suitable material. Historically, an RG1000 filter was used to reject sub 1000 nm radiation and luckily this material provided the optimal dispersion compensation.

2.6 Few Cycle 1.85 μm Pulse Characterisation

Pulse characterisation at around 2 μm presents some technical difficulties pertaining to detector sensitivities around these wavelengths. Second harmonic generation based techniques can suffer from silicon's poor sensitivity around 1000 nm making device calibration extremely critical.

2.6.1 Temporal Characterisation

A home-built SHG frog described in appendix A.4 is used to characterise the pulses that have been spectrally broadened in the HCF and then compressed by the bulk RG1000 filter. An ultra-thin pellicle is used as the beam-splitter, whereafter the pulse replicas are focused by a $f = 50\,mm$ off-axis parabolic mirror into a 10 μm BBO crystal. The second harmonic signal is then refocused onto a spectrometer (Ocean Optics HR4000). The spectrometer has a silicon based detector claiming spectral sensitivity from 200-1100 nm however both spectral and most importantly intensity (irradiance) calibration is essential. Spectral calibration is performed using a mercury-argon calibration source (Avantes - AvaLight-CAL). A tungsten halogen bulb (Avantes) is used to calibrate irradiance prior to usage of the spectrometer in the FROG.

Figure 2.15 shows the results of the second harmonic FROG obtained with optimal compression, resulting in a pulse duration of 11.2 fs.

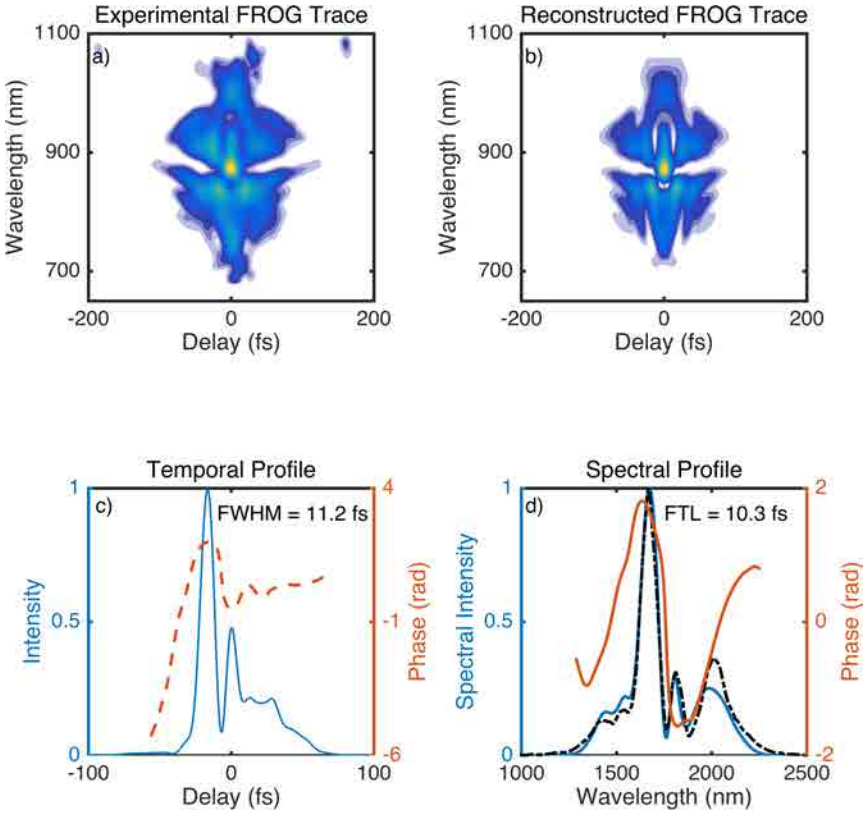

FIGURE 2.15: Compressed pulse FROG a) an experimentally retrieved FROG spectrogram. b) The algorithmically reconstructed spectrogram. c) The temporal profile of the pulse and d) the spectral intensity

2.6.2 System Stability

A fast photo-diode sensitive to 1.85 μm radiation is used to monitor the shot to shot stability of the TOPAS output and of the HCF

output, with stabilities of 1.5 % and 1.0 % respectively measured over 1 hour.[2]

2.6.3 Carrier to Envelope Phase

The CEP describes the relationship between the electric field oscillations and the electric field envelope. Control of the CEP is essential when generating repeatable isolated attosecond pulses discussed in chapter 6 and the generation of repeatable few-cycle driven X-ray spectra discussed in chapter 5

Characterisation of CEP can be implemented in two ways: in-loop and out-of-loop. The out-of-loop method relies on a sample of the beam being sent to a device capable of measuring the CEP such as the stereo above threshold ionisation (ATI) [13], in which the directionally biased photo-ionisation of a gas by a polarised laser pulse is used to extract the CEP. More commonly however an in-loop measurement is used. The most common implementation of this makes use of *f to 2f* interferometry, in which a pulse can be spectrally self-referenced to yield the CEP.

In our setup, the HCF generates more than an octave of bandwidth, simplifying heavily the *f to 2f* spectral requirements of the technique. The small fraction of the beam that is reflected off the RG1000 pulse compressor, is focused into a type-1 100-μm-thick BBO crystal, frequency doubling the broad bandwidth. A half-wave plate then rotates the signal to allow for interference with the remnant fundamental. The interference spectra are recorded using a spectrometer. A LabView program interfaces with the spectrometer, performing a Fourier analysis of the fringe pattern and calculates the CEP jitter.

[2] 1 hour was the measurement time to minimise disruption to laser use, however continued stability at these levels is normal during day to day operation.

It also interfaces with a digital to analogue converter connected to a piezo-electric transducer which is placed in the delay stage of the second OPA pump optics. With this active stabilisation we are able to mitigate the slow CEP drift, caused by external environmental influences.

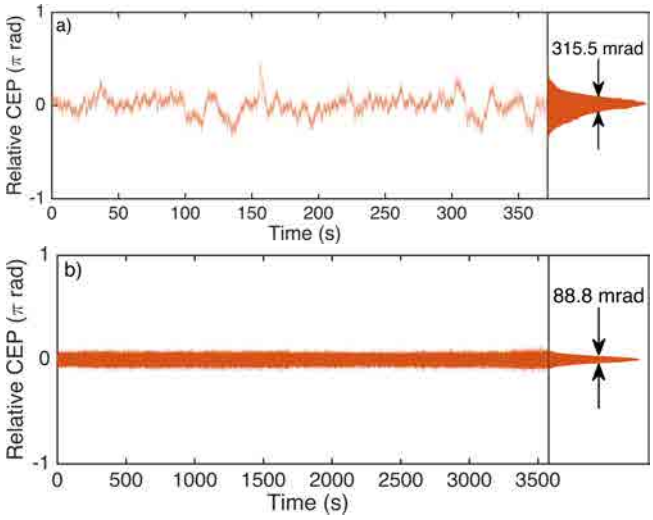

FIGURE 2.16: a) Intrinsic CEP stability measured after the HCF. b) CEP stability with slow feedback loop enabled

Using this detection and control system, we characterise our intrinsic CEP jitter at 316 mrad, which is measured single-shot over 6 minutes. After activation of the feedback loop, the CEP jitter is reduced to 89 mrad measured over an hour. These results are shown in Fig. 2.16. Subsequent to this measurement, during a 72 hour experimental data acquisition, the CEP jitter remained below 100 mrad which is a record for this type of system.

To conclude this chapter, a schematic diagram showing the full system is shown in Fig. 2.17.

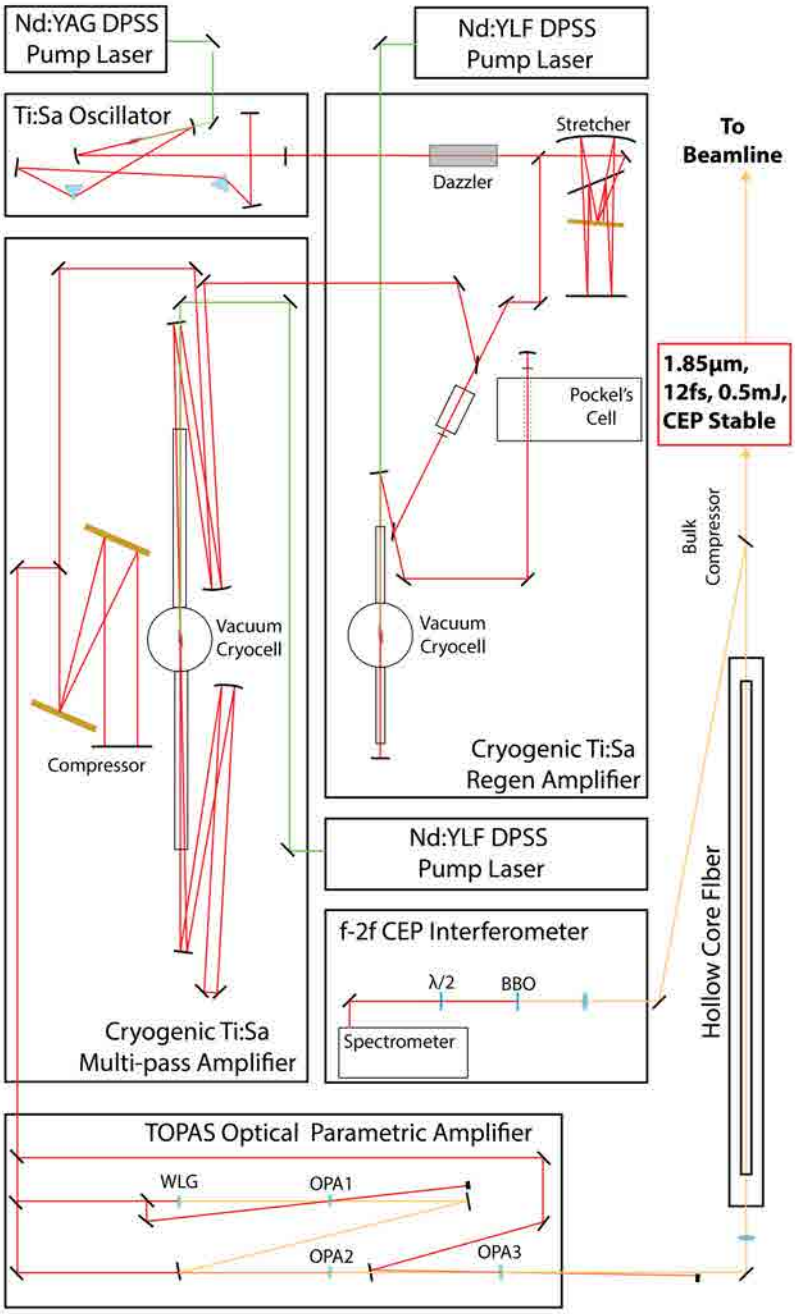

FIGURE 2.17: Schematic representation of the complete source. Abbreviations described in the chapter, apart from: white light generation (WLG) stage of the TOPAS.

Chapter 3

Pulse Characterisation of Few-Cycle Pulses using an Acousto-optic Programmable Dispersive Filter

3.1 Introduction to Pulse Characterisation

With the successful generation of femtosecond duration laser pulses came the challenge of how to characterise these ultrashort durations. The fastest electronics and photodiodes are only capable of picosecond response times making direct measurement impossible. Very soon after the first pulsed laser operation, the first pulse measurement based on autocorrelation was performed [9]. In autocorrelation, the laser pulse and a replica are combined in a non-linear

medium, with the ability to control the delay of the pulses with respect to each other. While autocorrelation does give a pulse duration, very limited further information is available. To fully characterise the pulse and retrieve both the intensity and the phase, spectral data needs to be recorded too. The 1990s saw the introduction of two measurement techniques namely FROG [14] and spectral phase interferometry for direct electric-field reconstruction (SPIDER) of ultrashort optical pulses [15]. The field of pulse characterisation is already mature and the numerous evolutions of the main techniques have already filled many PhD theses. Briefly though, in their most basic forms: FROG is an autocorrelation in which a spectrogram is recorded as a function of the inter-pulse delay. An iterative algorithm can then be used to reconstruct this spectrogram yielding the pulse duration derived from it's intensity and phase. The SPIDER techniques also uses multiple pulse replicas interfered in non-linear media, yielding a spectral interferogram. Fourier analysis (a non-iterative process) of the interferogram can be used to extract the phase and the pulse duration can then be deduced.

3.1.1 Dispersion

Both of these measurement techniques are optical techniques and thus special care is needed when designing a measurement device, particularly with regards to interaction between an ultra short pulse and material. To illustrate this point a basic calculation shows that a 5 fs pulse propagating through 1 mm of fused silica is temporally stretched to 16.6 fs, whereas a 30 fs pulse propagating through the same amount of material is barely temporally stretched at all to 30.1 fs. The refractive index $n(\lambda)$ of a material is wavelength dependent ($n(\Omega)$ in frequency space). This implies that the wavelengths

comprising the spectrum of a short pulse will travel through materials at different velocities. This is called dispersion and is often described mathematically by a Taylor expansion of the derivative of the propagation constant k. The first three orders of dispersion are given below:

$$\frac{dk}{d\Omega} = \frac{1}{c}\left(n - \lambda\frac{dn}{d\lambda}\right) \tag{3.1}$$

$$\frac{d^2k}{d\Omega^2} = \left(\frac{\lambda}{2\pi c}\right)\frac{1}{c}\left(\lambda^2\frac{d^2n}{d\lambda^2}\right) \tag{3.2}$$

$$\frac{d^3k}{d\Omega^3} = -\left(\frac{\lambda}{2\pi c}\right)^2\frac{1}{c}\left(3\lambda^2\frac{d^2n}{d\lambda^2} + \lambda^3\frac{d^3n}{d\lambda^3}\right) \tag{3.3}$$

where the propagation constant k is defined as:

$$k(\Omega) = \sqrt{\frac{\Omega^2}{c^2}n^2(\Omega)} \tag{3.4}$$

The control of dispersion can be considered one of the most important aspects of ultra-fast optics. The CPA scheme for example, so deeply enshrined in the field relies on dispersion control to stretch and then re-compress pulses. Pushing the limit of pulse durations down to the few-cycle regime requires an even greater control of dispersion, owing to the broad bandwidths required to support such short pulses.

3.2 Few-Cycle Pulse Generation

Currently, amplified Ti:Sa laser systems produce pulses in the 14.8 fs [16] to >40 fs range. When shorter pulses are desired either to perform few-cycle pulse experiments, or to seed attosecond generation schemes, such as high harmonic generation (HHG), techniques need to be employed to generate even shorter pulses. Ti:Sa oscillators can

be configured to generate few-cycle pulses directly however at very modest energy levels.

A relationship between the spectral bandwidth and the temporal duration of a pulse exists and is most simply defined by the time-bandwidth product:

$$\Delta\nu\Delta t \geq F, \tag{3.5}$$

where $\Delta\nu$ is the frequency bandwidth and Δt is the pulse duration, both defined at FWHM. F is a factor that depends on how the pulse shape is defined, for example $F = 0.44$ for a Gaussian shaped pulse. The time-bandwidth can give an indication of how close a pulse duration is with respect to the Fourier transform limit of the pulse's spectrum. The time bandwidth product also alludes to the inverse proportionality between pulse duration and spectral bandwidth. The following basic formula can be used to relate the two properties.

$$\Delta\lambda = \frac{F\lambda_c^2}{\Delta\tau c}, \tag{3.6}$$

where $\Delta\lambda$ is the required spectral bandwidth in nm, λ_c is the central wavelength and c is the speed of light.

For example to support a Gaussian shaped pulse duration of 5 fs, a spectral bandwidth of at least 188 nm centred at 800 nm is required. Keeping in mind that the typical spectral width of a Ti:Sa amplifier is around 25 nm, significant spectral broadening would be needed to reduce the pulse duration.

Various spectral broadening techniques exist, all of which rely upon non-linear pulse propagation through a medium. At sufficient pulse intensities, the medium's refractive index can become intensity dependant, which is known as the Kerr effect, a third order non-linear effect. When an ultra-short pulse propagates through a non-linear medium, the refractive index is modulated following the temporal

evolution of the pulse. This modulation results in a shift of the instantaneous phase ergo a frequency shift of the pulse. This process is known as self phase modulation (SPM) and is the dominant non-linear effect used to broaden spectra:

The intensity dependant refractive index is described by:

$$n(I) = n_0 + n_2 I \tag{3.7}$$

where n_0 is the linear refractive index and n_2 is the second order non-linear refractive index.

$$I(t) = I_0 \exp\left(\frac{-t^2}{\tau^2}\right) \tag{3.8}$$

where τ is half the pulse duration. The change in refractive index is given by:

$$\frac{dn(I)}{dt} = n_2 I_0 \frac{-2t}{\tau^2} \exp\left(\frac{-t^2}{\tau^2}\right) \tag{3.9}$$

and the instantaneous phase shift is:

$$\phi(t) = \omega_o t - kz = \omega_0 - \frac{2\pi}{\lambda_0} n(I) L \tag{3.10}$$

where L is the distance travelled by the pulse. The frequency shift is

$$\begin{aligned} \omega(t) &= \omega_0 - \frac{2\pi L}{\lambda_0} \frac{dn(I)}{dt} \\ &= \omega_0 + \frac{t 4\pi L n_2 I_0}{\lambda_0 \tau^2} \exp\left(\frac{-t^2}{\tau^2}\right) \end{aligned} \tag{3.11}$$

From this equation, for $t < 0$, the leading edge of the pulse shifts to lower frequencies and for $t > 0$ the trailing edge shifts to higher frequencies.

Importantly, the new frequencies generated will also suffer from dispersion induced by propagation through the medium, resulting in the front of the pulse moving faster than the back of the pulse. The spectrally broadened pulse may have the bandwidth now to support a short pulse, however the pulse is chirped i.e. its constituent spectral components do not arrive at the same time.

3.2.1 Filamentation

The phenomenon of laser pulse filamentation [17] is a vast research topic in itself and although having shot a few beautiful laser filaments in the laboratory I have not made use of them for the purpose of spectral broadening and pulse compression. Filamentation can be thought of most simplistically as a competition between two non-linear effects: self-focusing and plasma defocusing. If the laser power exceeds the critical power, defined below, self-focusing can occur.

$$P_{cr} = \alpha \frac{\lambda^2}{4\pi n_0 n_2}, \tag{3.12}$$

where $\alpha \approx 1.9$ for a Gaussian beam, λ is the central wavelength, n_0 is the linear refractive index and n_2 is the non-linear refractive index

As the intensity further increases due to self-focusing, the laser pulses start to ionise the medium and generate a plasma, which can in turn defocus the pulses. These two processes compete until some balance is found in which a self guided channel of light forms, known as a filament. The spectral broadening process described above as well as other non-linear processes generate the broadened spectrum, where after compression techniques are required to compress the broad spectrum. Extensive research is still undergoing to

characterise and understand the complex dynamics of laser filamentation, but most relevant to this thesis is few cycle pulse generation through filamentation [18–21].

3.2.2 Hollow-Core Fibre Pulse Compression

A hollow-core fiber is a wave-guiding structure composed of a glass tube with a hollow core. SPM can be induced by focusing an ultrashort laser pulse with sufficient intensity into a HCF, which is filled with a noble gas such as argon or krypton, first shown by Nisoli et. al. [22]. As a result of SPM, spectral broadening of more than an octave can be achieved [22–24].

Unlike solid-core fibers which rely on total internal reflection to transmit light, HCFs rely upon grazing incidence reflections on the internal hollow core. By satisfying a coupling condition [24], interference due to the multiple reflections ensures that only a fundamental mode propagates in the HCF. Assuming efficient coupling into the HCF fundamental mode, known as the EH_{11} mode, the output efficiency can exceed 50% [24]. Noble gases are used for their relatively high third order non-linearities at low pressures. The non-linearity is a function of gas pressure, making it a controllable parameter. Finally noble gases have high multi-photon ionisation intensity thresholds, which is beneficial as multi-photon ionisation is not a desired response to the intense laser field.

HCF pulse compression has resulted in sub 2-cycle pulses, using improvements to the technique such as cascading two HCFs with chirped mirror compression in between the two HCFs [25]. Differentially filling the HCF with the noble gas has also improved the coupling efficiency. Having a low gas density at the entrance of the

HCF ensures that unwanted non-linear processes are avoided and SPM occurs further down the HCF [26].

In our experiment, 700 µJ pulses are split from the Ti:Sa output and are focused into a 0.9 m HCF with a 250 µm inner core. The HCF is statically filled with 800 mbar of argon. The spectrum is broadened to support an FTL of 7 fs as seen in Fig. 3.1 where the filled red curve shows the Ti:Sa input spectrum and the filled blue curve shows the broadened HCF output spectrum. Six bounces on two pairs of Layertec ultrabroadband chirped mirrors (-40 fs^2 group delay dispersion per bounce) and two thin wedge prisms compress the pulse.

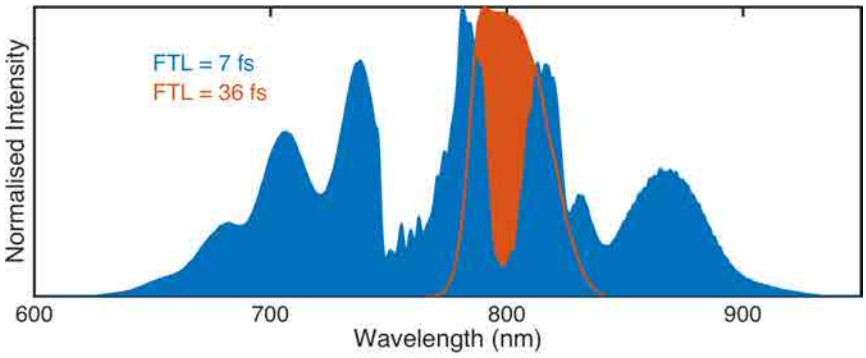

FIGURE 3.1: Spectra showing the spectral broadening of the hollow-core fibre

3.3 Acousto Optic Programmable Dispersive Filters

The idea of using an acousto optic interaction as a filter was first suggested in 1969 [27]. A lithium niobate crystal in combination

with an acoustic transducer was demonstrated as a tunable band-pass filter. The Dazzler is an acousto-optic programmable dispersive filter (AOPDF) consisting of a $25mm$ paratellurite (TeO_2) crystal, driven by a piezo-electric transducer at RF frequencies. The Dazzler acousto-optic coupling is described in the temporal domain, by:

$$E_{out}(t) \propto E_{in}(t) \otimes S(t/\alpha) \tag{3.13}$$

and in the frequency domain by:

$$E_{out}(\omega) \propto E_{in}(\omega) S(\alpha\omega) \tag{3.14}$$

where E_{out} is the optical output signal, E_{in} is the optical input signal, $S(t)$ or $S(\omega)$ is the electric signal creating the acoustic wave and α is the ratio of the speed of sound to the speed of light multiplied by the difference in refractive indices of the ordinary and extraordinary waves:

$$\alpha = \Delta(V/c) \tag{3.15}$$

In the Dazzler, the optical and acoustic signals are collinear to maximise interaction length. The electric field incident on the Dazzler is polarised in the fast ordinary axis as is the acoustic wave. When a frequency component of the electric field is in phase with a frequency component of the acoustic wave, it is diffracted on the slow extraordinary axis. The total output electric field is composed of all the diffracted frequency components that have been phase matched at various planes in the TeO_2 crystal and thus by shaping the acoustic wave, the spectral phase of the output electric field can be controlled. The amplitude of the output electric field scales with the amplitude of the acoustic wave thus offering amplitude control too.

The Dazzler is most commonly used early in the amplification chain

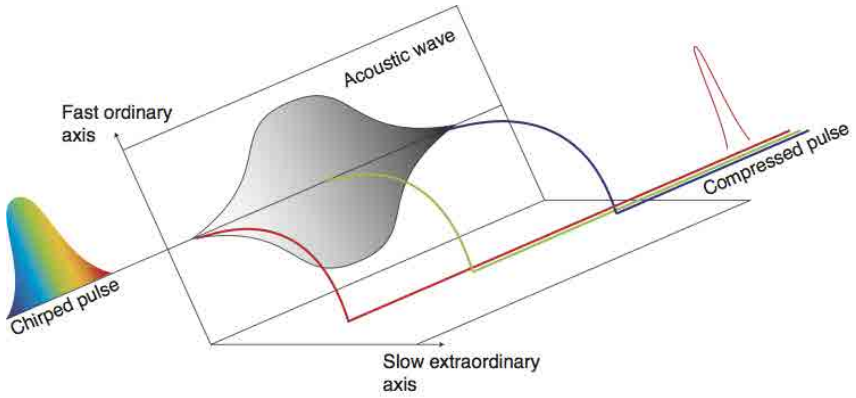

FIGURE 3.2: A schematic representation of the Dazzler [28]

of a CPA Ti:Sa system, making use of its ability to shape the amplitude and phase. The compression of the pulse at the end of the CPA system relies upon the ability of the compressor to reverse the phase generated by the stretcher and all the optical components in the amplification chain. A Dazzler can be used to pre-compensate for the higher order phase terms which are inaccessible using simple phase compensation techniques, ensuring compression down as close to the Fourier transform limit as possible. Amplitude shaping can be used to compensate for the effects of gain narrowing discussed in section 2.3.3. By placing a dip in the spectrum at the peak of the gain profile, amplification in the wings of the spectrum can be improved, retaining spectral bandwidth during amplification. Verluise et al. have used a Dazzler in this fashion to extend the amplified spectrum from 35 nm to 75 nm, measured at FWHM [28].

The Dazzler can also be used to generate pulse replicas through amplitude shaping. This ability of the Dazzler is the foundation of the Phazzler pulse measurement device, described in the next section.

3.4 Phazzler Pulse Characterisation

The versatile Phazzler can be programmed with various filters corresponding to many variants of FROG and SPIDER [29], however the work in this thesis has been performed solely with the baseband FROG (bFROG) variant.

3.4.1 The bFROG Method

The CEP can also be arbitrarily chosen using an AOPDF. The implication of this is that unlike a standard Michelson interferometer built with mirrors, CEP can be chosen and maintained for each delay step of an autocorrelation. For CEP=0 the interferometric trace has no fast oscillations which can significantly reduce the number of delay steps needed to sufficiently sample a FROG trace [30]. The baseband FROG (bFROG) is an interferometric version of FROG which makes use of the above described "trick". The AOPDF is programmed with a spectral filter $1 + e^{-i[(\omega-\omega_0)\tau+i\phi]}$, resulting in a spectrometer signal:

$$I_{\mathrm{bFROG}}(\tau,\omega) \propto \left| \int \left(E(t) + E(t-\tau)e^{i\phi} \right)^2 e^{2i\omega_o t} e^{-i\omega t} dt \right|^2 \qquad (3.16)$$

where $E(t)$ is the envelope of the electric field in the time domain, τ is the delay between pulse replicas.

A theoretically generated pulse having a 50 nm FHWM Gaussian spectrum and no spectral phase is used to generate the expected bFROG results shown in Fig. 3.3

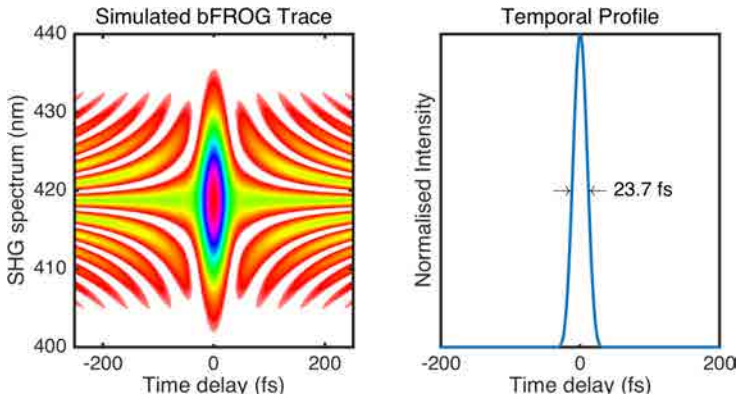

FIGURE 3.3: left) Theoretical bFROG trace, right) Temporal profile of the pulse

3.4.2 Phazzler Limitations

The Dazzler TeO_2 crystal is a highly dispersive medium itself, so before any pulse shaping can take place it has to compensate for its own intrinsic dispersion. For a 25 mm TeO_2 crystal as used in the AOPDF, the second and third order dispersion terms are calculated to be $GDD_o = 12425\,\text{fs}^2$ and $TOD_o = 8132\,\text{fs}^3$. $GDD_e = 14585\,\text{fs}^2$ and $TOD_o = 9625\,\text{fs}^3$ (See Appendix A.5). Once this self-compensation is performed, the available pulse shaping window left is not sufficient to be applied to a broad bandwidth typical from an HCF. External pre-compensation is thus needed to increase the available shaping window bandwidth.

The pair of grisms shown in Fig. 3.4, constructed using Thorlabs gratings (GTI25-03) and prisms (PS908L-B), have been used for dispersion pre-compensation into the Phazzler. Grisms have been chosen for their ability to impart both negative second and negative third order dispersion [31], needed to pre-compensate for the TeO_2 dispersion.

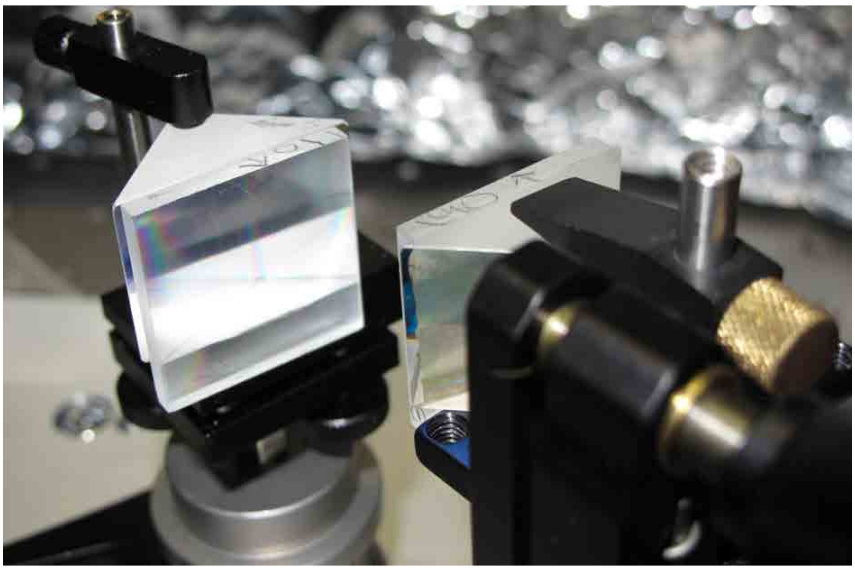

FIGURE 3.4: The grism pair used to pre-compensate the AOPDF dispersion

Unfortunately it is not as simple as tuning the grisms to pre-compensate for all of the dispersion of the AOPDF. Diffraction efficiency of the AOPDF is proportional to the acoustic signal that is applied to it. If the AOPDF was programmed with zero phase, diffraction would occur at a single plane in the AOPDF crystal approaching zero percent efficiency. A balance is thus found in applying enough phase to ensure sufficient diffraction efficiency while maintaining a pulse shaping window that can accommodate the broad bandwidth of the few-cycle pulse being measured. The grism pair separation can then be adjusted to pre-compensate for the necessary AOPDF phase. An optimum grism spacing of 15 mm was found which corresponds to a chirp of approximately -7600fs^2 (equal and opposite to the dispersion of the AOPDF).

3.4.3 Phazzler Phase Calibration

When characterising ultra-short pulses more stringent requirements are placed on the measurement device to ensure that no additional phase is imparted to the pulse by the device. In the few-cycle regime this is even more critical as even a very thin optic could still heavily chirp the pulse to be measured. To prevent this from happening setups can be constructed using all reflective optics, or by using ultra thin optics such as a pellicle to generate the pulse replicas - however extreme care is still required to ensure that the arms of the interferometer are phase balanced.

Our characterisation device relies intrinsically on highly dispersive elements both for pre-compensation (the grism pair) and pulse replica and delay generation (the AOPDF), so we need a calibration tool to quantify the phase difference between the input phase and the phase after propagation through the AOPDF. We use Fourier transform spectral interferometry (FTSI) [32] to infer this phase difference.

3.4.4 Experimental Setup

The extremely compact device shown in Fig. 3.5 is constructed on a 300 mm×200 mm bread board. A small fraction of the beam can be split with a flip-mounted beam splitter (BS1) and sent via an optical delay line through a second beam splitter (BS2) to a spectrometer. I will return to this part shortly. The part transmitted through BS1 is double-passed through the grism pair and then diffracted by the AOPDF. A half-wave plate rotates the diffracted beam's polarization where after it is focused into a type 1 BBO crystal via flip-mounted mirror. The second harmonic signal is then refocused into the entrance slit of a spectrometer (the remaining fundamental is however

first removed with a BG39 filter). When the flip-mounted mirror is out, the diffracted beam is recombined with the BS1 reflected beam. The beams co-propagate to the spectrometer wherein spectral interference between the two can be recorded for FTSI. BS1 and BS2 are identical beam splitters from the same batch and either arm of the interferometer consists of one reflection and one transmission through each beam splitter, ensuring a balanced interferometer.

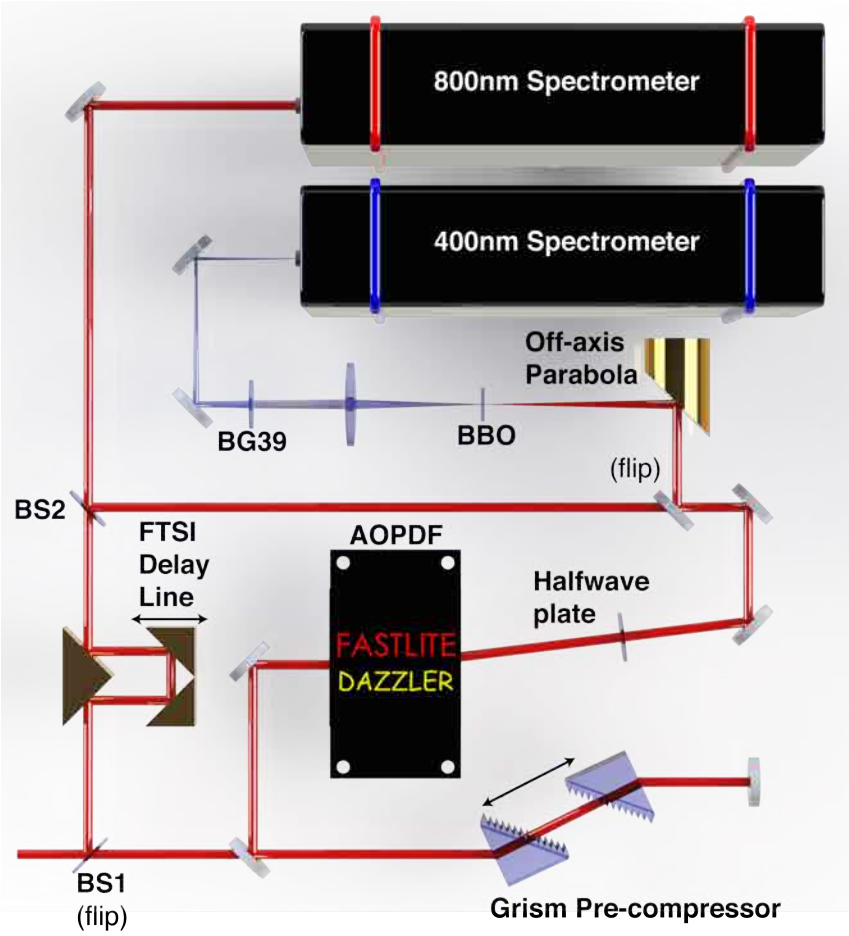

FIGURE 3.5: Schematic of the Phazzler experimental setup. All unlabelled optics are protected silver metal mirrors

3.5 Results

3.5.1 FTSI Phase Calibration

The first measurement is always the FTSI phase calibration. A LabView program was used to interface with the spectrometer, recording the interference spectrum generated by the spatio-temporal overlap of the spectrum going through the device and the spectrum circumventing the device. In real-time the residual phase is calculated. Phase could then be applied manually with the sliders in the Phazzler software up to the point where the FTSI calculated phase was relatively flat as shown in the top plot of Fig. 3.6. Finally the software was used to save this residual phase to a file which could then be loaded into the Phazzler software to flatten the small features in the phase, resulting in the phase difference shown in Fig. 3.6

3.5.2 Pulse Characterisation

Once phase calibration is complete, the temporal characterisation can be performed. The bFROG phase filters are loaded into the Phazzler software and the measurement can then be started. 165 delay steps over a spectral range from 300 to 500 nm and a temporal range of -150 to 150 fs ensure a sufficiently sampled bFROG trace. Typical integration times per delay step are 20 ms.

A pulse duration of 9.4 fs at FWHM is reconstructed by the FROG algorithm, which at a central wavelength of 800 nm implies a sub-3-cycle electric field. The results are shown in Fig. 3.7 with the experimental trace on the top left and the reconstructed trace on the top right showing excellent visual agreement. The bottom left shows the temporal profile. The spectral profile is shown on the

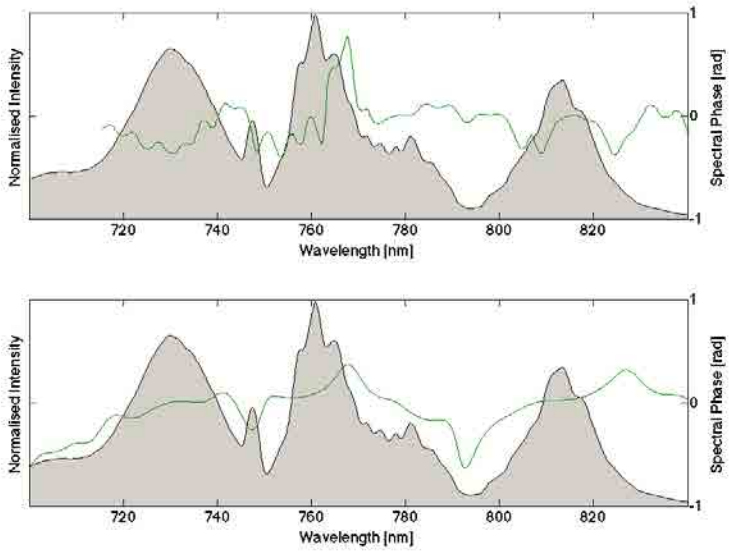

FIGURE 3.6: Top) Measured spectrum (grey shaded) and manually flattened phase (green curve). Bottom) Measured spectrum (grey shaded) and final FTSI phase (green curve) post FTSI calibration

bottom right, with the spectral phase in blue. A satisfactory match between the reconstructed (gray) and the measured spectrum (blue) is shown. This is the shortest pulse characterised with a shaper based technique to date.

3.5.3 Device Verification

As with any new pulse characterisation device, some verification of its accuracy is needed. We perform this verification by introducing a known amount of dispersion to the pulse before characterisation - in this case a 2 mm BK7 optical window. The resulting pulse duration with the BK7 window included was measured to be 23.2 fs. The full results are shown in Fig. 3.8

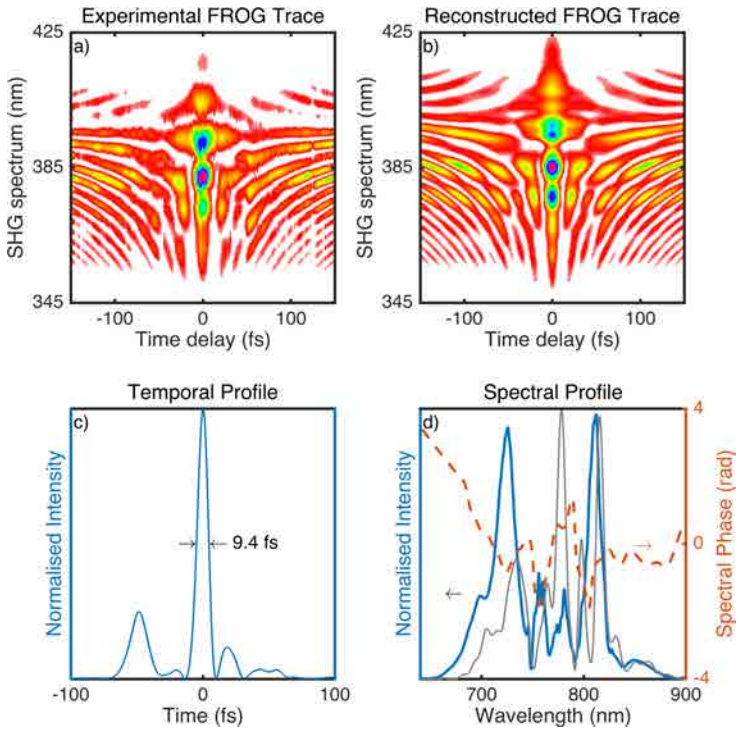

FIGURE 3.7: Few-cycle bFROG Results: a) Measured bFROG trace. b) Reconstructed bFROG race. c) Retrieved temporal intensity (blue curve), FWHM of 9.4 fs indicated. d) Reconstructed spectrum (grey), measured fundamental spectrum (black), and spectral phase (red).

The phase of the BK7 window retrieved by the bFROG is compared to the theoretically expected phase from 2 mm of BK7 showing an excellent match. As we have the FTSI delay line included we can also take an independent measurement of the the phase imparted by the window. The three phases are compared in Fig. 3.8 showing a match between all three phase curves highlighting the reliability and accurate phase retrieval and hence accurate pulse characterisation.

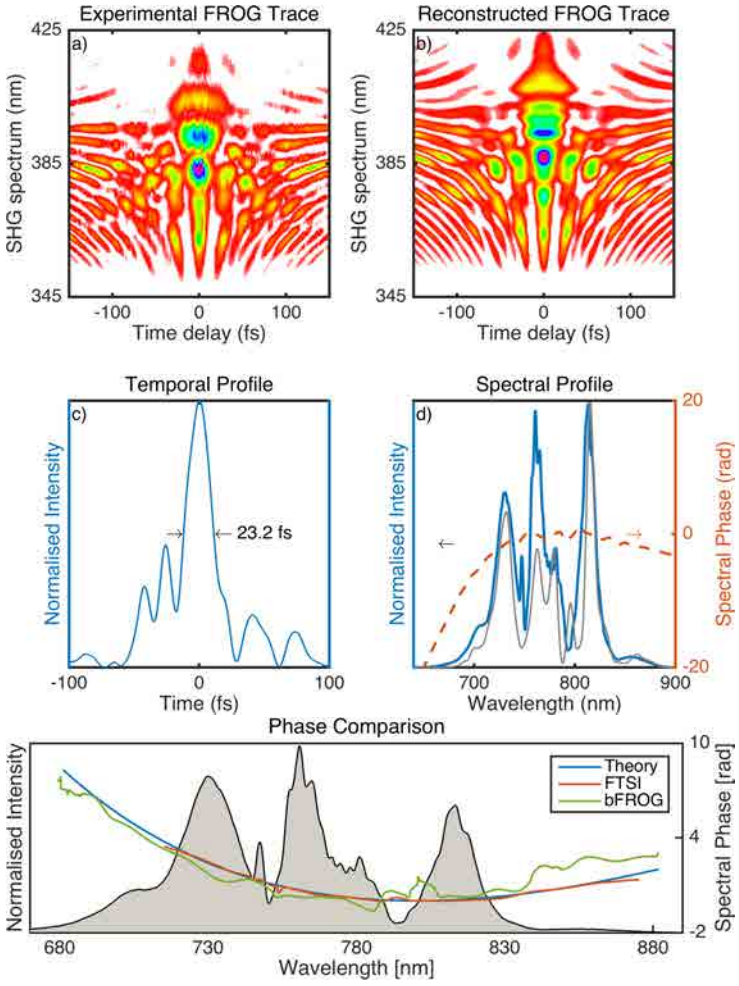

FIGURE 3.8: Top) bFROG results with 2mm BK7 in beam path. Bottom) Phase comparison, showing the measured spectrum (grey shaded) and theoretical BK7 phase (blue), FTSI phase (red) and the bFROG phase (green)

Chapter 4

Three Dimensional Pulse Characterisation of Ti:Sa Laser Pulses - The HAMSTER Technique

4.1 Introduction

When using the pulse characterisation techniques described in section 3.1, the most common practice is to either select a part of the beam to be measured with an iris, or to use the whole beam. Selecting a part of the beam then assumes that the temporal profile is the same over all parts of the beam as the measured part, which is not necessarily true. Integrating over the whole beam averages over the beam, resulting in a beam-averaged temporal profile.

Spatio-temporal coupling (STC) can be generated by many common optical components, from simple lenses to the more complicated prism and grating based stretchers and compressors used in CPA systems. Additionally non-linear pulse propagation, such as that described in section 3.2.1 [33] can result in very complex STC.

In this chapter, I'll give a brief description of the various techniques that exist to surmount this problem, whereafter I will describe the spatio-temporal pulse characterisation technique that I developed.

4.2 Spatio-Temporal Pulse Characterisation Techniques

The most common approach to facilitate spatio-temporal pulse characterisation is to combine a temporal characterization of a point in the beam with wavefront measurements taken with spectral resolution. Wavefronts can be recorded with various devices, such as a Hartmann-Shack wavefront sensor (WFS) or various forms of interferometry.

The Hartmann-Shack WFS relies on an array of micro lenses to divide a beam into a grid of sub-beamlets which focus to a CCD. Variations in the positions of the foci, with respect to calibrated points are used to reconstruct the wavefront of the incident beam. A clear contrast of requirements presents itself here though due to the fact that the focal length of a lens is wavelength dependant, whereas a short pulse intrinsically has a non-monochromatic bandwidth. If a Hartmann-Shack WFS is to be used, then spectral filtering needs to be applied to select as narrow as possible bandwidths with which to record the spectrally dependant wavefronts.

A brief outline of the existing techniques follows. The shackled-FROG technique [34] combines a standard FROG measurement combined with spatial amplitude and phase obtained using a Hartmann-Shack WFS, to infer the full electric field. The WFS is placed in the image plane of an imaging spectrometer, allowing the characterisation of the amplitude and phase of the spatially-resolved spectrum. The Striped FISH [35] technique relies on a holographic method of generating spectrally resolved holograms. The holographic image is recorded in 2D on a CMOS camera, whereafter an algorithm can process the image to yield the complete electric field. The SEA TADPOLE [36] technique relies on an extremely complex optical setup involving multiple pulse replicas being focused into single mode fibres, one of which can be translated to sample different parts of the beam. The outputs from the the fibres are then imaged onto a CCD camera via a cylindrical lens, which enables wavelength to be mapped to the horizontal axis of the camera, whereas the interference between the two replicas is recorded in the vertical axis of the camera. The 2D camera image is processed by an algorithm, yielding the complete electric field of the pulse

4.3 HAMSTER Technique

4.3.1 The Technique

The incredibly versatile AOPDF can be used both as described in chapter 3 to temporally characterise the pulse and additionally as a fully configurable band-pass filter. To stay true to the zoologically themed acronym tradition of pulse characterisation techniques I have named this device: Hartmann–Shack assisted, multidimensional, shaper-based technique for electric-field reconstruction

(HAMSTER).

The principle behind the technique is to program the AOPDF to transmit narrow spectral slices of the pulse through to the Hartmann-Shack WFS. The bandwidth of the spectral slices is selected to ensure any small spectral features are sampled. The intensity and spatial phase of the wavefront of each spectral slice are combined to form the three-dimensional spatio-spectral electric field:

$$E(x, y, \omega)A(\omega)e^{iB(\omega)} \tag{4.1}$$

Where $A(\omega)$ and $B(\omega)$ are unknown frequency dependant phase factors

A small part of the pulse (small enough to negate any large variation in spatio-temporal coupling) is selected with an iris and characterised using the AOPDF bFROG technique described in chapter 3, yielding:

$$E(x_0, y_0, \omega) \tag{4.2}$$

Where (x_0, y_0) is the point selected by the iris.

The unknown frequency dependant phase factors $A(\omega)$ and $B(\omega)$ are derived from the phase retrieval of the FROG algorithm, and can be used in equation (4.1) to produce the full three dimensional electric field of the pulse.

4.3.2 Experimental Setup

The HAMSTER device consists of four primary components combined to form a robust and relatively simple optical setup. The primary components are a Dazzler AOPDF, a Hartmann-Shack WFS (Thorlabs WFS-150), a 50um BBO crystal cut for type-I conversion

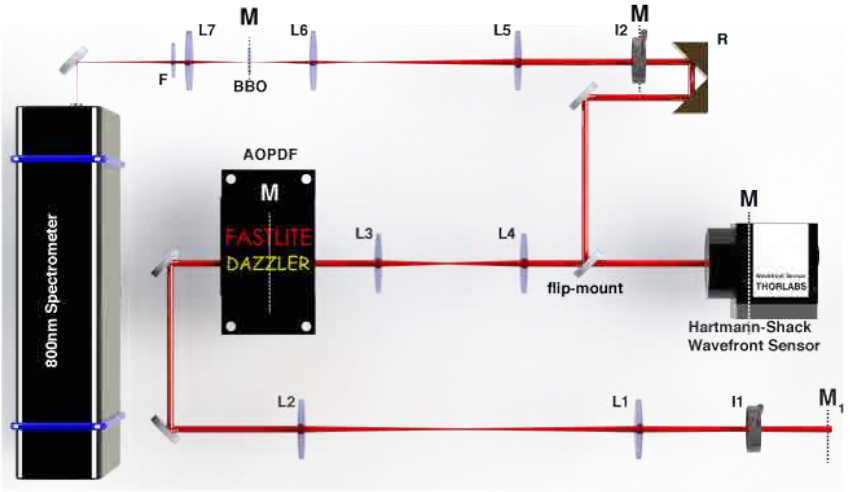

FIGURE 4.1: Schematic setup of the HAMSTER spatio-temporal measurement device; the acronyms are described in the text. Planes labelled M are conjugate to the measurement plane M_1 are indicated by dashed lines.

and a spectrometer (Avantes AvaSpec-2048-USB2) sensitive to the second harmonic spectrum. A flip-mounted mirror allows the beam to be sent into the WFS or on to the temporal characterisation.

One of the keys to the versatility of the HAMSTER device is the use of three $4f$ imaging systems. Characterising STCs such as a pulse front tilt (PFT) prove troublesome due to the fact that the combination of angular dispersion and some propagation, the constituent wavelengths are no longer spatially overlapped. Trying to temporally characterise a pulse in which not all its spectral components are present will result in at best: pulses with longer Fourier transform limits and hence longer pulses. The system of $4f$ lenses ensure that any measurement is performed at the state of the pulse at M_1 and that propagation is essentially zero through out. This is illustrated in Fig. 4.1 by the dotted x,y planes, all which are conjugate with M_1. Lenses L1 and L2 both have a focal length of $f = 500mm$

selected to prevent non-linear pulse propagation in air i.e. filamentation. Lenses L3 and L4 both have a focal length of $200mm$ chosen to maintain a compact footprint. Due to the relatively low diffraction efficiency of the AOPDF, the intensity at focus is now below that expected for non-linear effects to manifest. The final $4f$ system consisting of lenses L5 and L6 which use focal lengths of $f = 500mm$ and $f = 50mm$ respectively. This $10\times$ downsizing telescope ensures a suitable intensity in the BBO crystal. Finally lens L7 images the generated second harmonic signal onto the entrance slit of the spectrometer. A filter labelled F (Schott BG39) is used to remove the fundamental before the beam enters the spectrometer.

A retro-reflecting mirror R and iris I2 are used to enable spatial selection of the input beam, allowing the temporal measurement at any point of the beam.

4.4 Results

4.4.1 Ti:Sa Pulse Characterisation

The first pulse measured was the output of the Ti:Sa laser system, which assuming a well aligned compressor is expected not to have any significant STC. The AOPDF is programmed as a narrow bandpass filter, diffracting 2 nm spectral slices which are sent to the WFS. The programming needs to take into account the plane at which the narrow bandwidth slice is diffracted in the AOPDF crystal, ensuring that the same plane is used for each spectral slice. A sample of the data is shown in Fig. 4.2. Unlike the pulse characterisation device described in chapter 3 the HAMSTER contains dispersive lenses in the beam path. The dispersion of these lenses is calculated or measured via FTSI and the AOPDF is programmed to compensate for

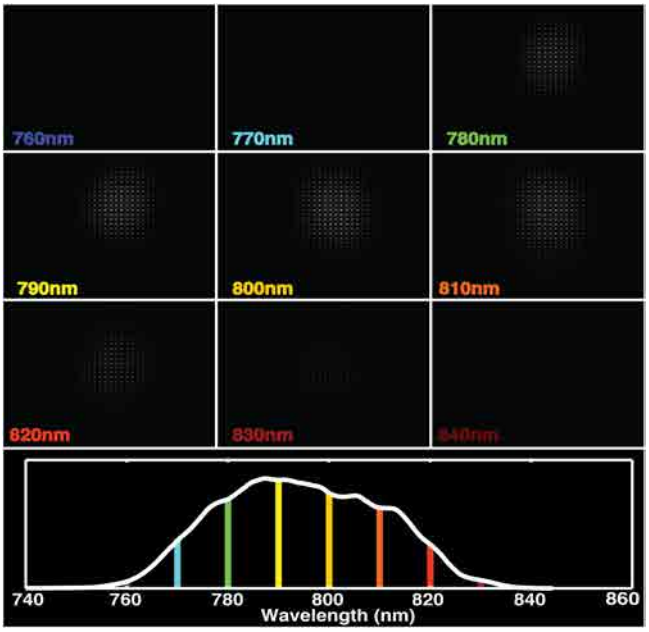

FIGURE 4.2: A sample of the raw data recorded with the Hartmann-Shack WFS, showing the spot pattern of the nine wavelengths corresponding to the colour coded to the spectral slices shown below. Raw images are not intensity normalised, hence the images for 760 nm, 770 nm, 830 nm and 840 nm are much dimmer

them. Next, iris I1 is closed to its minimum aperture (0.4 mm diameter) and a bFROG measurement is taken, whereafter the data from the two are processed to yield a spatio-temporal intensity profile shown in Fig. 4.3. The featureless blob gives the confirmation that, as expected, the spatio-temporal profile can be considered uniform across the entire beam.

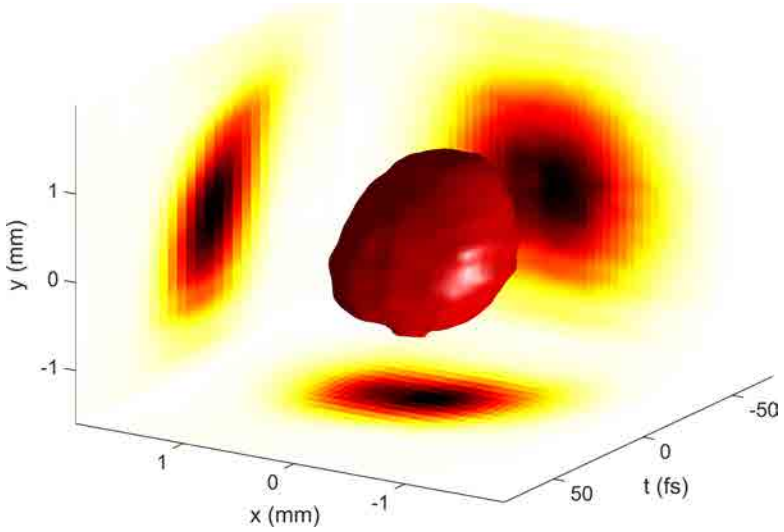

FIGURE 4.3: Spatio-temporal intensity profile, represented as a surface of 50% peak intensity, with projections along the spatio-temporal coordinate axes

4.4.2 Pulse Front Tilt

Following on from this simple device test, we investigate the spatio-temporal effects caused by one of the most common dispersive elements - the prism. An N-SF11 equilateral prism placed at the measurement plane, orientated to allow an incident angle of $58.1° \pm 0.2°$. The AOPDF was programmed to compensate for the dispersion imparted by the prism to the centre of the beam ($1000\,\mathrm{fs}^2$) so as to mitigate its effect on the spectral phase and pulse duration. The measurement is then taken in the same steps as that before (see section 4.4). The reconstructed spatiotemporal profile, represented as a surface of half-maximum intensity, is shown in Fig. 4.4. A PFT of $6.63° \pm 0.5°$ is characterised with the HAMSTER which agrees with the theoretically calculated PFT of $6.64° \pm 0.06°$ [37].

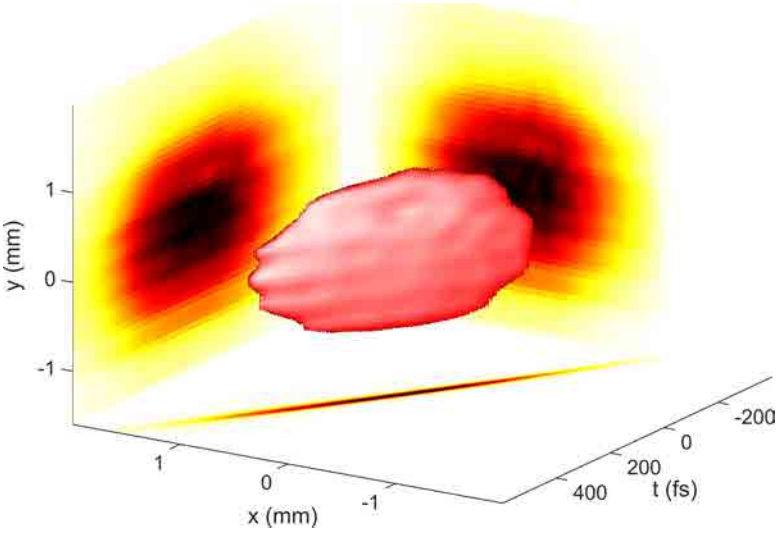

FIGURE 4.4: Spatio-temporal intensity profiles, represented as a surface of 50% peak intensity, with projections along the spatio-temporal coordinate axes. Top) Pulse from the Ti:Sa laser system Bottom) Prism-dispersed pulse clearly illustrating the pulse front tilt

4.4.3 Transverse Chirp

The next measurement was taken with the prism configuration revealing an often overlooked consequence of a beam propagating through a prism. Different parts of the beam travel through different lengths of prism glass resulting in a transverse chirp variation. We characterise this and extract the spectral phase across the beam to retrieve a linear-fit slope of $510\pm20\,\mathrm{fs}^2/\mathrm{mm}$ in good agreement with the theoretically expected value of $507\pm6\,\mathrm{fs}^2/\mathrm{mm}$. This is shown in Fig. 4.5,

4.4.4 Spatially-Chirped Spectrum and Phase Retrieval

The principle behind prism (and grating) based stretchers and compressors is to first angularly disperse the component frequencies of

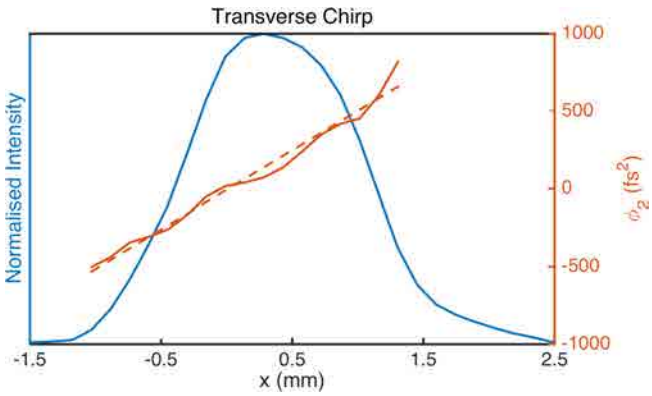

FIGURE 4.5: Transverse Chirp Measurment

a pulse, and then control their propagation path lengths before reversing the angular dispersion, to spatially recombine the frequencies, resulting in the desired compression or stretching of the pulse. We show the HAMSTER can be used to quantify the amount of GVD caused by the dispersive element. We perform this measurement by translating the prism 70 mm forward of the HAMSTER's object plane (M_1). The characterised pulse is similar to that measured with the prism at the object plane (M) however there is now an additional quadratic spectral phase of $1350\pm80\,\mathrm{fs}^2$, which corresponds to a length dependant dispersion of $19.3\pm1\,\mathrm{fs}^2/\mathrm{mm}$. The theoretically [38] expected dispersion is $19.1\pm0.04\,\mathrm{fs}^2/\mathrm{mm}$ in good agreement with what we measure.

The final measurement performed by the HAMSTER addresses a concern that has not been addressed in any of the other 3D characterisation techniques. A basic principal of a temporal characterisation device is that all the component frequencies need to be present in the part of the pulse being measured. An example of when this is not the case is spatial chirp. The retro reflector can be used to overcome this problem by selecting different points in the beam (x_n, y_n) to be temporally characterised. By using either

the spectrally resolved wavefronts constrained to a plane / a fixed wavelength, or the temporal characterisations constrained to one measurement point (x_n, y_n), an unambiguous reconstruction of the pulse can be achieved. We introduce spatial chirp by translating the prism 371 mm before the object plane (M_1) of the HAMSTER. Now as a consequence of propagation of the angularly dispersed pulse, the pulse becomes spatially chirped and not all frequencies have similar intensities at the centre of the beam. bFROG measurements are taken transversally in the beam at the points indicated by the red lines in the left plot of Fig. 4.6, combined with the usual WFS scan of the whole beam.

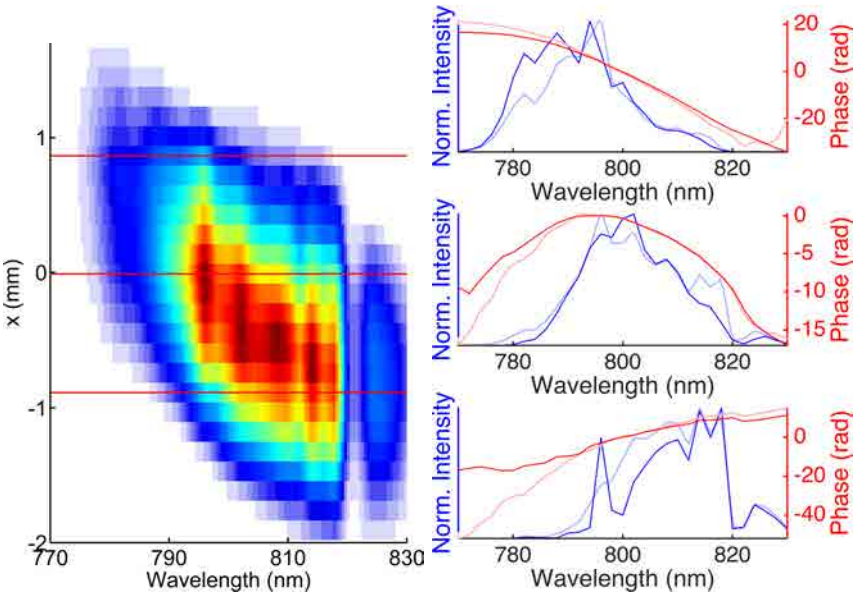

FIGURE 4.6: Left) Spatially-chirped pulse beam profile, shown as a function of a single spatial dimension (x) and wavelength. A bFROG measurement is taken at points in the beam, corresponding to the red lines. Right) The spectrum and phase of each point (top, middle and bottom respectively), with the bFROG reconstructed phase shown in red and the calculated phase shown in faint red, The bFROG reconstructed spectrum is shown in blue and the calculated spectrum is shown in faint blue.

It is clear that all the spectrum is not present in each individual bFROG measurement, however there is spectral overlap considering all three measurements. The redundancy ensures an overdetermined system which can then be processed using separate least-squares minimizations for the intensity and phase individually. The spectral intensity and phase reconstructed at each temporal characterization point is compared with that obtained directly from the bFROG measurements. The agreement between the calculated intensity and phase profiles and the bFROG retrieved intensity and phase profiles, shown in Fig. 4.6 b) is excellent, highlighting the ability of the HAMSTER device to accurately retrieve the electric field of a pulse in which not all the frequency components are present.

Chapter 5

Water-Window High Harmonic Beamline for Soft X-ray Spectroscopy

5.1 Introduction

In this chapter I will give a brief background to high-harmonic generation in the water window radiation range, with emphasis on the long wavelength driven, high gas pressure regime. This will be followed by a detailed description of our high harmonic beamline apparatus, in which water-window spanning radiation is now routinely generated. Investigation of the generation conditions are undertaken with regards to high gas pressure targets. In combination with energy calibration of the source, initial spectroscopic measurements are performed, culminating in the first near-edge x-ray absorption fine-structure (NEXAFS) spectroscopy measurement on a solid-state sample with such a source.

5.2 The Water Window Radiation Range

Up until recently, laser driven, bright high harmonic radiation and hence investigations into attosecond dynamics have been restricted to relatively low photon energies (below 150 eV) [39–43]. The next generation of experiments will need to access the absorption edges of elements more relevant to biological and organic systems. A particularly interesting range of radiation is defined from the carbon K absorption edge (284 eV) to the oxygen K absorption edge (543 eV). Biologically, this range is extremely important as it contains the absorption edges of the typical elements that are found in proteins as illustrated in Fig. 5.1 in which the absorption length is shown for different elements and compounds. It is clear to see from this figure that water is relatively transparent to this range of radiation. Experimentally, biological samples can typically be held in suspension in water, which would thus not interfere in any significant way with spectroscopic interrogation.

Organic semiconductors based around carbon, such as poly(3,4-ethylenedioxythiophene):poly(styrene sulfonate) (PEDOT:PSS) [44–48] are currently very important and relevant materials. From modern displays found in televisions and mobile telephones, to the more pertinent applications such as organic photovoltaics, their use and study is already vast but still growing rapidly.

Radiation in this range, especially radiation with the potential of being supplied in attosecond duration bursts has the potential to uncover the fundamental triggering events that lead to the reactions and behaviour that these systems currently exhibit. The understanding gained through these investigations could lead to drastic improvement in control and efficiency of these processes.

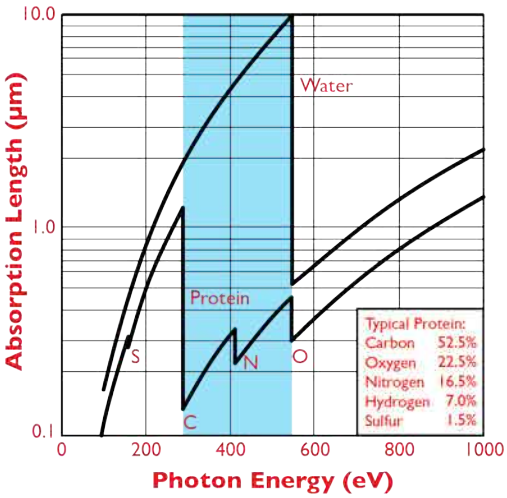

FIGURE 5.1: The water window radiation range (blue shaded area), containing the absorption edges of a typical protein [49]

5.3 High Harmonic Generation - The Long Wavelength, High Gas Pressure Regime

High harmonic generation in gas is an extremely non-linear process whereby the response of an atom (or cluster or molecule) to an intense laser electric field results in the emission of radiation having significantly lower wavelengths (or higher photon energies) than the driving radiation. The process has been most elegantly described by the now well-known three-step model [50] in which an atom is in the presence of an intense laser electric field. Around the peak of the electric field oscillation, the atomic potential is perturbed significantly enough to facilitate the tunnel ionisation of an electron into the continuum. The liberated electron is then accelerated away by the laser electric field. As the electric field oscillates past its peak, the electron is accelerated back towards the parent ion. The high kinetic energy electron has a probability of recombining with

its parent ion. If re-collision does occur, the atom's excess energy is shed via the emission of a high energy photon.

The highest energy achievable (the cut-off energy) through this process is described by the high harmonic cutoff law [51]:

$$E_{max} = I_P + 3.17U_P \tag{5.1}$$

Where I_P is the ionisation potential of the gas and the ponderomotive energy

$$U_P = \frac{e^2E^2}{4m\omega_0^2} \tag{5.2}$$

Where e is the electron charge, E is laser electric field amplitude, m is the electron mass and ω is the laser carrier frequency.

From this law, it is apparent that the two ways to get to higher photon energies are to increase laser intensity (linearly scaled) or to increase the laser carrier wavelength (quadratically scaled). On paper these two solutions are simple, but in reality both prove to be technically challenging. Increasing intensity could involve laser upgrades such as additional amplification stages, in combination with probable upgrade of expensive compressor optics to re-compress the pulses. On the other hand, scaling wavelength (ponderomotive scaling) either needs an entirely different laser to be bought or built, or energy sacrificial wavelength conversion stages need to be employed to get to longer wavelengths.

Unfortunately, the cut-off energy cannot be indefinitely extended through intensity scaling due to a) depletion of the HHG gas's ground state when gases with lower ionisation potentials are being used for HHG and b) the reduction in phase-matched generation

mediated by the excess free electrons. Intensity scaling has however resulted in non-phase matched water-window high harmonics [52].

Significantly more work has been undertaken by groups in the field to ponderomotively scale the HHG process to extend to higher photon energies [53–58]. More complicated theoretical studies [59] confirm the expected cut-off extension and also suggest a reduced intrinsic chirp resulting from the electron energy dependant recombination time of the returning electrons (This is discussed in detail in the next chapter). The first experimental results showed harmonic cut-offs extending beyond the carbon K-edge [57, 60]

An unfavourable consequence of driving the HHG process with long wavelength radiation is that the single atom response scales very poorly with driving wavelength: $\lambda^{-(5-6)}$[61], λ^{-9}[62]. This poor scaling can however be mitigated by high pressure gas phase-matching [56]. The combination of ponderomotive scaling, and high pressure gas phase-matching has led to the highest harmonic cut-off ($>$1 keV) to date [55].

Our approach to HHG builds upon the state of the art results, by combining: ponderomotive scaling, high gas pressure phase matching with CEP phase stable, few-cycle laser pulses.

5.4 The Water Window High Harmonic Beamline

Our high harmonic beamline can best be described by its five interconnected vacuum chambers. Common to each chamber is that while the chambers themselves are bolted to floor-mounted framework, the optical platforms inside each chamber are connected via

vacuum bellows to the optical table (which can be pneumatically floated). This decouples the optics in each chamber from the environment offering significant environmental vibrational isolation as well as substantial improvements in stability.

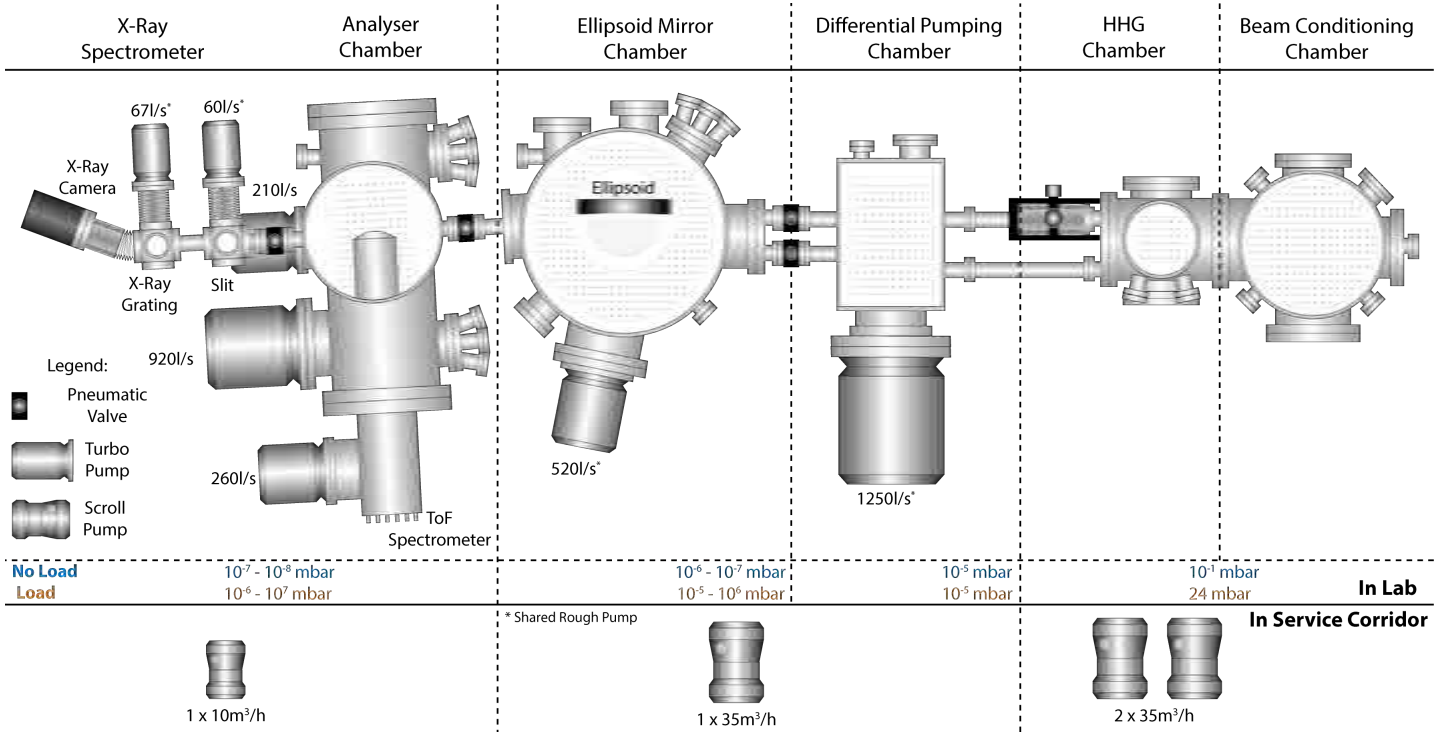

FIGURE 5.2: The high harmonic beamline schematically represented by the five vacuum chambers. Vacuum pump capacities are shown for all the turbo-molecular and scroll pumps, the latter kept outside the laboratory. Typical pressures are shown considering an unloaded system in blue and loaded in orange.

5.4.1 Beam Conditioning Chamber

This chamber contains the optics needed to condition the beam for high harmonic generation i.e. telescoping and focusing optics. Additional optics can be added in this chamber to prepare the beam line for any form of pump-probe type experiment.

5.4.2 High Harmonic Generation Chamber

This chamber is the heart of the HHG beamline containing the free-space HHG target in which water window harmonics are generated. The focusing optic is also located in this chamber mounted in a Smaract motorized tip/tilt mirror mount controllable from outside of the vacuum chamber allowing for fine alignment tuning of the generating beam. The HHG target is described in more detail in section 5.4.6. The target is mounted on a Smaract motorized goniometer also controllable from outside the vacuum chamber and having its slide radius centred on the gas/laser interaction region. The goniometer is then mounted on a cage, which can be externally translated in the following ways: 1) rotationally (parallel to the optical table) about the gas/laser interaction region and 2) linearly in all three spatial directions. This totals three linear axes and the two needed rotational axes permitting perfect co-alignment of the target aperture and the generating beam. The mounting geometry and translational capabilities are shown in Fig. 5.3 A small mirror fixed to an externally controllable motorized linear stage is installed just after the target allowing us to sample the beam after it has traversed the target or as an alignment tool when making more significant changes to the beam pointing in the previous chamber. The target is connected via tubing to a Swagelock vacuum feedthrough and out via a high pressure regulator to the various gas sources.

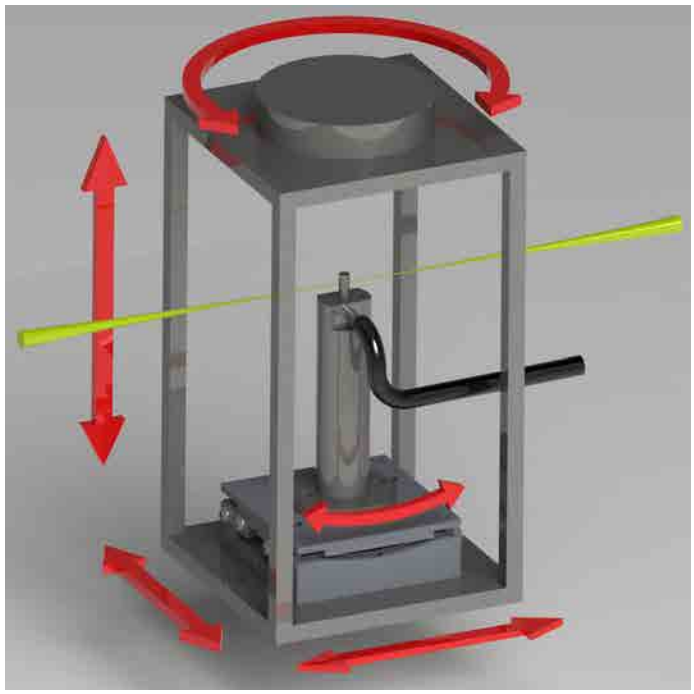

FIGURE 5.3: HHG target mounting and movement geometry, showing the three degrees of translational freedom and the two degrees of rotational freedom. Gas is introduced into the target via the black flexible tubing.

One of the keys to the brightness of the source is the ability to sustain high gas backing pressures in the HHG target. Two Edwards 35 m^3/h scroll vacuum pumps alone are used to maintain ambient pressures in the low tens of millibars under running conditions. This may seem like a poor vacuum for a HHG chamber however in the water window, the reabsorption of radiation is not as debilitating compared to sub 100 eV radiation. The second innovation in this chamber is the addition of a small diameter pumping aperture (1 mm) which extends as close to the HHG target as possible on one end and on the other end is connected via vacuum bellows to a two-axis linear positioner allowing alignment of the pumping aperture

while under vacuum.

This chamber has two parallel output CF40 flanges, one used by the HHG beam (referred to as the probe arm) and the second ready to be used for a pump/probe setup (referred to as the pump arm)

5.4.3 Differential Pumping Chamber

The next chamber's primary role is to assist the differential pumping configuration. We have achieved this by connecting the giant Pfeiffer 1250 l/s turbo pump directly to the chamber. This turbo pump enables pressures in the order of 10^{-5} mbar down from a few tens of millibars in the previous chamber. The pump arm connection is sealed with a 400 µm thick brewster-angled window, maintaining vacuum tightness through that arm.

In between this chamber and the next, pneumatically actuated vacuum valves are placed on each of the two arms.

5.4.4 Ellipsoid Mirror Chamber

The mirror chamber contains our ellipsoidal focusing mirror, which is a one of a kind taking more than a year to design and manufacture. The Zerodur substrate is 260 mm x 50 mm x 40 mm, resulting in a clear aperture of 201 mm x 8 mm and coated with 35 nm of platinum. It was initially mechanically polished and then ion beam "polished" to an atomically smooth surface finish having a measured surface roughness of less than 0.5 nm over the whole surface. The mirror relies on grazing incidence reflection to refocus the harmonics into the analyser with a 2× demagnification, resulting in a smaller beam and higher intensity on target. The very-high on-target flux of the

water-window harmonics is due both to the design and application of a high gas pressure HHG target, but also to the impeccable quality of the ellipsoidal mirror. Figure 5.4 shows the efficiency curves calculated as a function of left) surface roughness and right) incidence angle in which the blue curve represents our setup. Small deviation

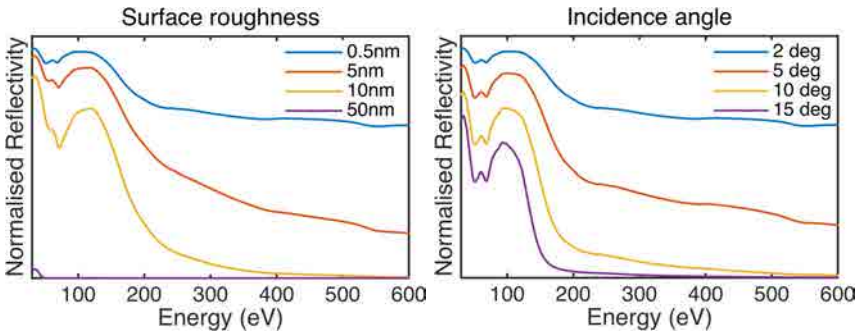

FIGURE 5.4: Ellipsoid efficiency, based on tabulated data [63] as a function of: Left) Platinum surface roughness for a 2 degree incidence angle. Right) Incidence angle for platinum with a surface roughness of 0.5 nm

from the 5 angstrom smoothness or 2 degree design angle can result in nearly no reflection in the water window range. The mirror is mounted to a motorised six-axis hexapod stage, which is computer controlled and allows any conceivable orientation of the mirror ensuring both perfect alignment of the optically complex mirror as well as the ability to steer the harmonic beam.

All HHG beamlines have some form of filter holder housing the filters used to filter out the remnant fundamental in the HHG beam. We use a motorised twin-wheel rotating filter holder, each wheel capable of housing 6 filters. The filter wheel is controlled externally and allows us a wide variety of filters as well as the ability to combine up to two filters at a time.

The chamber is vacuum pumped with a single 520 l/s turbo pump, sustaining pressures in the order of 10^{-7}mbar down from 10^{-5}mbar in the previous chamber

5.4.5 Analyser Chamber

The chamber is configured for three primary diagnostics, the third of which I have not made use of during my PhD and is hence excluded from the beamline schematic. A combined electron time of flight (ToF) / ion mass spectrometer (Stefan Kaesdorf - ETF15) and an electron spectrometer (SPECS - Phoibos 150) and an X-ray spectrograph. The ToF spectrometer and the electron spectrometer are located to ensure that they share an acceptance volume at the focus of the ellipsoidal mirror. The chamber is fitted with a three-axis CF-40 mounted positioner directly above the focal volume. An additional gas target can be fitted in this port allowing co-alignment of a gas jet, the X-ray radiation and the acceptance volume of the detectors. Radiation continues on to the X-ray spectrograph.

The chamber is vacuum pumped by 920 l/s, 260 l/s and 210 l/s turbo pumps, the ToF spectrometer has an additional 260 l/s sustaining pressures in the order of 10^{-9}mbar down from 10^{-7}mbar in the previous chamber. The spectrograph has two additional 60 l/s and 67 l/s turbo pumps maintaining a pressure of around 10^{-7}mbar.

The X-ray spectrograph consists of a motorised slit which is placed 465 mm after the focus of the ellipsoidal mirror. The aberration corrected concave grating (Hitachi 001-0450) then images the slit to the X-ray CCD camera. The camera rotates around the axis of the grating allowing coverage of a broad spectral range from below 100 eV to above 600 eV. Spectrographic resolution can be optimised by closing the slit to its minimum aperture (17 μm) however due to

the propagation distance from the centre of the ToF chamber (The ellipsodal mirror focus) the x-ray beam has diverged by the time it gets to the slit plane, so resolution is gained at the expense of photon flux.

5.4.6 HHG Target

The HHG target consists of a stainless steel tube which is sealed on one side, while the gas is introduced via the other side. The tube has an outer diameter of 1.5 mm and an inner diameter of 0.5 mm. A 300 µm hole is then cross drilled through the tube. This cross drilled hole acts as the interaction region between the gas and the laser and the small aperture helps to facilitate the high backing pressures needed for efficient generation of long wavelength driven HHG.

The high gas pressure phase matching regime can be defined by multi-atmosphere gas pressures being applied to the HHG targets. More often than not pressure is measured via a gauge some distance away from the target itself i.e. in the tubing supplying the gas to the target. Direct measurement of the pressure exiting the target inside the vacuum chamber is not a trivial measurement to perform - usually via Schlieren techniques or some form of interferometry in which a reference beam is interfered with a beam that travels through the region of gas to be measured. The results of such a measurement yields the pressure-length product. If the spatial resolution of the interferometric measurement is sufficient, a two dimensional pressure map could be inferred, however this can be insufficient especially when trying to map areas as small as the 300 µm exit hole of our target. It is also not necessarily sensible to assume cylindrical symmetry in the gas output profile, which could reduce the accuracy

of the pressure map inferred from the 2D pressure profile measured with the interferometer.

Besides measurement, the next best option is to perform a computational fluid dynamics (CFD) based simulation of the gas flow from the HHG target. ANSYS Fluent CFD offers an advanced suite of tools to model and simulate the complex, turbulent and supersonic gas flow experienced in our target. A full three-dimensional simulation is performed by first replicating the target geometry in Solidworks CAD, whereafter a triangular based mesh is applied to the model with an element size of 0.01 mm. The gas is modelled as an ideal gas. The turbulence model resulting in the best match with the experimental results is the K epsilon model. A photograph of the gas target can be seen in the top of Fig. 5.5. The visible plumes are present due to radiative transitions in neon, where their intensity at a point can allude to the density in that region. The modulated brightness and discrete boundaries along the plume are a result of characteristic "shock diamonds" or "Mach disks" [64–66] associated with supersonic flow, in which sudden changes in density result in shock wave formation. The remaining plots in Fig. 5.5 show the velocity, density, pressure and temperature of the gas respectively. The density profile shows an excellent match to the photograph in which the complex dynamics resulting in shock formation can be seen. The excellent match of this simulation allows us to confidently extract pressure and temperature profiles which will become important for the analysis of data in the next chapter. The influence of these shock-wave structures on HHG and propagation of high harmonics has not been looked into and may prove to be interesting in future investigations.

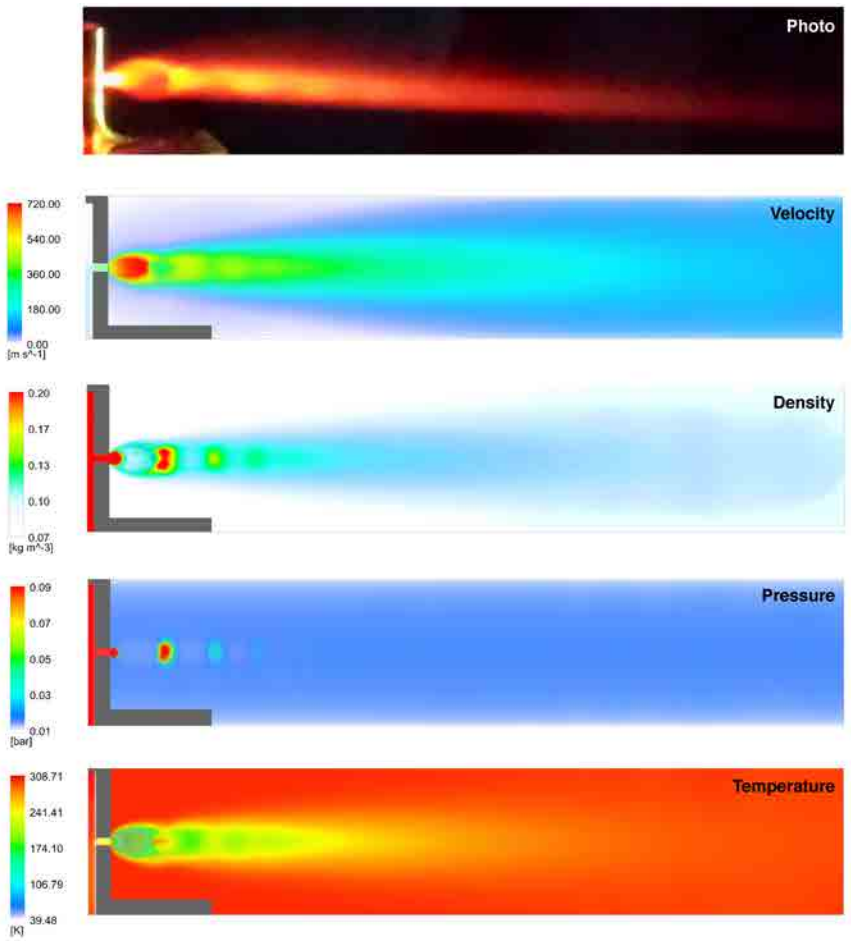

FIGURE 5.5: Top) This is a photograph taken of the HHG target backed with 3 bar of neon. The laser propagation is from left to right. Below) FEA gas pressure simulations - from top to bottom: Velocity, Density, Pressure and Temperature

5.5 Water Window High Harmonics

We use three noble gases to generate high harmonics: argon, neon and helium. Table 5.1 lists the most relevant parameters regarding these gases. Optimal backing pressure corresponds to the balance

between the highest yield and the highest cut-off. Alignment integration time gives a practical guide to the difference in flux detected by the three different gases. The table is assembled based on data obtained by performing gas pressure scans using the three different gases (see Figs. 5.7). To negate the highly CEP dependant spectral features, CEP is randomised during these measurement.

Gas	**Optimal Backing Pressure (bar)**	**Cut-off (eV)**	**Alignment Integration Time(s)**
Argon	1.2	160	0.01
Neon	3.5	370	1
Helium	7(14*)	500	5

TABLE 5.1: HHG Gases. *Our differential pumping setup can sustain continual backing pressure of 7 bar, however we have briefly doubled to 14 bar to identify the system limitations

5.5.1 Spectral Calibration

Two dimensional data is recorded on the x-ray CCD camera on a detector size of 2048 pixels × 512 pixels. The imaging spectrometer projects spatial information in the vertical axis (512 pixels) and spectrally disperses the beam in the horizontal axis (2048 pixels). Spectral calibration of the x-ray spectrometer from pixels to energy (eV) is performed by introducing thin filters with known absorption edges into the beam. A combination of filters is used to accurately retrieve the absorption response to the specific filter. Carbon has a K-edge at 284 eV whereas titanium has an L-edge at 454 eV offering two well separated calibration points in the water window. Aluminium exhibits good transmission covering the entire water window range.

Harmonic radiation was generated using helium, ensuring spectral continuum spanning the entire water window. Three filter combinations are used to perform the calibration: 1×100 nm of aluminium, 1×100 nm of aluminium + 1×200 nm of carbon and 1×100 nm of aluminium + 1×200 nm of titanium, where a 2 minute integration is taken for each permutation. The response of the carbon and titanium filters are then calculated by performing the following calculation: (C+Al)/Al and (Ti+Al)/Al. The two filter responses are shown in Fig. 5.6 where the excellent signal to noise ratio at the edge very clearly allows identification of the absorption edge with a very short integration time. This basic calibration step alluded to the great photon flux of our source and steered us towards performing a more significant spectroscopic investigation.

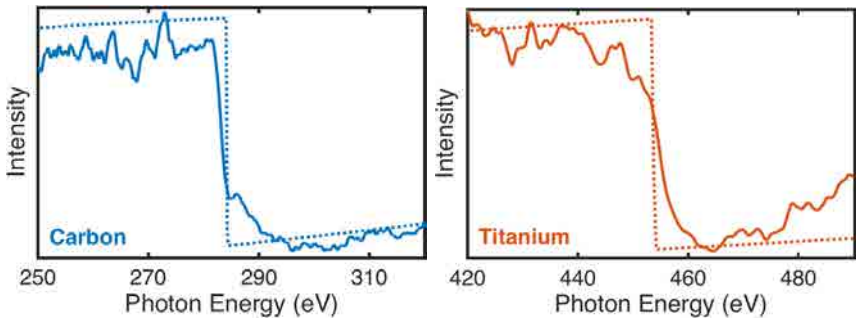

FIGURE 5.6: Spectral calibration showing the filter response with the solid curves and the theoretical absorption edge [63] with the dashed curved for: left) carbon and right) Titanium

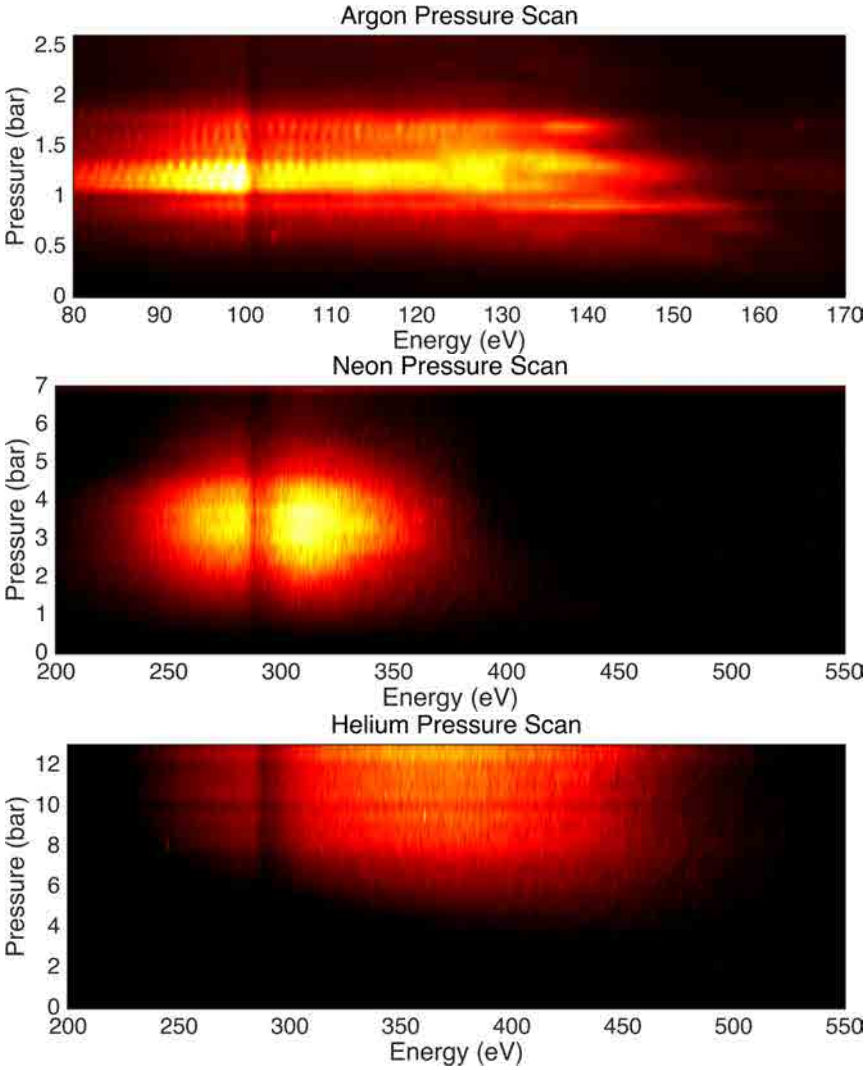

FIGURE 5.7: Top) Argon: The dip around 100 eV corresponds to the absorption of the silicon L-edge (the camera CCD is silicon based). Middle) Neon: The highest harmonic yield coincides with the highest cutoff at a backing pressure of 3.5 bar. Bottom) Helium. Carbon contamination in the beamline is visible through the absorption of photons at 284 eV in the neon and helium scans

5.6 Near Edge X-ray Absorption Fine Structure Spectroscopy

5.6.1 Polyimide

With the now routine generation of water-window HHG, a proof of principle experiment was planned to investigate the real-life usability, flux and resolution of the source. We decided to spectroscopically interrogate a sample that consisted of hopefully measurable and distinguishable bond structure.

Polyimide consists of a polymer of imide monomers, Kapton a common polyimide, is used extensively in the electronics industry owing to its high heat resistance and its high electric insulation properties. Polyimides have also been extensively studied with synchrotron or x-ray laser radiation, which would allow some comparison with published results. We already had a free standing 200 nm foil in the lab, so decided to use this foil in the first spectrographic test of the system. The foil was attached to a filter holder that could be positioned by a vacuum-manipulator, allowing insertion and removal of the filter from the beam while still under vacuum.

To maximise the resolution of the measurement while maintaining the high flux through to the CCD, we temporarily modified the beamline by removing the analyser chamber and placing the slightly modified spectrograph in its place (slit removed). The object plane of the concave grating was now close to the focal plane of the ellipsoidal mirror. In this configuration, with the slit no longer used, there is no loss of flux from a divergent beam clipping the slit. The focal spot size of the X-ray beam is comparable to the minimum slit aperture ensuring optimal resolution.

Water-window radiation spanning the range of interest for the polyimide foil was generated using 3.5 bar of neon. A single 5 minute 2D spectrum was recorded with the foil in place whereafter the measurement was repeated with the foil out of the beam - This process is needed to post-process spectra to extract the response of the polyimide foil (spectrum with foil / spectrum without foil = foil response). The 2D spectra and the integrated spectra are shown in Fig. 5.8, with polyimide in the beam on the left and out of the beam on the right. The spectral dip centred around 284 eV in the reference spectrum is attributed to hydro-carbon contamination in the detection system which inevitably finds its way into all experimental setups. Already without any processing of the data, fine

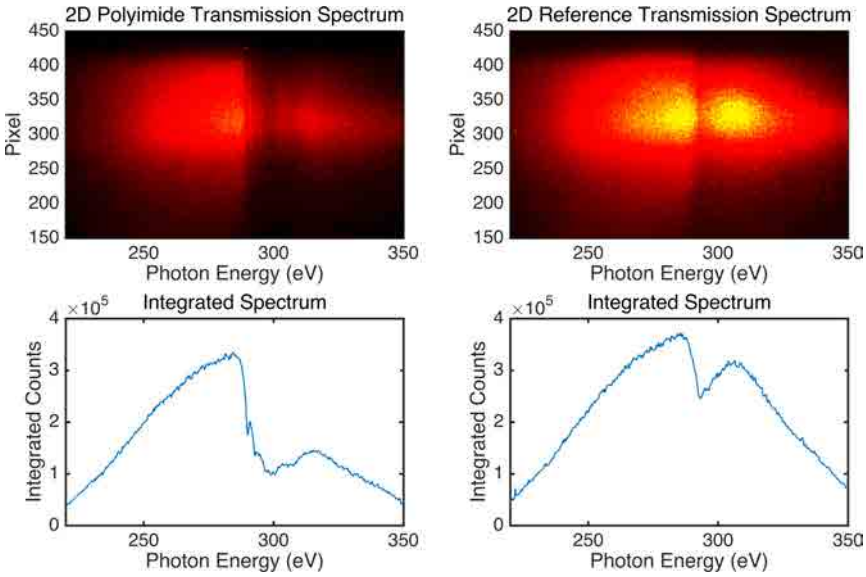

FIGURE 5.8: Polyimide Raw Data

structure can be seen in both the 2D and the integrated polyimide transmission spectra at the carbon K-edge. First, the optical density (OD) of the polyimide is calculated, whereafter a more in depth analysis into the contributions to the OD from the constituent bonds

Energy (eV)	Orbital/Orbitals
284.9	$\pi * C = C$(Aromatic)
286.9 and 287.4	$\pi * C = C$(Phenolic) and $\sigma * C - H$
288.9	$\sigma * C = O$
291.7	$\sigma * C - C$
294.3 to 295.8	$\sigma * C - O$ and $\sigma * C - C$
298.0 to 303.2	$\sigma * C - C$ and $\sigma * C = C$

TABLE 5.2: NEXAFS peaks - energies and corresponding orbital assignments from reference [68]

is performed using the Demeter software package, which is a "comprehensive system for processing and analyzing X-ray Absorption Spectroscopy data" [67]. Table 5.2 shows the known [68] energies and orbital assignments for polyimide, measured in that case with non-coherent X-ray radiation generated in a laser-plasma source.

5.6.2 Analysis

The analysis of NEXAFS data revolves around using various functions to fit the experimentally recorded absorption spectral peaks. Typically the peaks are fitted by Lorentzian functions, however instrument response can transform them depending on their width, in which case Gaussian functions can be fitted. A step function is also always included in the fit and is needed owing to the ionisation from the core level at which the absorption edge features are prominent. The Demeter software enables the manual selection and fitting of these curves and plotting a residual. This kind of analysis has already been performed [68], offering us a very robust way to verify our results. Normally when performing this analysis, one would manually select the energy of a peak by simply looking for the peak in the experimental data. Once identified, the Lorentzian/-Gaussian function is fitted to the peak. This process is repeated for

each peak until the sum of the fitted peaks and the step function match the experimental data with a minimum residual. In this case we could use the peak centres from the literature, adjusting the peak shape, intensity and width to match our experimental data. Using this method I was able to build a very accurate fit to the data. This is illustrated in Fig. 5.9 where the measured data is represented by the blue crosses. The various colour peaks correspond to the bonds in the polyimide. A fit sum shown in black shows incredibly good agreement with the experimental data, also illustrated with the small residual at the bottom of the plot.

Although this result was to some extent an initial proof-of-principle experiment to characterise the ability of the x-ray source, it also stands as a milestone of the first NEXAFS spectroscopy experiment performed with a water-window high harmonic source in which the constituent bonds of a solid state organic sample can be clearly identified. This is illustrated in Fig. 5.10 where the molecular structure of polyimide is shown along with the colour-coded arrows corresponding to the NEXAFS retrieved data.

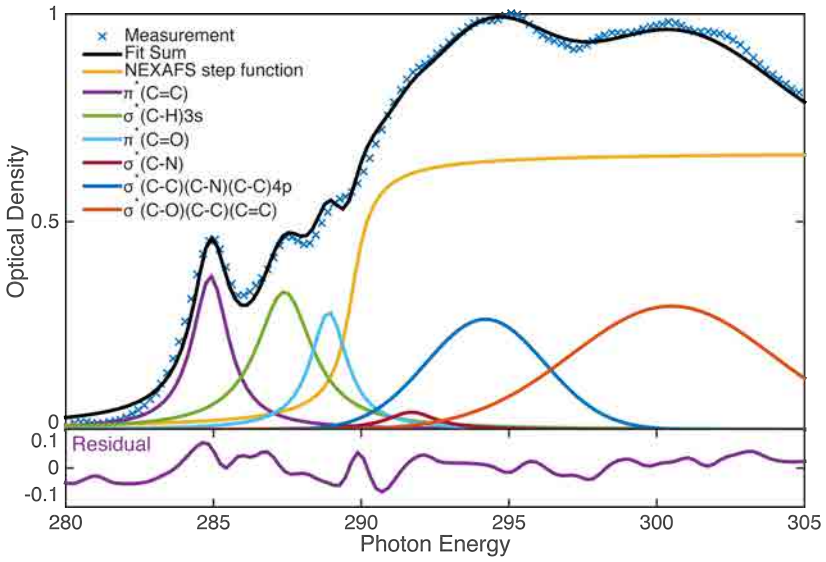

FIGURE 5.9: NEXAFS measurement of a 200-nm free-standing polyimide foil (blue crosses). A peak fit with known transitions (blue) from [68] agrees very well (black curve) with the measurement.

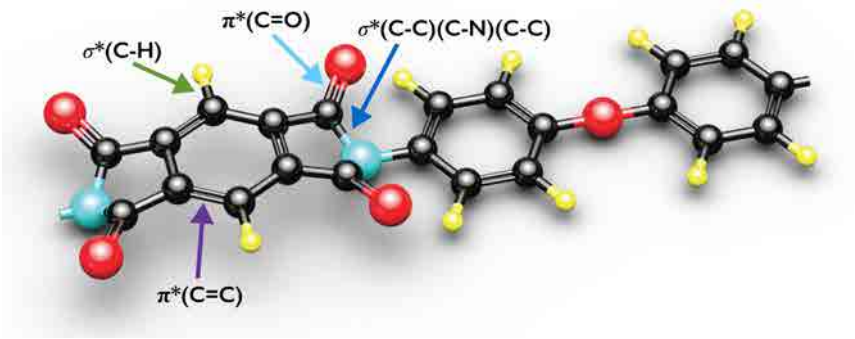

FIGURE 5.10: The polyimide molecule, with the benzene rings shown in black, hydrogen atoms in yellow, oxygen atoms in red and the nitrogen atoms in blue. Four of the bonds colour-coded from Fig. 5.9 are shown

5.7 Design of an X-ray Spectrograph

As discussed in section 5.4.5, spectral resolution is improved by closing the slit, however this reduces the photon flux reaching the CCD. The focal spot size of the x-ray beam is dependant on the generation conditions, particularly the choice of HHG gas. Knife edge based measurements have shown that the spot sizes are in the range of the minimum slit width. With this in mind I investigated the possibility of an extremely compact spectrograph design that could place the grating such that it images the ellipsoidal mirror focus directly to the CCD camera without the need of a slit. This configuration could provide both the highest flux in combination with the highest resolution.

Using the design specifications of the grating, I designed and built a new spectrograph using Solidworks 3D CAD. The design included a custom vacuum manipulator that would allow for in-vacuum manipulation of the grating in the two required axes i.e. grating rotation and translation in and out of the x-ray beam. A new ultra-high vacuum (UHV) rotation stage was also designed and fabricated "in-house" which allows for smooth, grease-free ball-bearing based rotation, while still keeping the grating perfectly vertical.

The spectrograph consist of a primary chamber in which the grating is mounted to a UHV manual rotation stage atop a manual linear stage. An industrial bearing connected rotating arm holds the X-ray CCD camera, allowing the camera to rotate about the vertical centre of the grating. This degree of freedom allows for a camera position capable of selection of multiple radiation ranges, for example 100 eV to 200 eV for argon generated harmonics at one position and 200 eV to >600 eV for neon generated harmonics in a second position. The camera is connected to the primary chamber via a vacuum-bellow

as well as being fixed to the rotating arm in a sliding track, allowing for the initial precise alignment of the camera-to-grating distance to ensure that the camera is placed in the image plane of the concave grating.

The vacuum manipulator controlling the grating position and angle consists of three micro vacuum-bellows welded to a CF40 vacuum flange. An M6 bolt feeds through the vacuum flange under atmospheric pressure to control the extension of the micro vacuum-bellows. In the primary chamber, the lower-most micro-vacuum-bellow is in direct contact with the linear translation stage, whose internal spring loading ensures back force against the vacuum-bellow. The upper-two micro-vacuum-bellows then contact a flat plate on the rotation stage allowing alternate extension and contraction of each to control the rotation of the grating. The first water window spectra recorded with the new spectrometer can be seen in Fig. 5.11.

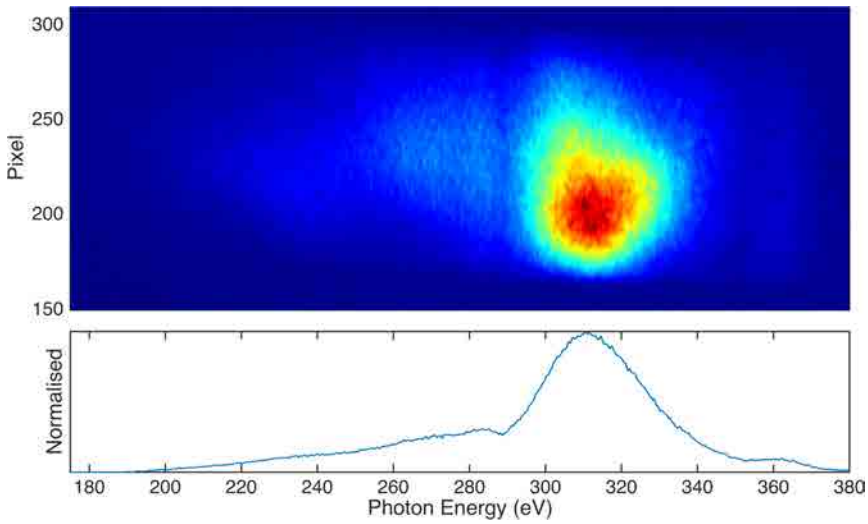

FIGURE 5.11: Carbon K-edge spectrum generated in neon

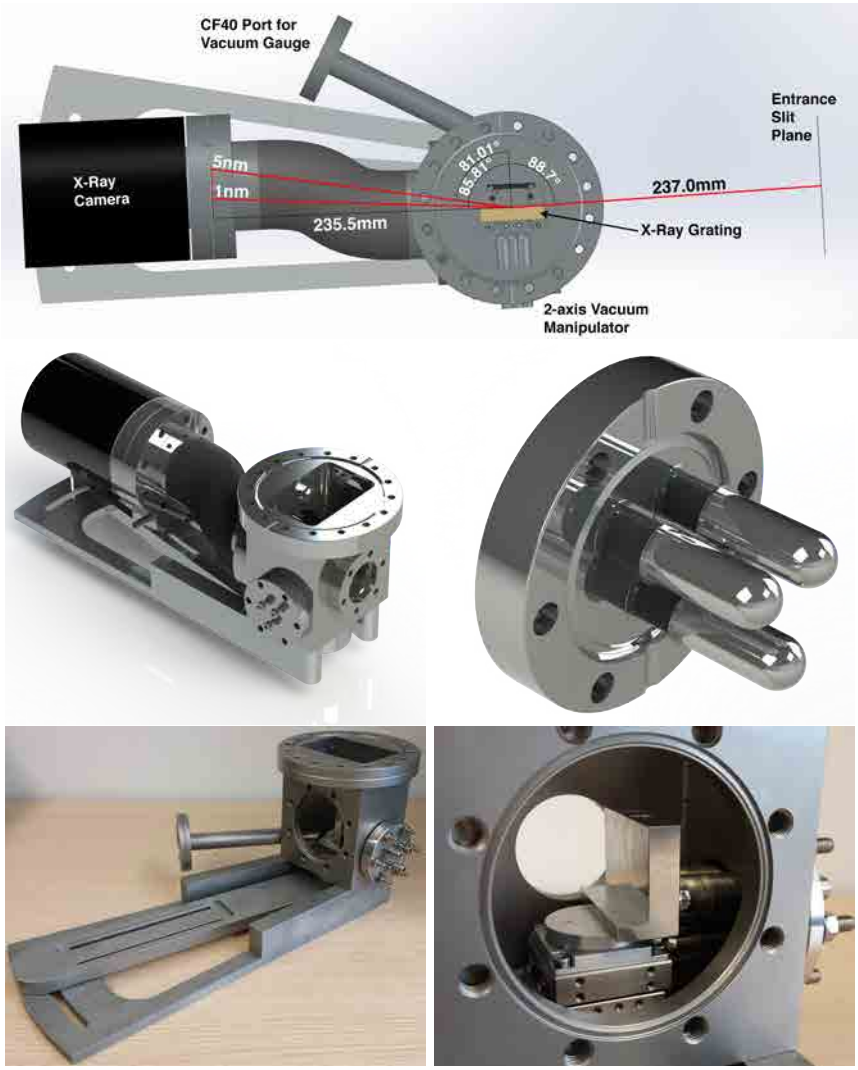

FIGURE 5.12: Top) Geometric design parameters for the x-ray spectrograph. Middle row left) Photo-rendered CAD model of the spectrograph. Middle row right) Photo-rendered CAD model of the micro-bellow vacuum manipulator. Bottom row) Photographs of the manufactured spectrograph

Chapter 6

Attosecond Streaking in the Water-Window

6.1 Introduction

In this chapter I will give a brief theoretical description of the attosecond streaking technique. This will be followed by a description of our attosecond streaking setup. Next I will present our attosecond streaking results, followed by a discussion on the findings.

6.2 Attosecond Streaking

The idea of the attosecond streak camera was first formalised in 2002 [69] soon after which a method of retrieving the phase from streaked spectra was formulated [70]. The basic principle of the technique considers the photo-ionisation of atoms by a high energy

electric field $\mathbf{E}_{XUV}(t)$, in the presence of the time delayed electric field $\mathbf{E}_{LASER}(t)$, for convenience defined by its vector potential: $\mathbf{E}_{LASER}(t) = -\partial\mathbf{A}/\partial t$. From reference [70], the amplitude of populating the continuum state $|\mathbf{v}\rangle$ (the transition amplitude) with momentum $\mathbf{v}$ is given by

$$a(\mathbf{v},\tau) = -i\int_{-\infty}^{+\infty} dt e^{i\phi(t)}\,\mathbf{d}_{\mathbf{p}(t)}\cdot\mathbf{E}_{XUV}(t-\tau)e^{i(W+I_p)t} \tag{6.1}$$

Where $\mathbf{d}_\mathbf{p}$ is the dipole transition matrix element from the ground state to the continuum state $|\mathbf{p}\rangle$, $\mathbf{p}(t) = \mathbf{v} + \mathbf{A}(t)$ is the instantaneous momentum of the free electron in the laser field, $W = \mathbf{v}^2/2$ is the final kinetic energy of the electron and I_p is the atomic ionisation potential.

The main effect of $\mathbf{E}_{LASER}(t)$ is to induce a temporal phase shift $\phi(t)$ on the electron wave packet $\mathbf{d}_\mathbf{p}\cdot\mathbf{E}_{XUV}(t)$ generated.

$$\phi(t) = -\int_t^{+\infty} dt'[\mathbf{v}\cdot\mathbf{A}(t') + \mathbf{A}^2(t')/2] \tag{6.2}$$

Mairesse et al. realised that the photo-electron spectra $|a(\mathbf{v},\tau)|^2$ from equation (6.1) was similar to that of the signal recorded in a FROG trace:

$$S(\omega,\tau) = \left|\int_{-\infty}^{+\infty} dt G(t)E(t-\tau)e^{i\omega t}\right|^2 \tag{6.3}$$

A similar iterative algorithm such as the Principal Component Generalized Projections Algorithm (PCGPA) could therefore be used to extract the phase of both the extreme ultra violet (XUV) pulse and the streaking pulse, where the FROG gate is a pure phase gate $G(t) = e^{i\phi(t)}$. The method was named frequency resolved optical gating for complete reconstruction of attosecond bursts (FROGCRAB).

The FROGCRAB technique was first used to retrieve the phase and amplitude of few cycle isolated attosecond pulses, resulting in a 130 as pulse duration [71]. The technique has become the de-facto technique for measuring isolated attosecond pulses ex-situ. The technique has also been used to characterise delays in photoemission [72] and tunnelling delays from different states on solids [73].

6.2.1 Attochirp

The final step of the three-step model described in chapter 5 considers the recombination of the high energy electron and its parent ion, resulting in the emission of a high energy photon. HHG is obviously not a single atom process, but instead the consequence of an ensemble of emitters interacting with a broadband laser pulse spectrum. The recombination process is however not instantaneous for all electron energies, which results in a recombination time that is dependant on the electron energy. The broader the energy bandwidth, the longer the time it takes for the recombination to complete. Although this recombination time occurs during a fraction of the driving laser pulse cycle, the bandwidth of the emitted photon spectrum can in principle support pulse durations much lower than the described fraction of the driving laser pulse cycle. The emitted photon pulse thus has a maximum pulse duration stretching from the moment the first electron recombines to the moment the last electron recombines. A spectrum that is composed of temporally separated components is the definition of spectral chirp and in the context of attosecond pulses generated via HHG this is referred to as attochirp.

The intrinsic attochirp scales inversely with the wavelength [74] and intensity [75] of the HHG driving laser. The λ^{-1} scaling is shown in

Fig. 6.1 for intensities typical to our setup, contrasting our wavelength to that of Ti:Sa. It has been shown that taking into account this scaling, an optimal bandwidth exists to generate the shortest IAP without subsequent pulse compression albeit these pulses would not be transform limited. For the short trajectory electron recombination the attochirp is positive (lower energies recombine first) a suitable negative GDD compressor will be required to compress the IAPs. A suitable compressor could also compress over a larger bandwidth than the optimal bandwidth identified above.

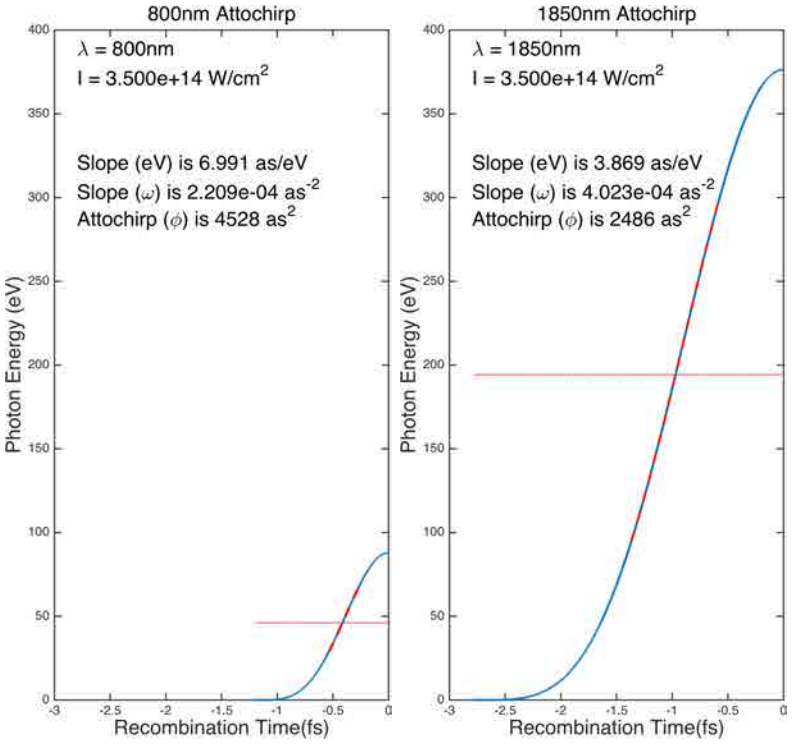

FIGURE 6.1: left) 800nm right)1850nm

Typically at sub-150 eV photon energies, thin metallic films have been used as the negative GDD compressor. The concept of using

these filters was described [76] in 2004 and luckily these filters are normally already in place as they are used to prevent illumination of the sensitive X-ray CCD by high flux fundamental radiation. Depending on the photon energies, the transparency and GVD of the filters varies heavily and these characteristics may or may not permit the use of these filters as compressors.

Owing to the reduction in attochirp from the long wavelength driven source. Atomic gas can also be considered as the negative GDD compressor. A theoretical study in 2012 [77] suggested that an 83 as pulse generated by 1.6 μm laser pulses could be compressed to 38 as (FTL 34 as) using a 10mm gas cell, containing 160 mbar of xenon.

6.3 Water-window Attosecond Streaking Setup

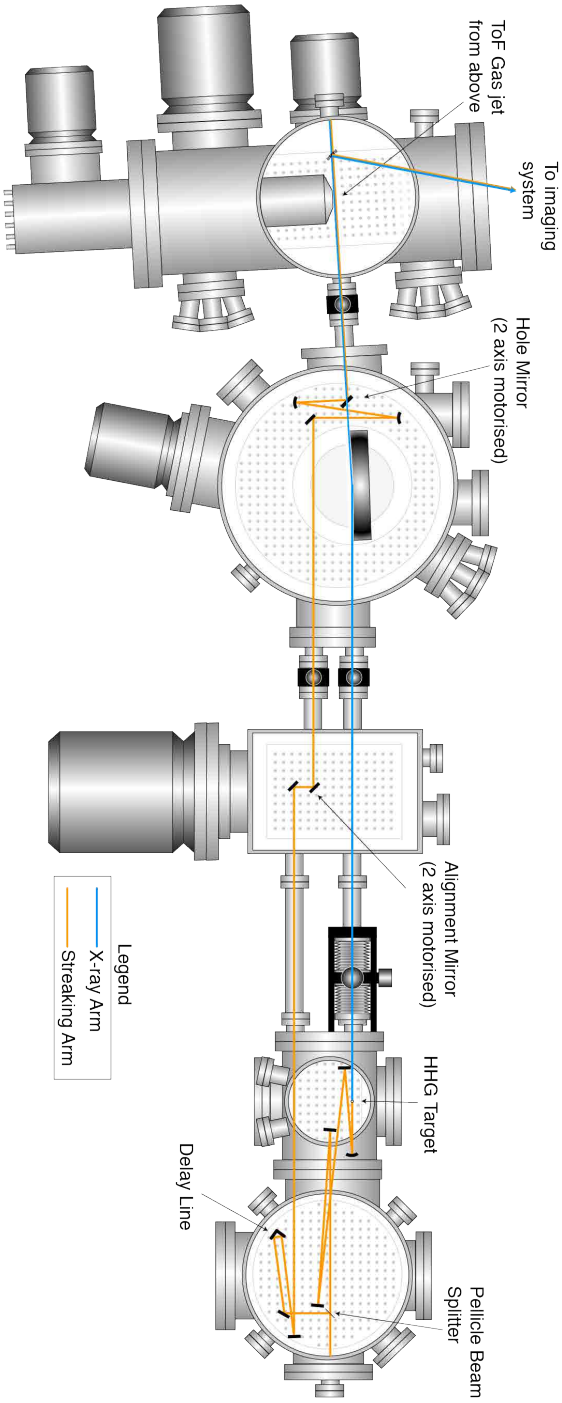

FIGURE 6.2: Water-window Attosecond Streaking Setup

The water-window beamline was designed from the beginning with pump-probe type experiments in mind, so no major modifications were needed to the apparatus. Common to all extreme ultra violet (XUV)/x-ray streaking setups is an interferometer comprised of a streaking arm and the XUV arm. In this setup, shown in Fig. 6.2, an ultra-thin pellicle beam-splitter is used to split the 1.85 µm pulses into a ratio of 70% for HHG (transmitted), leaving 30% for the streaking pulse (reflected). The 2 µm thickness of the pellicle ensures no measurable chirp is added to the HHG pulses. The high harmonic target is as described in the chapter 5, charged with a backing pressure of 3.5 bar. The streaking arm of the interferometer contains the delay line, consisting of a Smaract nanometre precision linear translation stage, which has a zero travel reference. An additional motorised linear stage with a 1 mm aperture pinhole allows for the centre of the streaking beam to be sampled (this will be discussed in more detail later).

In the differential pumping chamber, the XUV beam passes unfettered, whereas the streaking beam is aligned through to the next chamber via a New Focus motorized mirror mount, permitting in-vacuum alignment of the streaking beam.

In the ellipsoidal mirror chamber, the XUV and streaking beam are recombined using a 45° gold mirror, with a 2 mm hole drilled at 45°, again allowing unimpeded focusing via the ellipsoidal mirror of the XUV beam through the hole. The streaking beam is first expanded and then focused using two reflective spherical mirrors whose focal lengths and positions are carefully chosen and painstakingly tested to ensure that the foci of the XUV and streaking beam are co-planar in the acceptance volume of the ToF and at the same time ensure that the streaking beam is as large as possible on the hole mirror to minimise the loss of intensity caused by the hole in the mirror.

The hole mirror is mounted in a Smaract two-axis motorised mirror mount to allow for steering of the streaking beam.

At water-window photon energies, the ionisation cross-sections of the typical noble gases is not as favourable compared to those of sub-150 eV photon energies, so maximising ionisation yield is a key component on the ability of this set-up to capture electron spectra in reasonable time frames. Increasing the number density of the gas to be ionised is one of the ways to mitigate the low yields, so taking this into consideration, I designed and fabricated a stepped diameter gas target needle consisting of various lengths and diameter tubes, downsizing in a step-wise fashion from a Swagelock vacuum feed-through to the eventual needle tip, which has an internal diameter of 160 µm. This small diameter final needle tip is chosen to maximise the number density of gas molecules at the exit of the needle by enabling relatively high backing pressures in a vacuum chamber which is maintained at pressures around 10^{-9} mbar. The target is shown in Fig. 6.3 illustrating the final three steps of the needle from thinnest (right) to thickest (left) - 1 mm of ID 160 µm, 3 mm of ID 310 µm and 25 mm of ID 800 µm.

In the analyser chamber an externally controlled linear positioner allows insertion of a gold mirror (pick-off mirror) into the beam path 100 mm behind the ToF interaction region. The mirror deflects the beam through a vacuum viewport into a home built imaging system which is configured to image both the hole mirror and the ToF needle target tip simply by shifting the imaging camera.

The alignment and balancing of such an interferometer all of which is concealed in small and inaccessible vacuum chambers, proves incredibly challenging. Measuring each arm to an accuracy of less than a centimetre is practically difficult and time consuming. I decided to try an optical measurement technique, making use of a commercially

available "laser ruler" available at any good hardware store. These laser rulers use a red laser diode and an adjacently placed integrated photo detector. They work on the principle of measuring a phase shift between the transmitted and then received laser beam and offer accuracy of under 3 mm. Use of this laser ruler substantially cut alignment down to a couple of hours, the first time the optics had been placed, and only a few minutes when subsequent changes were made to the interferometer.

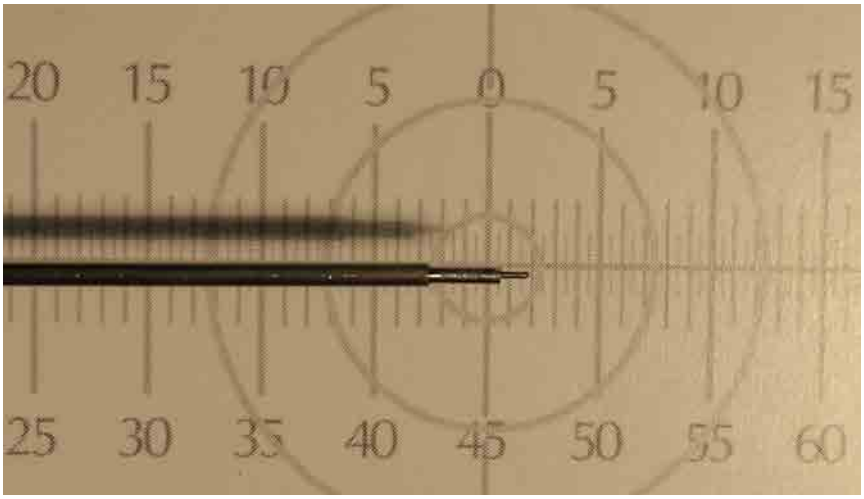

FIGURE 6.3: Needle target used in the time of flight spectrometer

6.3.1 Alignment procedure

The first step in alignment of a streaking measurement is to optimise the HHG process. By using the filter wheel to rotate a 200 nm titanium filter into the XUV beam path to block the fundamental radiation and monitoring the photon spectrum, it is possible to adjust what I call the base parameters, such as gas pressure fine tuning, target position fine tuning (three axes) and HHG iris aperture to maximise the yield and harmonic cut-off. After this, a value

of CEP can be selected which produces a clear spectral continuum over the majority of the spectrum. This spectrum is most likely to be a consequence of a single half-cycle dominating the HHG process.

The streaking beam then needs to be optimally aligned, centred on the hole mirror aperture. The imaging system is enabled by introducing the pick-off mirror into the beam path with the manual linear positioner. The WinCamD-FIR is placed in the hole mirror imaging plane and the beam is steered onto it using the New Focus motorised mirror.

The next step is to overlap the two arms of the interferometer in space and time, both of which are conveniently revealed with the same diagnostic. The WinCamD-FIR is now placed in the ToF needle-tip imaging plane and the titanium filter is removed from the beam path. By removing the 200 nm titanium filter, the camera can now detect the focal spots of both the streaking beam (referred to as streaking-IR) and the fundamental radiation left in the XUV beam (referred to as XUV-IR). The streaking-IR beam focus can then be steered onto the XUV-IR focal spot using the Smaract motorised mirror mount. The intensity of the streaking IR beam far exceeds that of the XUV-IR due to clipping on the differential pumping aperture in the generation chamber. To simplify the spatio-temporal overlap diagnostic, the motorised 1 mm aperture can first be centred on the streaking beam to limit its intensity. Now by scanning the delay stage while monitoring the beam profile comprised of the overlapped streaking-IR and XUV-IR, the temporal overlap presents itself as very obvious spherical interference between the two beams. This beam profiler technique to find the spatio-temporal overlap is only obvious over a very small delay range around zero delay, so an additional flip-mounted mirror was used to send the optically spatially overlaped beams to a spectrometer sensitive to radiation

around 1.85 µm. The spectral fringes that appear as a consequence of temporal overlap of the two pulses is more apparent over a much larger delay range - finely modulated far from zero delay, approaching coarsely modulated at the zero delay. A combination of these two diagnostics ensures spatio-temporal overlap of the two IR beams.

6.3.2 XUV-IR / Streaking-IR Cross-correlation

Before attempting a streaking measurement, a cross-correlation measurement can be performed using the XUV-IR and streaking-IR. This cross-correlation uses the ToF spectrometer to collect electrons ionised by the two IR beams as a function of the delay between them and can be used to accurately identify the "zero delay" point between the two pulses and to choose a suitable delay range. The cross-correlation also serves as an indication of the stability of the interferometer.

The intensity of the streaking beam (with or without the 1 mm aperture in place) is insufficient to ionise a gas target, such as krypton (despite its low ionisation potential) and even less so the XUV-IR. The cross correlation is therefore performed by translating the ToF stainless steel target needle tip fractionally into the overlapped beams and attenuating the streaking-IR with the 1 mm aperture. Electrons from the stainless steel tip can now be detected in the ToF spectrometer and this configuration can be used for the cross-correlation. A typical cross-correlation trace is shown in Fig. 6.4. The time delay between two maxima are ≈ 6 fs which is expected as the cycle duration for pulses with a spectrum centred at 1.85 µm is 6.2 fs (for pulses with a spectrum centred at 1.80 µm it is 6.0 fs). The pulse duration of under 12 fs obtained from the FROG measurement in section 2.6.1 is already roughly verified with this cross-correlation

trace having less than 4 peak modulations. The cross-correlation can now be used to define the delay range over which to attempt a streaking measurement.

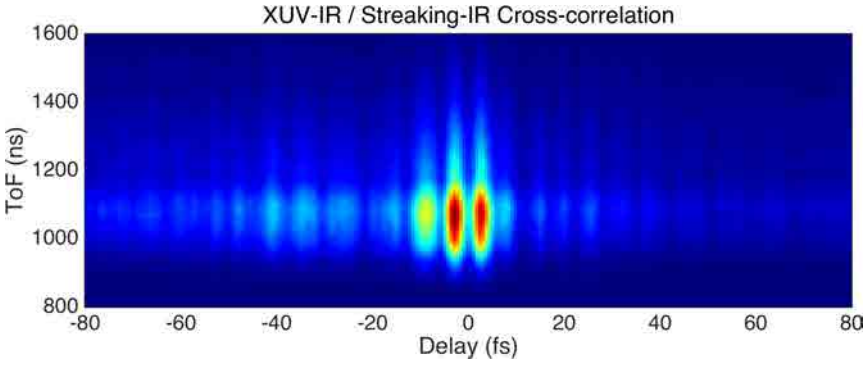

FIGURE 6.4: Cross-correlation of the streaking IR and the XUV-IR

Unfortunately the spatio-temporal co-alignment of the streaking-IR and the XUV-IR does not guarantee the best co-alignment of the streaking-IR and the XUV. This is a consequence of the fact that the XUV may not be at the centre of the XUV-IR (the XUV-IR is apertured by the hole mirror, whereas the XUV is going through the hole, but not necessarily centred on it). Fine tuning of this alignment needs to be undertaken once a streaking signal is detected. This can be done by doing a grid based scan of the pointing of the streaking beam, using the imaging system to mark the grid.

6.3.3 Streaking Target Gas

Krypton gas is selected for streaking for two main reasons. It has a relatively high and flat photoionisation cross-section (see Fig. 6.5)

in this energy range permitting realistic integration times for measurement. More importantly though is that having energies far exceeding 100 eV enables ionisation from core levels. The $3d$ (94 eV) shell of krypton has an ionisation cross section approximately an order of magnitude higher than the next two shells $4s$ (27.5 eV), $4p$ (14.1 eV). This high contrast is desired in this case as our bandwidth (150 eV to 350 eV foot to foot) can access electrons in all three of the listed shells.

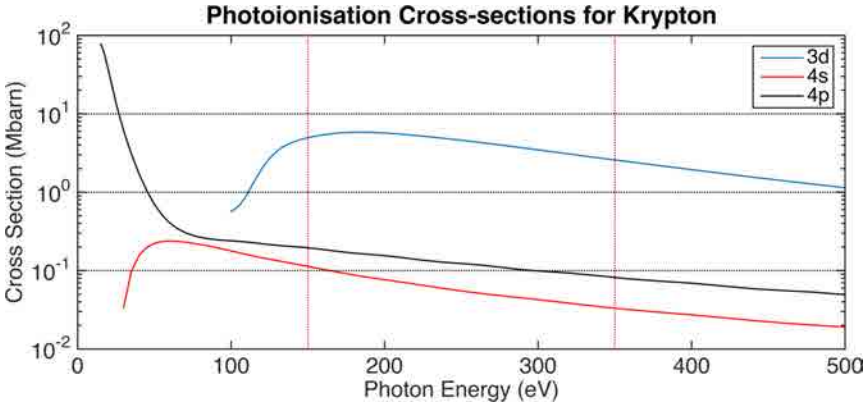

FIGURE 6.5: Photoionisation cross-sections for 3d, 4s and 4p shells. The dotted red lines enclose the range of photon energies relevant to this streaking measurement

6.4 Results

Once the streaking signal is maximised, the setup is ready to record a streaking spectrogram. To maximise counts we did not re-introduce a thin metallic filter to the XUV arm. To verify that this was not problematic, I recorded static time-of-flight spectra with the filter in and out, revealing identical flight times and only differing in count rate. A delay range of 36 fs is selected with a step size of 0.6 fs. Signal

to noise ratio appeared acceptable with 10 minute integration times at each delay step.

The raw streaking trace is shown in Fig. 6.6. The most striking features of this trace are the extremely broad bandwidth centred around 150 eV (implying 250 eV photon energy after ionisation from the 3d shell). The trace also gives an indication of a true isolated attosecond pulse, with no visible evidence of any significant pre- or post- pulse.

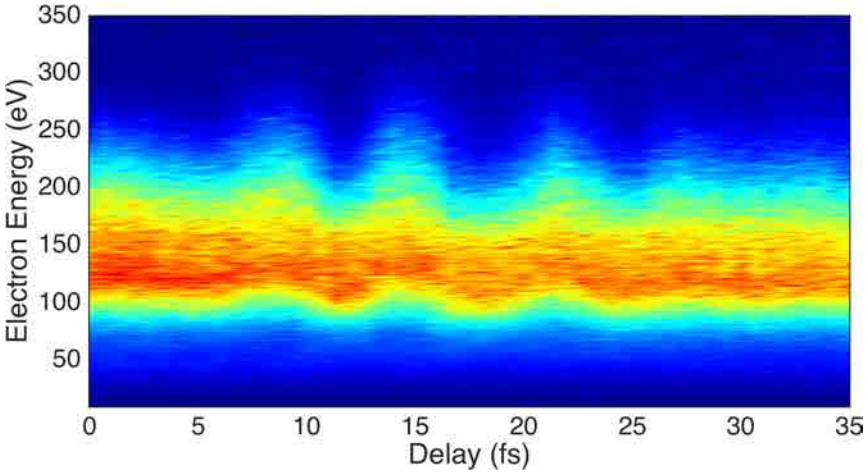

FIGURE 6.6: Raw streaking trace

The FROGCRAB technique ultimately relies upon a phase retrieval algorithm, such as the PCGPA to reconstruct the phase of the field being measured. For robust PCGPA reconstruction a sampling criterion needs to be satisfied and that is:

$$\delta\tau\Delta\omega = 2\pi \tag{6.4}$$

Where $\delta\tau$ is the delay step and $\Delta\omega$ is the total frequency range.

The bandwidth over which the streaked signal exists is around 200 eV and to satisfy the sampling conditions of the Fourier transform in the PCGPA algorithm, ensuring satisfactory resolution in the temporal domain, the experimental data needs to be interpolated onto a significantly broader frequency range (-300 eV to 700 eV). Satisfying criterion 6.4 then requires interpolation of the delay axis too, to a grid size of 8096 points. An interpolated experimental grid size of 8096 x 8096 fed into the FROGCRAB algorithm would take a few months to hopefully converge. It is valid though to perform the computation on one or two of the cycles instead, which allows for a smaller grid size to be used while still satisfying the requirements of equation 6.4. We repeat the FROGCRAB analysis on two single oscillations, as well as two double oscillations (see Fig. 6.7), all of which allow for a smaller grid size and achievable algorithm processing times. The retrieved pulse durations and phases are listed in table 6.1 and the measured vs. reconstructed traces are shown in Fig. 6.7.

Delay Region (fs)	**Pulse Duration (as)**	**GDD (as^2)**
16 to 28	22.8	116.4
22 to 34	25.2	234.1
15 to 21	22.4	-56.5
28 to 34	21.8	218.6

TABLE 6.1: FROGCRAB results for two oscillation retrieval (top two) and single oscillations (bottom two)

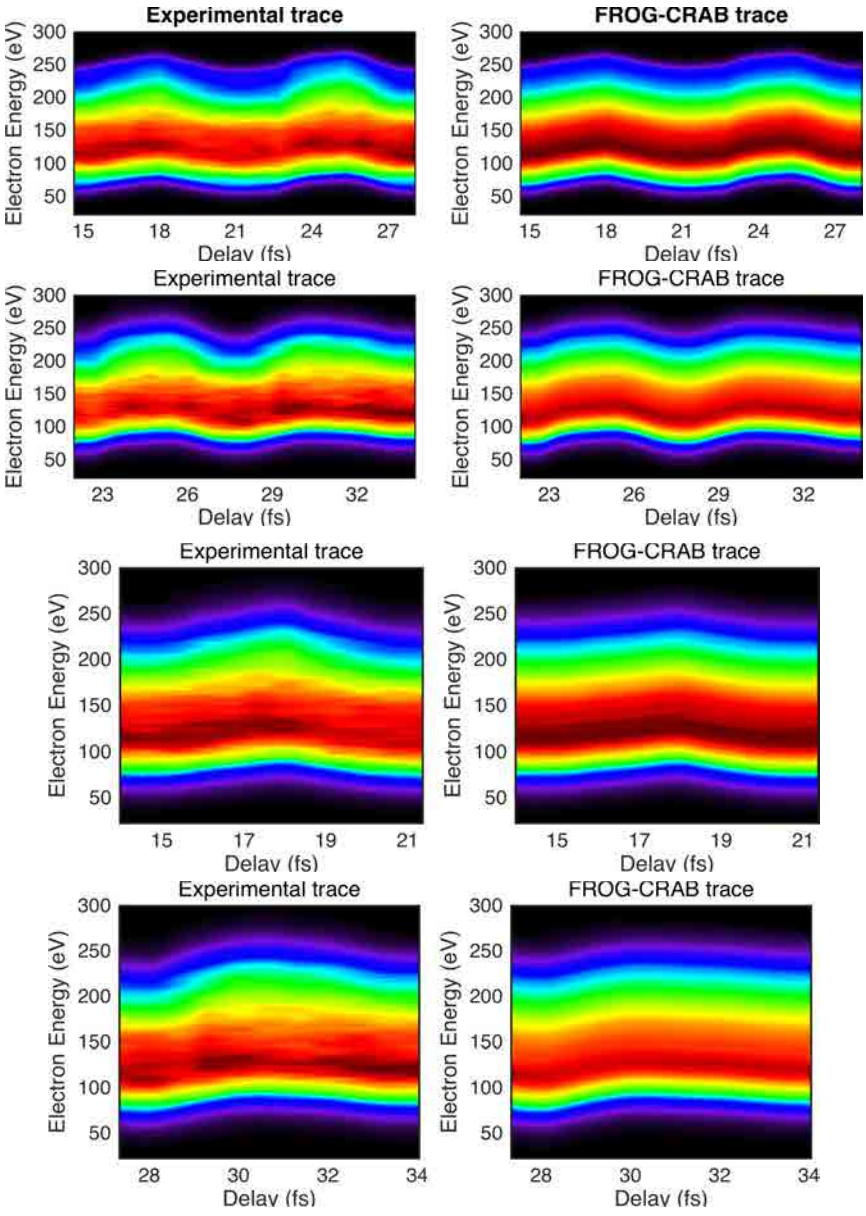

FIGURE 6.7: 2 Cycles (Top two rows), 1 Cycle (bottom two rows). Left) Experimental trace, top Right) Retrieved trace

6.5 Analysis

6.5.1 Attochirp

The results of the experiment were indeed at first quite a surprise! Self-compression of an isolated attosecond pulse in the water window, below the atomic unit of time seemed too good to be true. Quantifying the expected attochirp is not a trivial task however a first estimation is to use the classical picture of attochirp. Newtonian equations of motion can be used to quantify the flight time and hence recombination time of the electrons liberated during the ionisation. From Fig. 6.1 it is clear that we are looking for attochirp compensation in the order of -2500 as^2. The hunt was on to find the compression mechanism that resulted in this record pulse generation.

Unique to our HHG setup is the combination of an effusive gas target with multi-atmosphere gas pressures. The gas pressures typically used in these targets up until now have been sub 100 mbar where both dispersion and absorption of the XUV through any remnant gas was negligible. In our high-pressure regime, these cannot be ignored and have the potential to be the source of attochirp compensation. The trick is how to measure or ascertain the on-axis gas pressure that is potentially compressing the pulse. As described in the previous chapter, CFD based simulations have been used to obtain this information. Associated with the rapid expansion of the gas is a significant drop in temperature of the gas. In order to evaluate the GDD of the gas we need to know the refractive index which is both temperature and pressure dependant. The on-axis pressure and temperature profiles are shown in Fig. 6.8. The refractive index of neon is calculated from tabulated data [63] and then adjusted for the temperature and pressure [78].

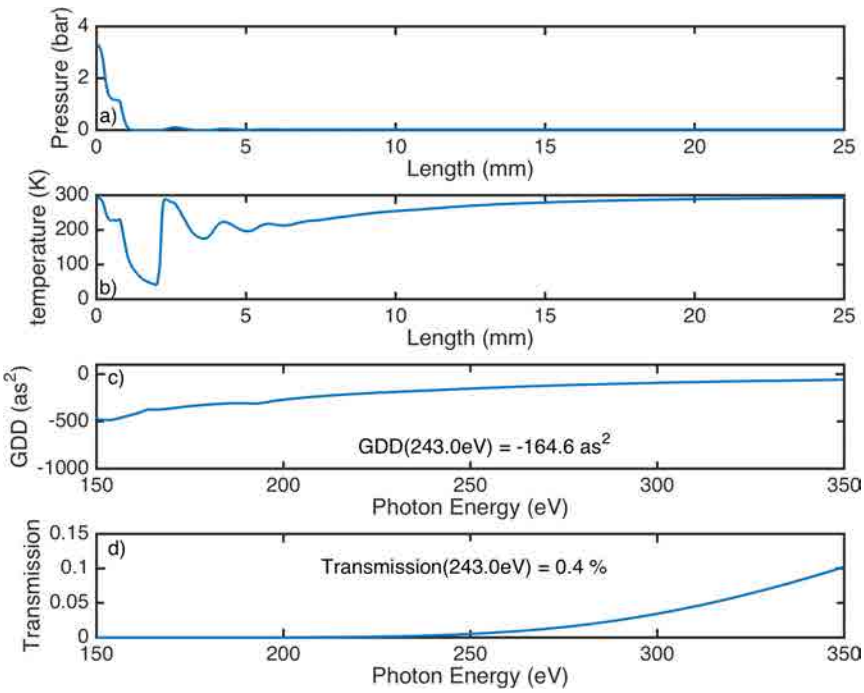

FIGURE 6.8: a) CFD based on-axis pressure profile (first 25 mm shown only). b) CFD based on-axis temperature profile (first 25 mm shown only). c) On-axis GDD of remnant neon. d) On-axis transmission of remnant neon

The conclusion from this simulation shows that for the expected on-axis gas pressure, there is more than an order of magnitude too little chirp compensation. The transmission of the x-rays through this remnant gas is also heavily limited by absorption. By simulating higher remnant pressures to investigate if the remnant gas is the source of chirp compensation it is apparent that x-ray reabsorption may be a limiting factor. The remnant gas is most likely not a viable source of chirp compression.

A contribution to the GVD is also expected from the ionised neon, however at the pressures and ionisation levels expected in our experimental conditions, the plasma GVD contribution is negligible

(Appendix section A.6.2).

A stark difference to the streaking based experiments is both the extreme bandwidth as well as the extreme photon energy at which our spectrogram is centred. Taking these into account I have investigated the validity of the method under these extreme and new conditions. The streaked excursion is dependant on the intensity of the streaking pulses. A simple code written in MatLab by a previous PhD student was used to simulate a streaked spectrogram as a function of different streaking pulse intensities. The results shown in Fig. 6.9 quite conclusively suggest that we are below a threshold at which the phase is encoded in the streaked spectrogram. Top left

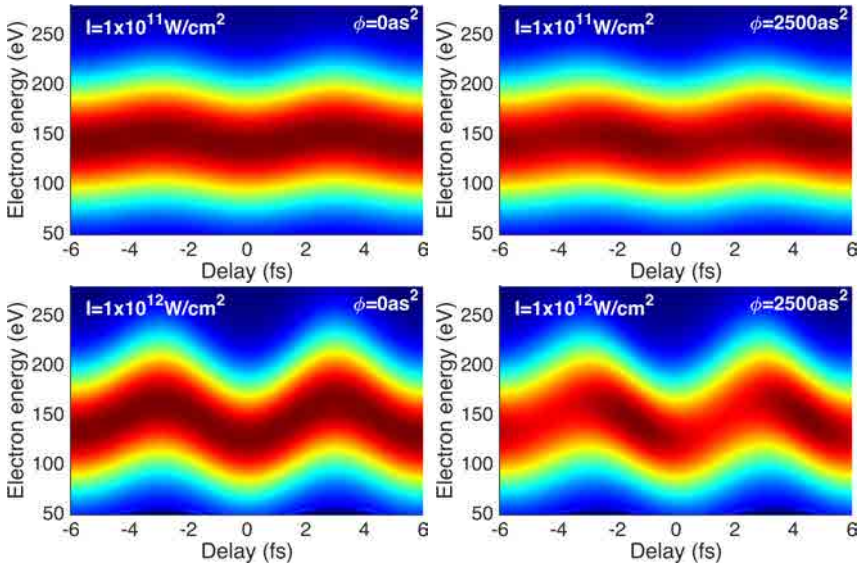

FIGURE 6.9: Simulated streaking trace over 2 cycles. Top two figures show a weak streaking field combined with significant attochirp, resulting in very similar streaking traces. For an order of magnitude higher streaking field and the same magnitude of attochirp, the traces are clearly different, suggesting that a threshold intensity is required to resolve attochirp in a streaking trace

in Fig. 6.9 shows the expected streaked spectrogram for no chirp

added to the pulse (with a transform limit of 19 as), whereas the adjacent plot shows for the same intensity but for an attosecond pulse chirped by 2500 as^2 resulting in a 407 as pulse duration. These two spectra seem very similar visually, the latter not obviously showing the characteristic asymmetrical intensity distribution typical of a chirped attosecond pulse spectrogram. The lower two plots in 6.9 mimic the upper two however with an order of magnitude higher intensity. Compounding this effect of not easily seeing asymmetry with a weak streaking field and having a relatively low streaking field intensity, it seems that the chirp-free appearance of our pulses may more likely be an artefact of measurement. To evaluate this further I have performed further simulations by generating streaking spectrograms with a fixed bandwidth, streaked by a pulse similar to our experimental pulse and have varied the amount of chirp for three different values (1250as^2, 2500as^2 and 5000as^2). I then performed a Poissonian statistical analysis of part of the streaking spectrogram that is not streaked to evaluate around what value of chirp is the asymmetry statistically relevant. Figure 6.10 shows the results of this simulation. For values of chirp below 2500as^2 the asymmetrical lineouts (blue and yellow curves) fall within the Poissonian variance bars of the non-streaked part of the spectrogram. The result adds strength to the hypothesis that taking into account a relatively low signal to noise ratio of an experimental trace, even a significant amount of chirp may be statistically invisible to a reconstruction algorithm.

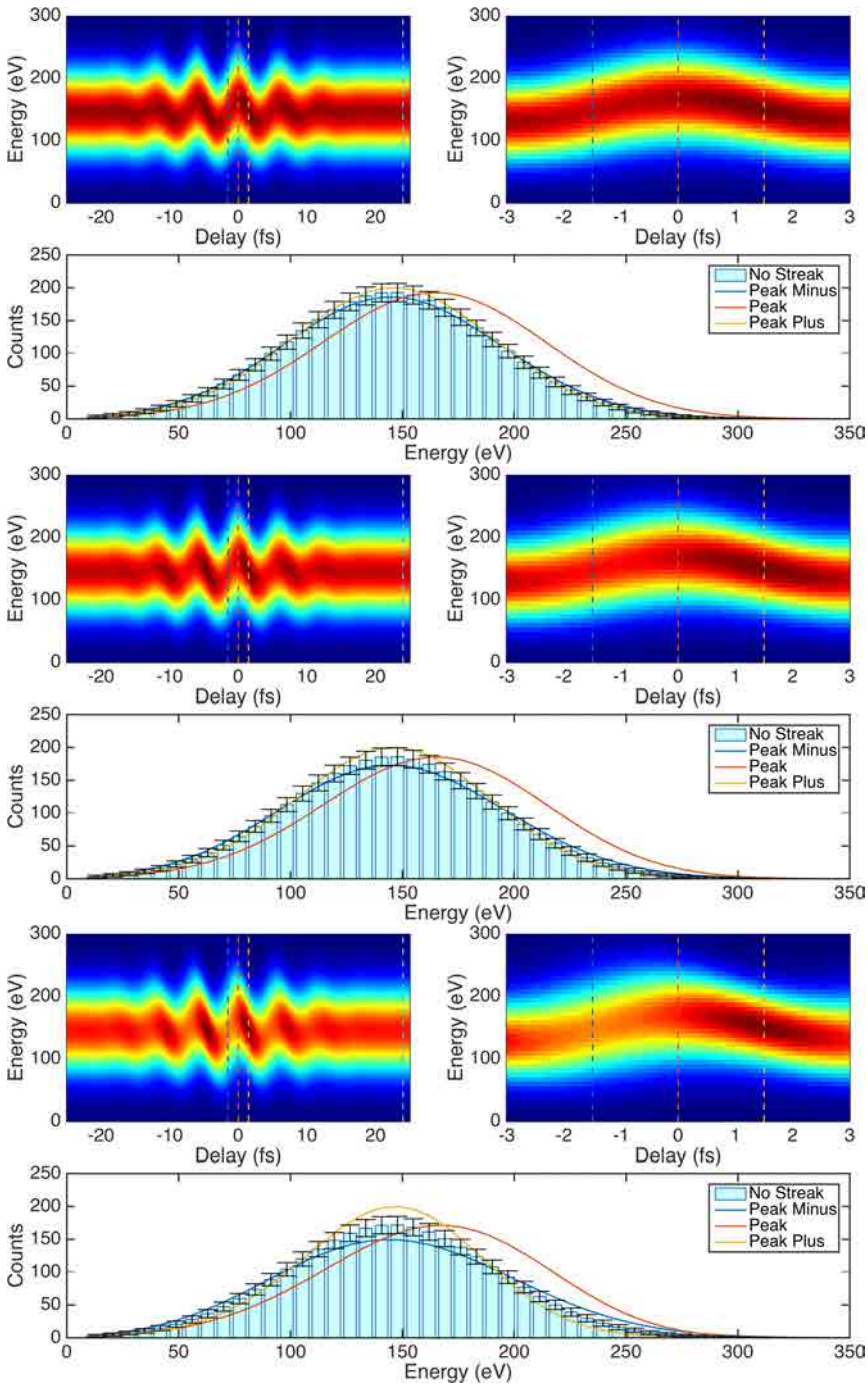

FIGURE 6.10: Statistical analysis of the resulting streaking spectrogram as a function of attochirp

A final simulation is performed to highlight the significance of our streaking data compared to what has already been achieved with narrower bandwidth spectra. Given the relatively low signal to noise ratio of our streaking signal, it is pertinent to investigate theoretically the limitations of the retrieval technique to reliably retrieve such broad bandwidth streaking spectrograms. To investigate this I used Matlab to generate streaking spectrograms with various bandwidths and chirps and then processed them with a FROGCRAB algorithm as well as the Least-Squares Generalized Projections Algorithm (LSGPA) [79] as a comparison to evaluate at what spectral bandwidth does reliable reconstruction break down. Table 6.2 shows the results of this study with the full retrieval data available in appendix A.7. The LSGPA algorithm appears better at reconstructing the pulses more accurately, however given 100 eV of bandwidth and a lower streaking pulse intensity of $1 \times 10^{11} \mathrm{W/cm^2}$, both algorithms are incapable of reconstructing the pulse. These simulations add weight to the assumption that at streaking field intensities that are too low, reconstruction of a pulse will not be possible using the FROGCRAB algorithm.

To conclude these simulations and the information mined from them, a further experiment is planned in which we will increase the streaking intensity with the use of a different optical setup for the streaking beam.

Simulated				FROGCRAB		LSGPA		Retrieval
Bandwidth (eV)	Phase (as^2)	Duration (as)	Intensity (W/cm^2)	Phase (as^2)	Duration (as)	Phase (as^2)	Duration (as)	
20	10000	318	1×10^{12}	7205	235	10267	317	Yes
40	10000	606	1×10^{12}	8315	503	11170	626	Yes
60	2500	230	1×10^{12}	2066	190	2498	232	Yes
100	2500	380	1×10^{12}	2104	321	2539	393	Yes
100	2500	380	1×10^{11}	6970	794	635	37	No

TABLE 6.2: Bandwidth scan - Streaking simulations

Chapter 7

Summary, Conclusion and Outlook

7.1 Summary

7.1.1 Chapter 2 - Titanium Sapphire Seeded, 1.85 μm Few Cycle, CEP Stable, Laser Pulses

Despite Ti:Sa laser technology being relatively mature, pushing the boundaries of ultrafast physics requires a Ti:Sa laser system that at the start of my PhD, simply did not yet exist: a high average power, high repetition rate amplifier capable of producing both spatially and temporally high quality laser pulses. Through extensive modelling, design and fabrication we were able to understand and implement the critical requirements, resulting in near perfect spatial beam quality, coupled with temporally clean laser pulses having remarkable shot to shot stability. The re-design of the laser system and the careful control of the environmental conditions also reduced

the daily start-up time from a couple of hours to a few tens of minutes.

A subsequent wavelength conversion stage, pulse compression scheme and CEP stability system have been added and fine tuned to convert a now relatively widespread ultrafast laser system into a light source with a truly unique parameter set described in table 7.1:

Laser Source Parameter	**Value**
Central Wavelength	1850 nm
Pulse Duration	12 fs
Repetition Rate	1 kHz
Pulse Energy	500 μJ
Peak Power	42 GW
Pulse Stability	1 % (peak to peak) over 1 hour
CEP Jitter	<100 mrad (72 hours)

TABLE 7.1: Long-wavelength, CEP-stable few-cycle laser source parameters

7.1.2 Chapter 3 - Pulse Characterisation of Few-Cycle Pulses using an Acousto-optic Programmable Dispersive Filter

Few-cycle laser pulses have enabled a plethora of ground breaking experiments. The generation and characterisation of these pulses has now become fairly routine in many laboratories.

In this experiment, hollow-core fibre pulse compression has been employed to spectrally broaden the output of a Ti:Sa amplifier, generating a spectrum broad enough to support a 7 fs laser pulse. Chirped dielectric mirrors have then been used to compensate for the chirp of the broadened hollow-core fibre spectrum, resulting in a sufficiently short duration pulse.

The Dazzler AOPDF has also had a significant impact on the field of ultrafast physics for its ability to behave as a programmable amplitude and phase filter, which has an ultra-simple in-line alignment. Owing to the Dazzler's ability to generate time delayed pulse replicas, it can be used to replace the traditional Michelson's interferometer required for virtually all pulse characterisation techniques. The only significant drawback of this system is that the Dazzler itself is highly dispersive, and this dispersion places limits on the bandwidth that can be pulse shaped into delayed replicas. The device described in this chapter overcomes this drawback by introducing a pre-compensation scheme to compensate for some of the second and third order dispersion of the AOPDF crystal. The inclusion of an FTSI phase comparison interferometer has resulted in a fully calibrated pulse characterisation device capable of accurately retrieving the amplitude and phase of an ultra-broadband laser pulse with a central wavelength around 800 nm and a bandwidth of more than 200 nm (measured foot to foot). A pulse duration of 9.4 fs has been retrieved using the device, which is thus far the shortest pulse duration ever retrieved with a pulse shaper based technique.

7.1.3 Chapter 4 - Three Dimensional Pulse Characterisation of Ti:Sa Laser Pulses - The HAMSTER Technique

The two most common pulse characterisation techniques: FROG and SPIDER are usually performed either on a small spatially selected part of the beam (the center) with the assumption that the phase does not differ drastically across the beam. Alternatively the whole beam is aligned into the device which then averages the phase over the whole beam. In most cases these assumptions and averaging are acceptable i.e. the output of a well aligned compressor in an

amplifier. However when the need does arise to quantify a spatio-temporal coupling such as a pulse front tilt these techniques fall short of providing this information

A technique to obtain this information involves recording a) the spatial phase of the whole beam in a device such as a Hartmann-Shack wavefront sensor at quasi-monochromatic wavelengths covering the spectrum of the broad band laser pulse and b) recording the spectral phase of a single point in the beam with a conventional characterisation device such as FROG or SPIDER. The two data sets can then be related to each other and the full three dimensional spatio-temporal profile can be extracted.

Again, the versatility of the Dazzler has been exploited to record both data sets. For a) the Dazzler is amplitude-programmed to transmit only narrow quasi-monochromatic wavelength slices to a Hartmann-Shack wavefront sensor. For b) the Dazzler is used as described in the previous chapter summary.

By implementing this configuration we have built a full three dimensional pulse characterisation device called HAMSTER, with a significantly more simple and robust optical setup compared to the various handful of other devices capable of similar characterisation. The device has then been used to characterise the output of our Ti:Sa amplifier, which as expected displayed no significant spatio-temporal coupling. As a verification of the accuracy of the device, one of the most basic STCs - a pulse front tilt was imparted to the pulses, where after the HAMSTER was able to reconstruct the pulse front tilted pulse in full three dimensions.

7.1.4 Chapter 5 - Water-Window High Harmonic Beamline for Soft X-ray Spectroscopy

The significance of the water window radiation range from 284 eV to 543 eV is described in the context of the importance of spectroscopic interrogation of both biological samples and organic semiconductors. The highest photon energies achievable through high harmonic generation are most significantly influenced by the carrier wavelength of the driving laser field. Owing to this, most experiments that have used HHG as the source of XUV or even X-ray photons have been restricted to photons having less than 100 eV - a consequence of being driven directly by 800 nm Ti:Sa amplifiers. By driving the HHG process with 1850 nm radiation we easily access the water window range with usable photon flux.

The high flux $(1.85\pm0.12)\times10^7$ photons/s/1% bandwidth at 300 eV [80] of the soft-x-ray source is achieved through a carefully designed and well implemented HHG beam line, in combination with a macroscopic phase matching technique that mitigates the low harmonic yield expected when driving the process with longer wavelength radiation.

A spectroscopic technique (NEXAFS) which is very well known to the synchrotron community is then for the first time implemented using an HHG x-ray source. An organic molecule called polyimide consisting predominantly of carbon, but also containing nitrogen, hydrogen and oxygen is selected for investigation. The absorption spectrum of the polyimide reveals the transitions to the various orbitals of these atoms. The absorption data is recorded in only 10 minutes (5 minutes for sample and 5 minutes for background) resulting in an excellent signal to noise ratio. Comparing the intrinsically broadband spectrum of HHG to the monochromatic spectra

obtained in a synchrotron, there is a clear benefit. Despite the drastic flux deficit of HHG the measurement requires no energy scanning and is acquired in a single acquisition.

To improve the experimental setup and make use of the intrinsically tiny spot size of the x-ray focus a new x-ray spectrometer has been designed to negate the energy wasting slit, which is normally required to optimise spectral resolution.

7.1.5 Chapter 6 - Attosecond Streaking in the Water-Window

The attosecond streaking technique is widely accepted as the standard characterisation method for ex-situ pulse characterisation in the attosecond regime. The work done in this part of my PhD has resulted in the first streaking measurement of an isolated attosecond pulse in the water-window radiation range.

The high harmonic beamline is reconfigured to enable the pump/probe scheme needed to perform an attosecond streaking technique. Owing to the high flux of our source, the soft x-rays possess sufficient energy to ionise krypton gas in a second gas target (required in the streaking technique). A streaking spectrogram is recorded and evidences the isolated attosecond pulse structure of the pulse however due to insufficient streaking field intensity coupled with an insufficient signal-to-noise ratio, FROGCRAB algorithm based reconstruction of the full phase and pulse duration of the pulse has not been possible. Given the expected attochirp however we expect a maximum pulse duration of around 400 as with a spectral bandwidth that supports pulses less than 20 as, which is below the atomic unit of time.

A future experiment is planned to address these issues.

7.2 Conclusion

The focus of this thesis can be divided into three main topics. Firstly the redesign and rebuild of a state-of-the art laser system, secondly the characterisation of the laser system and thirdly, the first applications of the laser system and characterisation of those applications.

The Ti:Sa laser system that we had purchased, albeit state-of-the art, did not satisfy the stringent requirements to seed an OPA based wavelength conversion scheme. Extensive modelling and redesign and an eventual rebuild of this laser system resulted in significantly improved laser parameters which proved to be what was needed in order to drive the OPA. With the OPA working efficiently, stably and consistently, additional components were cascaded to produce a world-unique laser source. The output parameters of which are sub-two-cycle (12 fs) laser pulses with a central wavelength of 1850 nm. The laser pulses are CEP stabilised to the sub 100 mrad level and the shot to shot stability is around the 1 percent level over extended periods of time. This new system provided the key to the generation of water-window high harmonics.

Two new pulse characterisation techniques for Ti:Sa laser pulses were developed. The first technique pushed the limits of one of the most simple-to-align optical setups to the regime of few cycle pulses and resulted in the characterisation of the shortest pulse ever measured with this kind of device. The second technique addressed an often overlooked aspect of 3D pulse characterisation, specifically the spatio-temporal profile of ultra-short laser pulses. Through combination of the characterisation of the spectral phase and spatial phase

of a laser pulse, the technique allows for the full four dimensional (three spatial dimensions, one temporal dimension) characterisation of an ultra-short laser pulse.

The long wavelength pulses were then used to generate ponderomotively scaled high harmonics which extend to and span the entire water-window range of radiation (284 eV to 543 eV). This radiation was then used to perform the first ever high-harmonic based NEXAFS measurement in the water-window. The orbital transitions corresponding to absorption of the radiation in polyimide were identified with outstanding resolution and signal to noise ratio.

Finally the de-facto measurement technique for isolated attosecond pulses was for the first time extended beyond the 100 eV regime by successfully performing a streaking measurement of 300 eV+ harmonic continuum. Owing to the current limitations of the experimental setup, an accurate reconstruction of the spectral phase has not yet been possible, but improvements to the setup are underway to enable access to this information.

7.3 Outlook

With the successful redesign and build up of the few-cycle, phase stable, long wavelength laser source we have successfully demonstrated two significant and ground breaking results: high resolution water-window soft x-ray spectroscopy and isolated attosecond pulses in the water window. The natural progression is to combine these two results into an experimental tool capable of investigating the temporal dynamics of interactions occurring in the water window radiation range. The obvious class of experiments are the transient absorption scheme, in which x-rays transmitted through a sample

are resolved by a spectrometer. The sample is then perturbed by a second laser pulse where the delay between the x-rays and the laser pulse are scanned. Typically the changes in the absorption spectra include changes in absolute absorption and the broadening or narrowing of absorption peaks. The changes expected can be quite small - sub percent level, however this is where the high resolution, high stability and good signal-to-noise characteristics of the x-ray source can be used to the fullest.

Appendix A

Appendix

A.1 FEA Thermal Simulations

The FEA simulations are performed using COMSOL Multiphysics, which has built in materials, however they do not take into account the temperature dependence of the three components of the Ti:Sa crystal assembly: copper, sapphire and indium. Tabulated data [81] is imported into COMSOL to more accurately model the thermal properties of our amplifiers.

The full simulation then takes into account the Ti:Sa crystal, the indium buffering and the copper mounts. Boundary conditions are applied at the cold finger side of the mount at 50 K. This temperature corresponds to the loaded temperature that is measured by a thermocouple, permanently connected to the copper mount. A heat load of 70 W is applied to a 500 µm diameter cylinder through the crystal, approximating the heat transfer area from pump laser to the crystal. Simulation convergence depends both on the complexity of the model as well as the element size chosen. Typically satisfactory

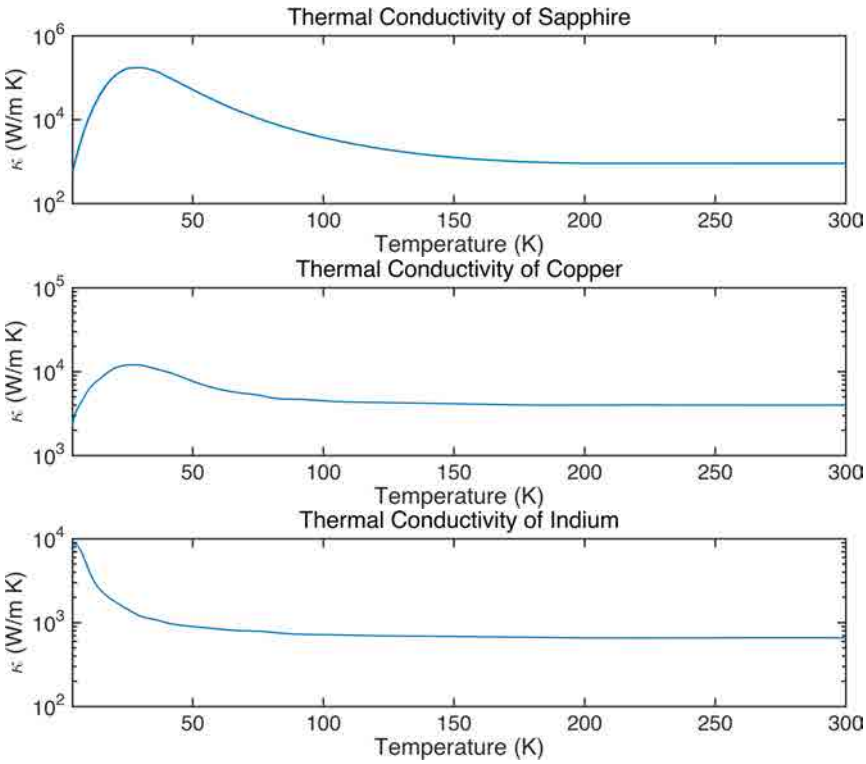

FIGURE A.1: Thermal conductivities of copper, indium and sapphire

results can be achieved in less than an hour, making it very quick and easy to make and test changes.

A.2 B-Integral Calculation

The B-integral for the system is calculated using equation (2.1), based on the measured stretched pulse duration of 170 ps. For the regen, pulse intensity per pass through material is calculated based on calibrated photodiode measurements of the pulse still in the cavity as well as the ejected pulse as seen in Fig. A.2, where the dotted grey lines indicate successive round-trips in the cavity. The dominant in-cavity sources are included: Ti:Sa crystal, Brewster windows, Pockel's cell and the thin film polariser. The B-integral calculated for the regen is 1.51.

The booster amplifier, with only two passes, is easier to calculate as

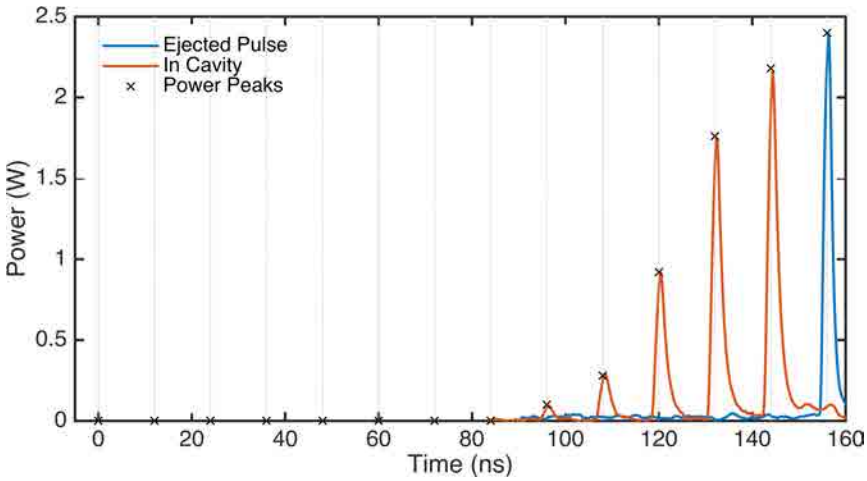

FIGURE A.2: Photodiode based calibration, of the in-cavity and ejected pulse power

the only transmissive optics are the Ti:Sa crystal and the Brewster windows sealing the vacuum chamber. The B-integral calculated for the booster is 0.91

The total B-integral for the system is 2.42

A.3 Pockel's Cell Alignment

Alignment of a Pockel's cell is most conventionally achieved using the "Maltese Cross" technique, which is described in many places however I have not seen a published image of what a Maltese cross in the context of a Pockel's cell actually looks like. This appendix section serves both as an alignment guide to readers as well as to my knowledge, the first published photograph of a Pockel's cell Maltese cross. The Pockel's cell is to be aligned with polarised light. The first step is to locate the Pockel's cell in the beam and roughly align it using the back reflection from the crystal. Next, place a reference such as a mark on a beam block on the laser spot transmitted through the crystal. Next the polarisation before the Pockel's cell needs to be rotated 90 degrees and a piece of semi-opaque Sellotape/Scotchtape must be placed on the entrance aperture of the Pockel's cell. Finally, a polariser, such as a polarising beam splitting cube is placed after the exit aperture of the Pockel's cell. The Maltese cross will now be

FIGURE A.3: The photographs are taken by placing an infra-red viewing camera in front of a smartphone camera.

visible on the earlier placed beam block (see Fig. A.3). Adjustment

of the tip and tilt of the Pockel's cell crystal can be used to ensure that the central spot is where the earlier reference was taken and that the cross is placed symmetrically about it.

A.4 SHG FROG

The SHG FROG is used to measure the Ti:Sa pulses, the TOPAS pulses as well as the HCF output pulses and hence has been built with versatility in mind. An ultra-thin pellicle is used as the beam-splitter and can be exchanged based on which the desired wavelength measurement range is i.e. 800 nm or 1850 nm. owing to its sub-5 µm thickness it can be used for few-cycle pulse measurement as the expected dispersion is negligible. The non-linear crystal can too be exchanged, based on the phase matching requirements, however typically a 50 µm thick BBO crystal is used for >40 fs and a 10 µm thick BBO crystal is used for few-cycle pulse durations. The delay stage and spectrometer interact with a MatLab interface (written by a former post-doc) to record the FROG spectrograms.

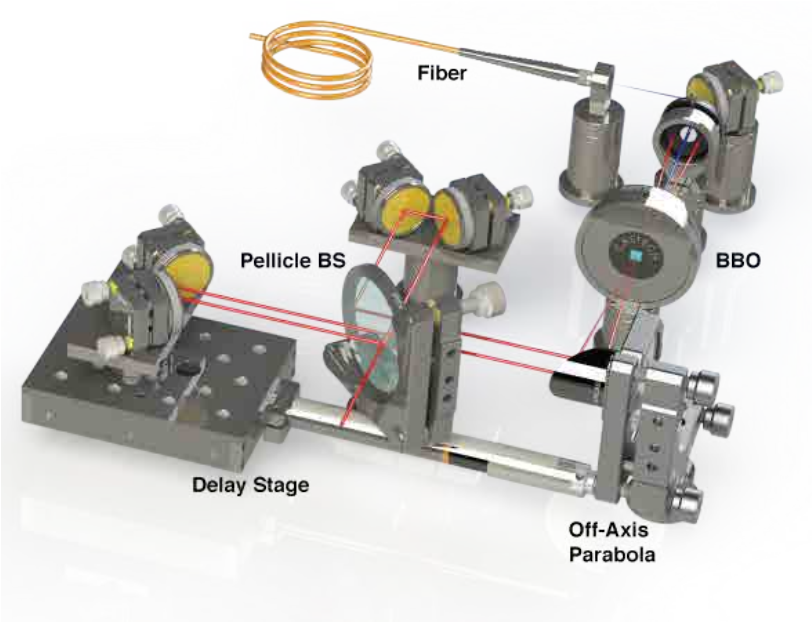

FIGURE A.4: SHG FROG Schematic

A.5 Dispersion calculation in TeO_2

All calculations are performed in MatLab

The refractive indices of TeO_2[82] are given by the Sellmeier equations:

$$n_o^2 - 1 = \frac{2.584\lambda^2}{\lambda^2 - (0.1342)^2} + \frac{1.157\lambda^2}{\lambda^2 - (0.2638)^2}$$
$$n_e^2 - 1 = \frac{2.823\lambda^2}{\lambda^2 - (0.1342)^2} + \frac{1.542\lambda^2}{\lambda^2 - (0.2631)^2}$$

For a 25 mm TeO_2 crystal as used in the AOPDF, the second and third order dispersion terms are calculated at 800 nm to be $GDD_o = 12425\,\text{fs}^2$ and $TOD_o = 8132\,\text{fs}^3$. $GDD_e = 14585\,\text{fs}^2$ and $TOD_o = 9625\,\text{fs}^3$

A.6 Neon Group Velocity Dispersion

A.6.1 Neutral Neon

The temperature and pressure dependant refractive index of neon is calculated using the atomic scattering factors $f1$ and $f2$ taken from tabulated data [63]. The refractive index is then adjusted for the temperature and pressure according to the following equation [78]:

$$n = \left(2\frac{n_0^2 - 1}{n_0^2 + 2}\frac{pT_0}{p_0 T} + 1\right)^{1/2} \left(1 - \frac{n_0^2 - 1}{n_0^2 + 2}\frac{pT_0}{p_0 T} + 1\right)^{-1/2} \tag{A.1}$$

Where T_0 is 273.15 K, p_0 is 1 atm and n_0 is the refractive index at p_0, T_0.

To give an indication of the order of magnitude of GVD, Fig. A.5 shows the temperature independent GVD of neutral neon for a range of photon energies covering the water-window range.

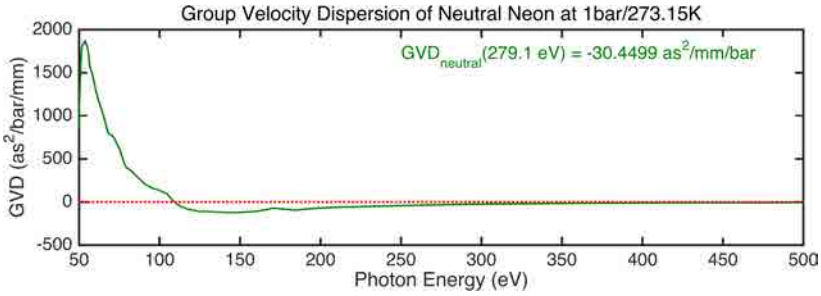

FIGURE A.5: Group velocity dispersion of neon at 1bar

A.6.2 Ionised Neon

The refractive index of a plasma [83] is given by:

$$n = \sqrt{\left(n_o^2 - \frac{\omega_p^2}{\omega^2}\right)} \tag{A.2}$$

Where n_0 is the refractive index of neutral medium, ω is the angular frequency of the harmonic radiation and ω_p is the plasma frequency given by:

$$\omega_p = \sqrt{\left(\frac{N_e e^2}{\epsilon_0 m_e}\right)} \tag{A.3}$$

Where N_e is the electron number density, e is the electron charge , ϵ_0 is the permittivity of free space and m_e is the electron mass.

In the relevant frequency range: $2.3{\times}10^{17} rad\, s^{-1}$ to $6.1{\times}10^{17} rad\, s^{-1}$), $n_o \approx 1$ - derived from tabulated data [63]. At 300 eV, $\omega = 4.6 \times 10^{17} rad\, s^{-1}$, whereas the plasma frequency for 1 bar of neon is $2.8 \times 10^{14} rad\, s^{-1}$. Given the 3 orders of magnitude difference, its clear that at these frequencies, the refractive index of the plasma ≈1 and thus no significant GVD is expected from neon plasma. Figure A.6 shows the plasma GVD for a range of photon energies of 50 eV to 400 eV

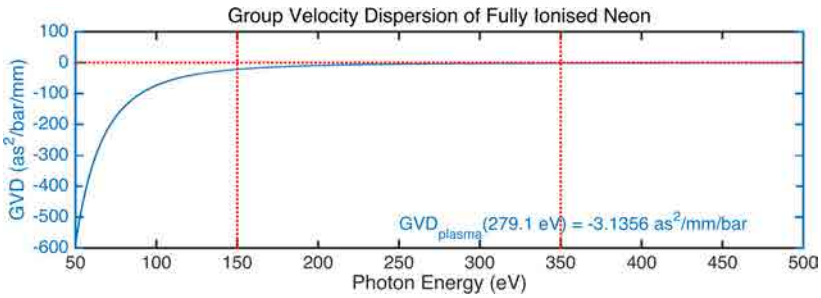

FIGURE A.6: Group velocity dispersion of neon plasma

A.7 Simulated Streaking Traces - Bandwidth Scan

The streaking trace bandwidth scan is performed by generating a streaking trace in Matlab and varying the bandwidth and phase of the attosecond pulse. Two different retrieval algorithms FROGCRAB and LSGPA are then used to try to reconstruct the attosecond pulse. The theoretically generated streak traces along with the reconstructed streak traces for both algorithms are shown in Fig. A.7. Figure A.8 corresponds to a streaking trace generated by a streaking field intensity that is one order of magnitude lower. Both algorithms

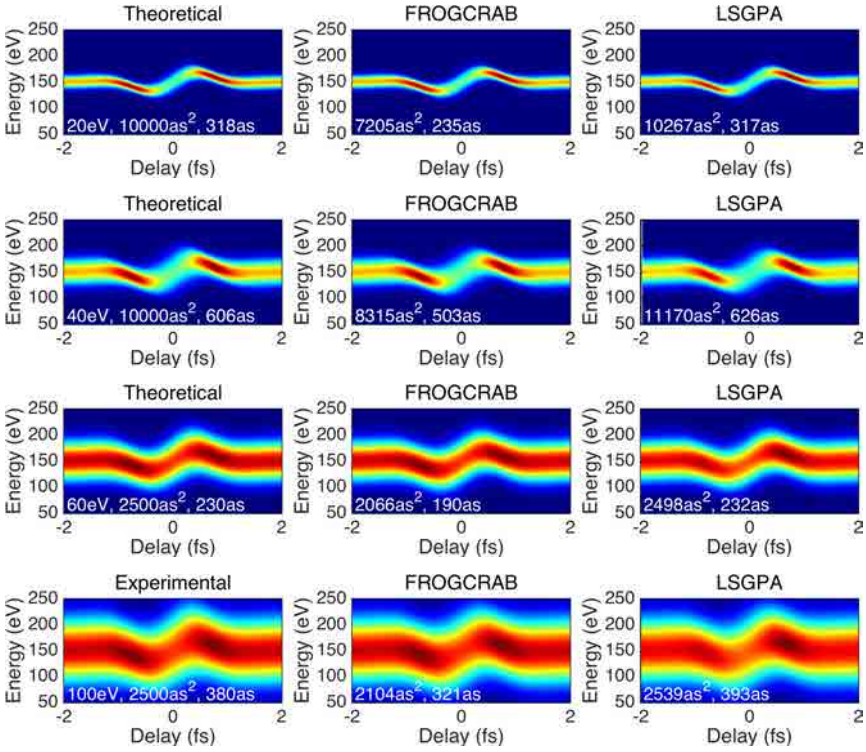

FIGURE A.7: Retrieval of simulated streaking traces, streaked with $1{\times}10^{12}$W/cm^2 intensity

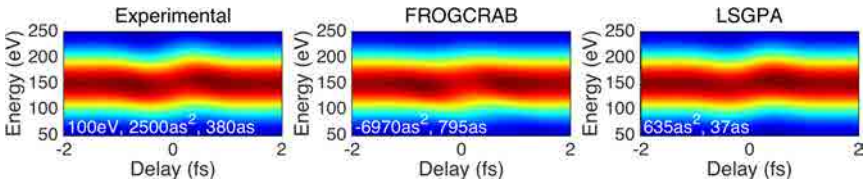

FIGURE A.8: Retrieval of simulated streaking trace, streaked with 1×10^{11}W/cm^2 intensity

successfully reconstruct the theoretical pulse, with varying degrees of accuracy while the streaking field intensity is kept at 1×10^{12}W/cm^2. Once the intensity is dropped an order of magnitude, neither algorithm can reconstruct the pulse, despite the relatively good visible match between the theoretical traces and both the reconstructed traces. Plots are annotated with the bandwidth (left plot), phase and pulse duration (all plots).

Bibliography

1. Al-Khalili, J. *Quantum: A Guide For The Perplexed* (2003).
2. Moulton, P. F. Spectroscopic and laser characteristics of Ti:Al_2O_3. *Journal of the Optical Society of America B* **3,** 125 (1986).
3. Photonix Industries. *Photonix DM series Lasers*
4. Strickland, D. & Mourou, G. Compression of Amplified Chirped Optical Pulses. *Optics Communications* **55,** 447–449 (1985).
5. Koechner, W. *et al. Solid-State Laser Engineering* (2006).
6. Backus, S *et al.* High-efficiency, single-stage 7-kHz high-average-power ultrafast laser system. *Optics Letters* **26,** 465–467 (2001).
7. Rezonator. *Rezonator - Laser Resonator Design Software* 2011. <http://www.rezonator.orion-project.org/>.
8. Backus, S., Durfee, C. G., Murnane, M. M. & Kapteyn, H. C. High power ultrafast lasers. *Review of Scientific Instruments* **69,** 1207 (1998).
9. Armstrong, J. Measurement of picosecond laser pulse widths. *Applied Physics Letters* **10,** 122–124 (1967).
10. Baltuska, A., Fuji, T. & Kobayashi, T. Controlling the carrier-envelope phase of ultrashort light pulses with optical parametric amplifiers. *Physical Review Letters* **88,** 133901 (2002).

11. Schmidt, B. E. *et al.* High harmonic generation with long-wavelength few-cycle laser pulses. *Journal of Physics B: Atomic, Molecular and Optical Physics* **45,** 074008 (2012).

12. Schmidt, B. E. *et al.* CEP stable 1.6 cycle laser pulses at 1.8 μm. *Optics Express* **19,** 6858–6864 (2011).

13. Wittmann, T. *et al.* Single-shot carrier–envelope phase measurement of few-cycle laser pulses. *Nature Physics* **5,** 357–362 (2009).

14. Kane, D. J. & Trebino, R. Characterization of arbitrary femtosecond pulses using frequency-resolved optical gating. *IEEE Journal of Quantum Electronics* **29,** 571–579 (1993).

15. Iaconis, C & Walmsley, I. A. Spectral phase interferometry for direct electric-field reconstruction of ultrashort optical pulses. *Opt. Lett.* **23,** 792–794 (1998).

16. Hauri, C. P., Bruck, M, Kornelis, W, Biegert, J & Keller, U. Generation of 14.8-fs pulses in a spatially dispersed amplifier. *Optics Letters* **29,** 201–203 (2004).

17. Braun, A. *et al.* Self-channeling of high-peak-power femtosecond laser pulses in air. *Optics Letters* **20,** 73 (1995).

18. Guandalini, a *et al.* 5.1 Fs Pulses Generated By Filamentation and Carrier Envelope Phase Stability Analysis. *Journal of Physics B: Atomic, Molecular and Optical Physics* **39,** S257–S264 (2006).

19. Hauri, C *et al.* Generation of intense few-cycle laser pulses through filamentation - parameter dependence. *Optics Express* **13,** 7541–7 (2005).

20. Couairon, A, Franco, M, Mysyrowicz, A, Biegert, J & Keller, U. Pulse self-compression to the single-cycle limit by filamentation in a gas with a pressure gradient. *Optics Letters* **30,** 2657–9 (2005).

21. Hauri, C. *et al.* Generation of intense, carrier-envelope phase-locked few-cycle laser pulses through filamentation. *Applied Physics B* **79,** 673–677 (2004).

22. Nisoli, M., De Silvestri, S. & Svelto, O. Generation of high energy 10 fs pulses by a new pulse compression technique. *Applied Physics Letters* **68,** 2793 (1996).

23. Nisoli, M. *et al.* Toward a terawatt-scale sub-10-fs laser technology. *IEEE Journal of Selected Topics in Quantum Electronics* **4,** 414–420 (1998).

24. Nisoli, M. *et al.* A novel-high energy pulse compression system: generation of multigigawatt sub-5-fs pulses. *Applied Physics B: Lasers and Optics* **65,** 189–196 (1997).

25. Schenkel, B *et al.* Generation of 3.8-fs pulses from adaptive compression of a cascaded hollow fiber supercontinuum. *Optics Letters* **28,** 1987–9 (2003).

26. Bohman, S. *et al.* Generation of 5 fs, 0.5 TW pulses focusable to relativistic intensities at 1 kHz. *Optics Express* **16,** 10684–9 (2008).

27. Harris, S. E. & Wallace, R. W. Acousto-optic tunable filter. *Josa* **59,** 744–747 (1969).

28. Verluise, F, Laude, V, Cheng, Z, Spielmann, C & Tournois, P. Amplitude and phase control of ultrashort pulses by use of an acousto-optic programmable dispersive filter: pulse compression and shaping. *Optics Letters* **25,** 575–7 (2000).

29. Forget, N., Crozatier, V. & Oksenhendler, T. Pulse-measurement techniques using a single amplitude and phase spectral shaper. *J. Opt. Soc. Am. B* **27,** 742–756 (2010).

30. Galler, a. & Feurer, T. Pulse shaper assisted short laser pulse characterization. *Applied Physics B* **90,** 427–430 (2008).

31. Kane, S. & Squier, J. Grism-pair stretcher–compressor system for simultaneous second- and third-order dispersion compensation in chirped-pulse amplification. *Journal of the Optical Society of America B* **14,** 661 (1997).

32. Takeda, M., Ina, H. & Kobayashi, S. Fourier-transform method of fringe-pattern analysis for computer-based topography and interferometry. *Journal of the Optical Society of America* **72,** 156 (1982).

33. Zair, A *et al.* Spatio-temporal characterization of few-cycle pulses obtained by filamentation. *Optics Express* **15,** 5394–5404 (2007).

34. Rubino, E. *et al.* Spatiotemporal amplitude and phase retrieval of space-time coupled ultrashort pulses using the Shackled-FROG technique. *Optics Letters* **34,** 3854–6 (2009).

35. Gabolde, P. & Trebino, R. Single-shot measurement of the full spatio-temporal field of ultrashort pulses with multi-spectral digital holography. *Optics Express* **14,** 4423–4428 (2006).

36. Bowlan, P., Gabolde, P., Coughlan, M. A., Trebino, R. & Levis, R. J. Measuring the spatiotemporal electric field of ultrashort pulses with high spatial and spectral resolution. *J. Opt. Soc. Am. B* **25,** A81–A92 (2008).

37. Hebling, J. Derivation of the pulse front tilt caused by angular dispersion. *Optical and Quantum Electronics* **28,** 1759–1763 (1996).

38. Martinez, O. E., Gordon, J. P. & Fork, R. L. Negative group-velocity dispersion using refraction. *Journal of the Optical Society of America A* **1,** 1003 (1984).

39. Drescher, M *et al.* Time-resolved atomic inner-shell spectroscopy. *Nature* **419,** 803–7 (2002).

40. Cavalieri, A. L. *et al.* Attosecond spectroscopy in condensed matter. *Nature* **449,** 1029–1032 (2007).

41. Goulielmakis, E. *et al.* Real-time observation of valence electron motion. *Nature* **466,** 739–743 (2010).

42. Schultze, M. *et al.* Controlling dielectrics with the electric field of light. *Nature* **493,** 75–78 (2013).

43. Schultze, M. *et al.* Attosecond band-gap dynamics in silicon. *Science* **346,** 1348–1352 (2014).

44. Xu, Q. *et al.* Solution-Processed Highly Conductive PEDOT:PSS/AgNW/GO Transparent Film for Efficient Organic-Si Hybrid Solar Cells. *ACS Applied Materials & Interfaces* **7,** 3272–3279 (2015).

45. Gupta, D., Wienk, M. M. & Janssen, R. A. J. Efficient Polymer Solar Cells on Opaque Substrates with a Laminated PEDOT:PSS Top Electrode. *Advanced Energy Materials* **3,** 782–787 (2013).

46. Lipomi, D. J. *et al.* Electronic Properties of Transparent Conductive Films of PEDOT:PSS on Stretchable Substrates. *Chemistry of Materials* **24,** 373–382 (2012).

47. Tait, J. G. *et al.* Spray coated high-conductivity PEDOT:PSS transparent electrodes for stretchable and mechanically-robust organic solar cells. *Solar Energy Materials and Solar Cells* **110,** 98–106 (2013).

48. Zhang, W. *et al.* High-efficiency ITO-free polymer solar cells using highly conductive PEDOT:PSS/surfactant bilayer transparent anodes. *Energy & Environmental Science* **6,** 1956–1964 (2013).

49. Princeton Instruments. *Water Window Absorption* <http://www.princetoninstruments.com/Xray/microscopy.aspx>.

50. Corkum, P. Plasma Perspective on Strong-Field Multiphoton Ionization. *Physical Review Letters* **71,** 1994–1997 (1993).

51. Krause, J., Schafer, K. & Kulander, K. High-Order Harmonic Generation from Atoms and Ions in the High Intensity Regime. *Physical Review Letters* **68,** 3535–3538 (1992).

52. Spielmann, C. Generation of Coherent X-rays in the Water Window Using 5-Femtosecond Laser Pulses. *Science* **278,** 661–664 (1997).

53. Chen, M.-C. M.-C. *et al.* Bright, Coherent, Ultrafast Soft X-Ray Harmonics Spanning the Water Window from a Tabletop Light Source. *Physical Review Letters* **105,** 173901 (2010).

54. Ishii, N. *et al.* Generation of soft x-ray and water window harmonics using a few-cycle, phase-locked, optical parametric chirped-pulse amplifier. *Optics Letters* **37,** 97 (2012).

55. Popmintchev, T. *et al.* Bright Coherent Ultrahigh Harmonics in the keV X-ray Regime from Mid-Infrared Femtosecond Lasers. *Science* **336,** 1287–1291 (2012).

56. Popmintchev, T. *et al.* Phase matching of high harmonic generation in the soft and hard X-ray regions of the spectrum. *Proceedings of the National Academy of Sciences of the United States of America* **106,** 10516–21 (2009).

57. Takahashi, E. J., Kanai, T., Ishikawa, K. L., Nabekawa, Y. & Midorikawa, K. Coherent Water Window X Ray by Phase-Matched High-Order Harmonic Generation in Neutral Media. *Physical Review Letters* **101,** 253901 (2008).

58. Xiong, H. *et al.* Generation of a coherent x ray in the water window region at 1 kHz repetition rate using a mid-infrared pump source. *Optics Letters* **34,** 1747 (2009).

59. Tate, J. *et al.* Scaling of wave-packet dynamics in an intense midinfrared Field. *Physical Review Letters* **98,** 1–4 (2007).

60. Colosimo, P *et al.* Scaling strong-field interactions towards the classical limit. *Nat Phys* **4,** 386–389 (2008).

61. Frolov, M., Manakov, N. & Starace, A. Wavelength Scaling of High-Harmonic Yield: Threshold Phenomena and Bound State Symmetry Dependence. *Physical Review Letters* **100,** 173001 (2008).

62. Austin, D. & Biegert, J. Strong-field approximation for the wavelength scaling of high-harmonic generation. *Physical Review A* **86** (2012).

63. Henke, B., Gullikson, E. & Davis., J. X-ray interactions: photoabsorption, scattering, transmission, and reflection at E=50-30000 eV, Z=1-92. *Atomic Data and Nuclear Data Tables* **54,** 181–342 (1993).

64. Jeff Scott. *Shock Diamonds and Mach Disks* 2005. <http://www.aerospaceweb.org/question/propulsion/q0224.shtml>.

65. Park, J.-J. *et al.* Supersonic Nozzle Flow Simulations for Particle Coating Applications: Effects of Shockwaves, Nozzle Geometry, Ambient Pressure, and Substrate Location upon Flow

Characteristics. English. *Journal of Thermal Spray Technology* **20,** 514–522 (2011).

66. Crist, S, Glass, D. R. & Sherman, P. M. Study of the highly underexpanded sonic jet. *AIAA Journal* **4,** 68–71 (1966).

67. Ravel, B. & Newville, M. *ATHENA, ARTEMIS, HEPHAESTUS: Data analysis for X-ray absorption spectroscopy using IFEFFIT* in *Journal of Synchrotron Radiation* **12** (2005), 537–541.

68. Sedlmair, J. *et al.* Characterization of refractory organic substances by NEXAFS using a compact X-ray source. *Journal of Soils and Sediments* **12,** 24–34 (2011).

69. Itatani, J *et al.* Attosecond streak camera. *Physical Review Letters* **88,** 173903 (2002).

70. Mairesse, Y. & Quéré, F. Frequency-resolved optical gating for complete reconstruction of attosecond bursts. *Physical Review A - Atomic, Molecular, and Optical Physics* **71,** 1–4 (2005).

71. Sansone, G. *et al.* Isolated Single-Cycle Attosecond Pulses. *Science* **314,** 443–446 (2006).

72. Schultze, M *et al.* Delay in photoemission. *Science* **328,** 1658–1662 (2010).

73. Cavalieri, a. L. *et al.* Attosecond spectroscopy in condensed matter. *Nature* **449,** 1029–1032 (2007).

74. Doumy, G. *et al.* Attosecond synchronization of high-order harmonics from midinfrared drivers. *Physical Review Letters* **102,** 2–5 (2009).

75. Mairesse, Y *et al.* Attosecond Synchronization of High-Harmonic Soft X-rays. *Science* **302,** 1540–1543 (2003).

76. Kim, K. T., Kim, C. M., Baik, M. G., Umesh, G. & Nam, C. H. Single sub-50-attosecond pulse generation from chirp-compensated harmonic radiation using material dispersion. *Physical Review A - Atomic, Molecular, and Optical Physics* **69,** 051805–1 (2004).

77. Ko, D. H., Kim, K. T. & Nam, C. H. Attosecond-chirp compensation with material dispersion to produce near transform-limited attosecond pulses. *Journal of Physics B: Atomic, Molecular and Optical Physics* **45,** 074015 (2012).

78. Lehmeier, H., Leupacher, W. & Penzkofer, A. Nonresonant third order hyperpolarizability of rare gases and N2 determined by third harmonic generation. *Optics Communications* **56,** 67–72 (1985).

79. Gagnon, J., Goulielmakis, E. & Yakovlev, V. S. The accurate FROG characterization of attosecond pulses from streaking measurements. *Applied Physics B: Lasers and Optics* **92,** 25–32 (2008).

80. Cousin, S. L. *et al.* High-flux table-top soft x-ray source driven by sub-2-cycle, CEP stable, 185-μm 1-kHz pulses for carbon K-edge spectroscopy. *Optics Letters* **39,** 5383 (2014).

81. J.E. Jensen, W.A. Tuttle, R.B. Stewart, H. B. & Prodell, A. *Selected Cryogenic Data Notebook* 1980.

82. RefractiveIndex.info. *RefractiveIndex TeO2* 2015. <http://refractiveindex.info>.

83. Corkum, P. Amplification of Picosecond 10 pm Pulses in Multi-atmosphere CO2 Lasers. *IEEE Journal of Quantum Electronics* **21,** 216–232 (1985).